SILICA SUPPORTED PALLADIUM NANOPARTICLES FOR THE

DECARBOXYLATION OF HIGH-ACID FEEDSTOCKS:

DESIGN, DEACTIVATION AND REGENERATION

A Dissertation
Presented to
The Academic Faculty

By

Eric Wayne Ping

In Partial Fulfillment
Of the Requirements for the Degree
Doctor of Philosophy in
Chemical & Biomolecular Engineering

Georgia Institute of Technology

May, 2011

SILICA SUPPORTED PALLADIUM NANOPARTICLES FOR THE

DECARBOXYLATION OF HIGH-ACID FEEDSTOCKS:

DESIGN, DEACTIVATION AND REGENERATION

Approved by:

Dr. Christopher W. Jones
School of Chemical & Biomolecular
Engineering
Georgia Institute of Technology

Dr. Pradeep K. Agrawal
School of Chemical & Biomolecular
Engineering
Georgia Institute of Technology

John Pierson
Georgia Tech Research Institute
Georgia Institute of Technology

Dr. Thomas F. Fuller
School of Chemical & Biomolecular
Engineering
Georgia Institute of Technology

Dr. Andrei G. Fedorov
School of Mechanical Engineering
Georgia Institute of Technology

Robert Wallace
Georgia Tech Research Institute
Georgia Institute of Technology

Date Approved:

ACKNOWLEDGEMENTS

I could not have completed this thesis without the support, encouragement and assistance of many people. I would like to thank Professor Chris Jones for continually pushing me in all aspects of my Georgia Tech life, putting up with my antics, and every once in a while indulging my ego with undeserved praise. Through his guidance I have evolved both scientifically and philosophically, and his experiences and opinions have been an invaluable resource to me. I also owe a big thank you to Professor Tom Fuller, whose co-guidance has allowed me to experience the electrochemical side of life—which I surely would have otherwise acknowledged merely in passing.

I would also like to thank my committee members, Professor Pradeep Agrawal, Professor Andrei Fedorov, John Pierson & Robert Wallace, for their willingness to provide insight from all angles and provide breadth of perspective to this project. I owe a special debt of gratitude to Dr. Agrawal, who mentored me as a teaching assistant, providing me with insight into the inner workings of one our school's eminent lecturers. The past four and a half years of engaging intellectual discourse and general camaraderie has finally convinced me to forgive him for his ChBE 6300 final. Barely.

To the members of the Jones Group past and present, I owe my sanity. Through the late nights and early mornings, it's your antics that keep me on my toes. Thank you especially to Jason Hicks for indoctrinating me into a decent research work ethic with your early guidance, and Chris Gill for teaching me it's okay to sometimes just ignore everyone and focus on the task at hand. A great big thanks to Krishnan Venkatasubbaiah, from whom I've learned more organic chemistry than in 10 years of classes. Your

constant distractions have both rescued me from the edge of sanity and threatened push me off the edge, but that's what goofy mustachioed friends are for. And of course I must provide infinite thanks to Jeff Drese, living proof of how two people can be entirely different yet so alike, and manage to become great friends because of it. Whether it was office rock sessions at four in the morning, friendly decompression at a local watering hole, or arguing incessantly about scientific concepts, your presence was always appreciated and your impact was immeasurable.

Most importantly, I'd like to thank my parents, Steve and Wendy Ping, without whom I wouldn't be anywhere, and I don't just mean that in the obvious sense. My love of science and insatiable hunger for knowledge is entirely attributed to the loving nurture of my two favorite engineers. I can't remember a time when they didn't do everything in their power to support and encourage me in my various endeavors, however outlandish they may have been. I know it hasn't always been easy, and their dedication has not been taken for granted. Thanks from the bottom of my heart—I know you guys are excited and proud, and nothing in the world means more to me.

TABLE OF CONTENTS

LIST OF TABLES

LIST OF FIGURES

Page

LIST OF SYMBOLS AND ABBREVIATIONS

δ	chemical shift
ΔG	Gibbs free energy of reaction
ΔH	enthalpy of reaction
APTMS	3-aminopropyltrimethoxysilane
BdB	Broekhof-de Boer
BdB-FHH	Frenkel-Halsey-Hill modified Broekhof-de Boer
BET	Brunauer-Emmet-Teller
BJH	Barrett-Joyner-Halenda
BSA	N,O-bis(trimethylsilyl)acetamide
CP-MAS	cross polarization magic angle spinning
CTAB	cetyltrimethylammonium bromide
DCM	dichloromethane
DI	deionized
DLS	dynamic light scattering
DMSO	dimethylsulfoxide
DSC	differential scanning calorimetry
EJ	exajoules
EXAFS	extended X-ray absorption fine structure
FAME	fatty acid methyl ester
FEG	field emission gun
FFA	free fatty acid

FT	Fourier transform
GC	gas chromatography
GC-MS	gas chromatography mass spectrometry
GC-FID	gas chromatography flame ionization detector
HDO	hydrodeoxygenation
ICP-OES	inductively coupled plasma optical emission spectrometry
IPCC	Intergovernmental Panel on Climate Change
IR	infrared
MBDOE	million barrels per day oil equivalent
MCF	mesocellular foam
MCM-41	type of ordered amorphous mesoporous silica
MCM-48	type of ordered amorphous mesoporous silica
MPTMS	3-mercaptopropyltrimethoxysilane
MS	mass spectrometry
NExBTL	Neste biomass to liquid fuel
NMR	nuclear magnetic resonance
OECD	Organisation for Economic Co-operation and Development
P123	Pluronic 123 $EO_{20}PO_{70}EO_{20}$ triblock copolymer
PBG	polished brown grease
ppm	parts per million
PSD	pore size distribution
SAXS	small angle X-ray scattering

SBA-15	type of ordered amorphous mesoporous silica
SEM	scanning electron microscopy
TCD	thermal conductivity detector
TEM	transmission electron microscopy
TEOS	tetraethylorthosilicate
TGA	thermogravimetric analysis
THF	tetrahydrofuran
TMB	1,2,5-trimethylbenzene
TPD	temperature programmed desorption
UPTMS	3-ureidopropyltrimethoxysilane
VBA	Visual Basic for Applications
XAFS	X-ray absorption spectroscopy
XPS	X-ray photoelectron spectroscopy
XRD	X-ray diffraction

SUMMARY

The major goals of this thesis were to (1) design and synthesize a supported catalyst with well-defined monodisperse palladium nanoparticles evenly distributed throughout an inorganic oxide substrate with tunable porosity characteristics, (2) demonstrate the catalytic activity of this material in the decarboxylation of long chain fatty acids and their derivatives to make diesel-length hydrocarbons, (3) elucidate the deactivation mechanism of supported palladium catalysts under decarboxylation conditions via post mortem catalyst characterization and develop a regeneration methodology thereupon, and (4) apply this catalytic system to a real low-value biofeedstock.

Initial catalyst designs were based on the SBA-15 silica support, but in an effort to maximize loading and minimize mass transfer limitations, silica MCF was synthesized as catalyst support. Functionalization with various silane ligands yielded a surface that facilitated even distribution of palladium precursor salts throughout the catalyst particle, and, after reduction, monodisperse palladium nanoparticles approximately 2 nm in diameter. Complete characterization was performed on this Pd-MCF catalyst.

The Pd-MCF catalyst showed high one-time activity in the decarboxylation of fatty acids to hydrocarbons in dodecane at 300 °C. Hydrogen was found to be an unnecessary reactant in the absence of unsaturations, but was required in their presence—full hydrogenation of the double bonds occurs before any decarboxylation can take place. The Pd-MCF also exhibited good activity for alkyl esters and glycerol, providing a nice

hypothetical description of a stepwise reaction pathway for catalytic decarboxylation of acids and their derivatives.

As expected, the Pd-MCF catalyst experienced severe deactivation after only one use. Substantial effort was put into elucidating the nature of this deactivation via post mortem catalyst characterization. H_2 chemisorption confirmed a loss of active surface area, but TEM and EXAFS ruled out morphological alterations in the supported nanoparticles. Significant decreases in pore volume and surface area via N_2 physisorption put deposition under suspicion and TGA confirmed the presence of organic species in the material. Initial attempts to remove the deposits via calcination were successful, but at the expense of severe nanoparticle growth. GC-MS, NMR and FT-IR helped speciate the deposition, mainly confirming the presence of residual reactant acid. A regeneration scheme was developed to remove these compounds, and subsequent catalyst reuses exhibited high decarboxylation activity.

Finally, the Pd-MCF catalyst was applied to a real feedstock: a wastewater-derived brown grease from a poultry rendering facility. Attempts at decarboxylating the raw material failed, so efforts to polish the material via dewaxing and degumming were undertaken. The treatments were able to optimize a three-phase separation, and the resultant polished brown grease was successfully decarboxylated to diesel-length hydrocarbons with high conversions and selectivities.

CHAPTER 1

INTRODUCTION

1.1 Trends, Projections, and Impact of Energy Consumption

For over 50 years, the scientific community has been issuing warnings regarding the world's depleting petroleum reserves [1]. Coupled with the forecast that global total energy consumption will nearly triple from 350 EJ (3.5×10^{20} J) in 1995 to 900 EJ by 2040 [2], it becomes increasingly vital to find alternative and renewable sources of energy. Wind, solar, nuclear, and hydro are all promising candidates to account for portions of that energy requirement, but these options currently have minimal application to the realm of transportation fuel. Global transportation liquid fuel demand is expected to increase from the current level of approximately 85 million barrels per day of oil equivalent (MBDOE) [3-5] to over 100 MBDOE by as soon as 2035 (Figure 1.1) [6, 7]. With much debate over total global petroleum reserves, including 2009 estimates of approximately 1.3 trillion barrels [6], this transportation fuel consumption growth rate cannot be met by petroleum alone, discounting all other consumption industries (Figure 1.2).

Global Transportation Demand
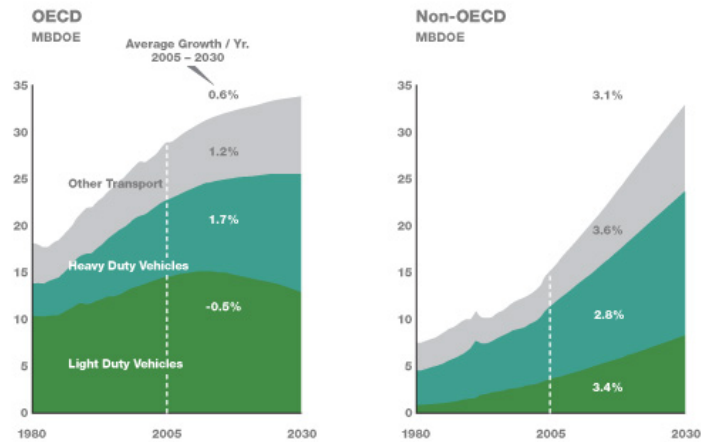
Figure 1.1 – Transportation fuel demand projections for OECD and non-OECD nations Image source: Energy Information Administration, Department of Energy, Annual Energy Review (2009) [7].

OIL AND GAS LIQUIDS
2004 Scenario
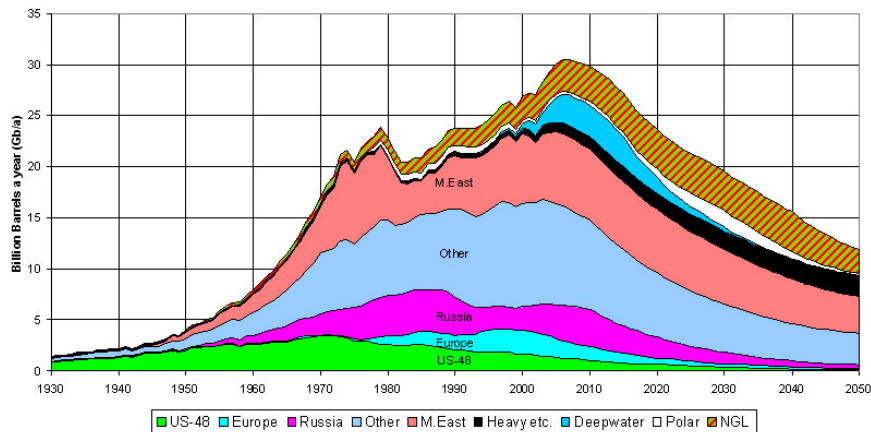
Figure 1.2 – Petroleum availability trends and projections. Image source: Uppsala Hydrocarbon Depletion Study Group (2004).

Additionally, a direct by-product of the heavy dependence on fossil fuels is the rise in global atmospheric CO_2 concentration from ever-increasing global CO_2 emissions. In the absence of mitigation, CO_2 emissions will rise correspondingly with the increased dependence on fossil fuels, a trend seen for decades (Figure 1.3). Accordingly, the

2

increasing anthropogenic CO_2 emissions directly increase the average atmospheric CO_2 concentration (Figure 1.4). The Intergovernmental Panel on Climate Change (IPCC) has confirmed the rising levels of atmospheric carbon dioxide associated with fossil fuel burning contribute measurably to global climate change [8]. Furthermore, in 2006, carbon dioxide emissions from liquid fuels in the transportation sector in the United States alone eclipsed two billion metric tons per year [9]. Though there is much debate as to what the effects of this increased atmospheric CO_2 concentration will have on the Earth's climate [10], it is clear that the burning of fossil fuels essentially serves as a short-circuit to the Earth's natural carbon cycle (Figure 1.5). Recent reports have indicated that certain biofuel lifecycles can be carbon neutral [3] or even carbon negative [11]. Thus it has become a problem of finding a feedstock that is plentiful, ethical, inexpensive, and easily converted into a practical biofuel.
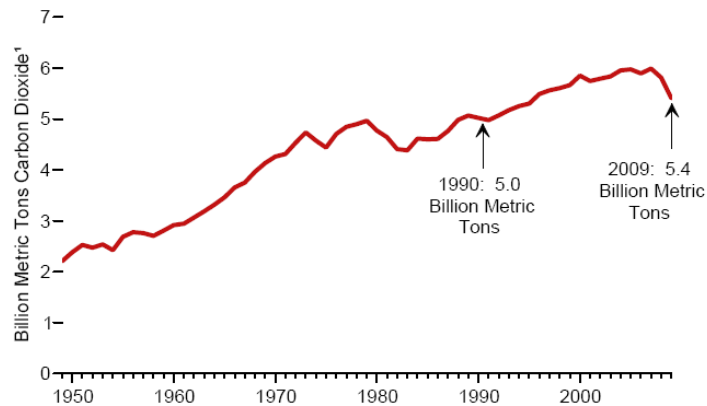
Figure 1.3 – CO_2 emissions for all U.S. sectors from 1950 to present day in billion metric tons of CO_2. Source: Energy Information Administration, Department of Energy, Annual Energy Review (2009) [7].
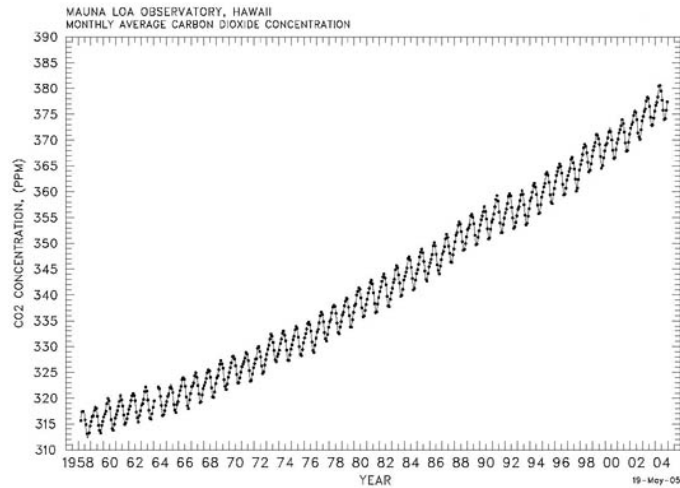
Figure 1.4 – Atmospheric concentrations of CO_2 from 1958 to 2005, showing a continuous rise from 315 ppm to 380 ppm. Source: National Ocean & Atmospheric Administration, Earth System Research Laboratory
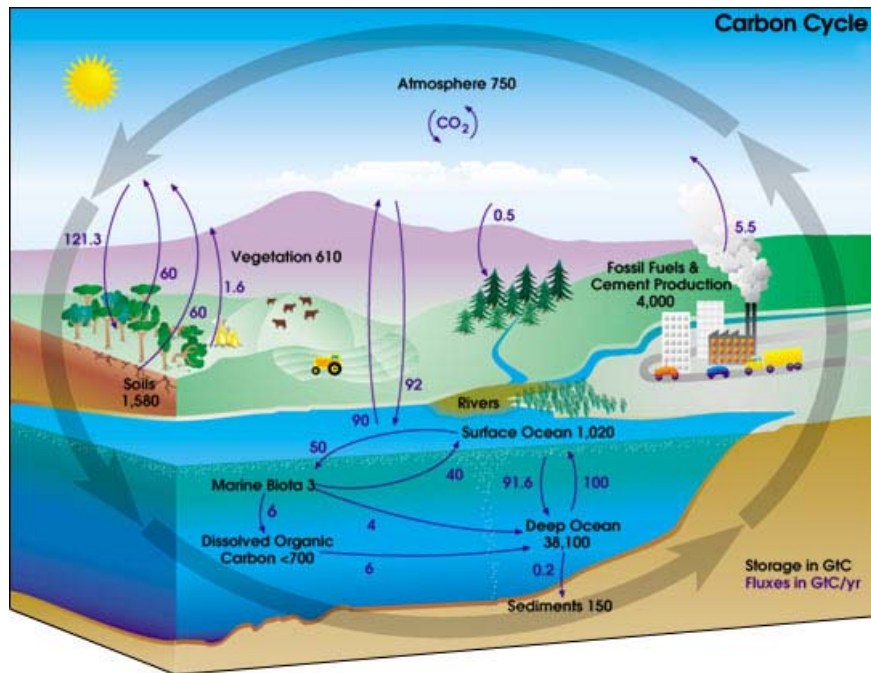
Figure 1.5 – Carbon cycle cartoon showing storage capacities and annual fluxes. Source: NASA Earth Science Enterprise, EOS Project Science Office

1.2 Biomass as a Renewable Energy Resource

Biomass has been recognized as a major world renewable energy source to supplement declining fossil fuel resources, appearing to be an attractive feedstock for three reasons: (i) it is a renewable resource that could be sustainably developed in the future, (ii) it appears to have formidably positive environmental properties resulting in little-to-no net release of carbon dioxide (CO_2) and very low sulfur content, and (iii) it appears to have significant economic potential provided that fossil fuel prices continue to increase [12-14]. Biomass is a widely prevalent renewable resource; Eggersdorfer, et al. reports 170 billion tons of biomass are produced globally per year, of which only 6 billion tons are cultivated (food & non-food) [15]. While the majority of this biomass goes towards feeding the world's ever-increasing population or providing them with requisite organic-based goods, there has been substantial increase in biomass conversion to fuel in the recent years [16]. The sources of biomass most commonly processed to transportation fuels are oils and fats, of which an estimated 165 million tons were produced globally in 2007 [17]. The main sources of oil and fats are vegetable and plant oils, such as rapeseed oil, sunflower oil, soybean oil, etc., and animal byproducts, such as poultry fat, tallow, yellow grease and brown grease. The main components of all these feedstocks are tri-, di-, and mono- glycerides, free fatty acids (FFA), and water.

1.3 Esterified and Transesterified Biodiesels

The standard method to convert lipid feedstocks into transportation fuel is to transesterify the glycerides with an alcohol to form alkyl esters (Figure 1.6) [18]. This is done industrially via homogeneous base catalysis, using either NaOH or $NaOCH_3$, to

produce an estimated 6.5 million tons of methyl ester biodiesel annually [19]. In these processes, feedstock oils must be highly refined to comply with rigorous specifications of water content (less than 0.3 wt %) and FFA content (less than 0.5 wt %), due to the formation of soap (Figure 1.7) [20]. These demanding requirements increase the feedstock cost dramatically, accounting for nearly 75% of the final biodiesel cost (Figure 1.8) [21]. This brings to light the possibility of decreasing renewable fuel costs substantially by using cheaper feedstocks, and here I focus on the usage of low cost high-acid feedstocks. Whereas crude soybean oil and rapeseed oil prices cost approximately $0.90 / kg, high acid materials such as soapstock are available for as low as $0.11 / kg dry weight [20].
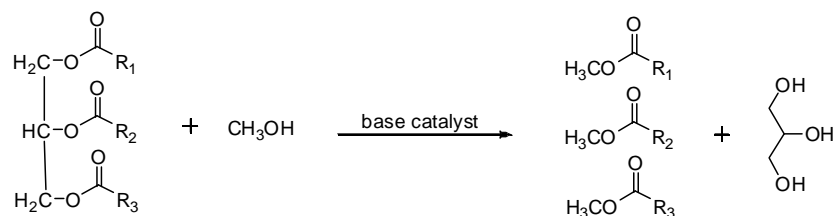
Figure 1.6 – Transesterification of triglycerides with methanol to form FAME biodiesel.
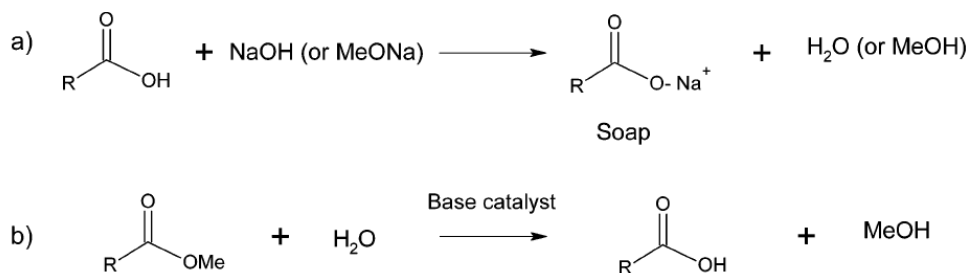
Figure 1.7 – Saponification mechanism in the presence of (a) free fatty acids or (b) water
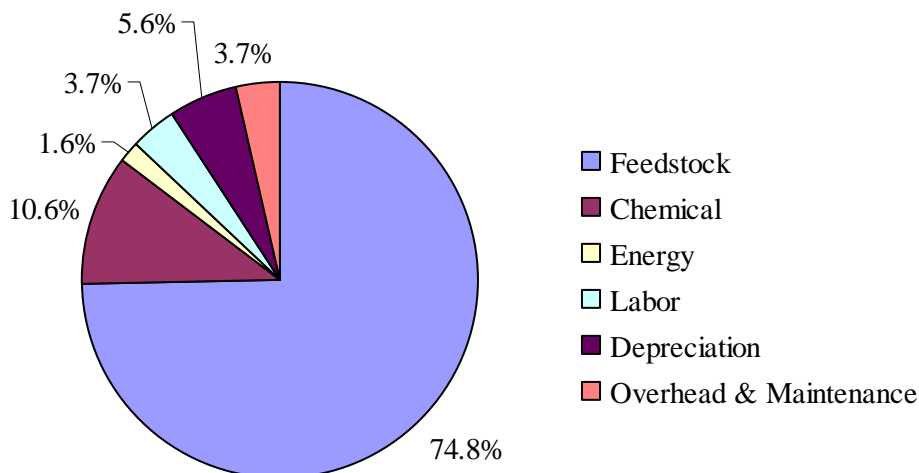
Figure 1.8 – Typical distribution for renewable fuel production costs (data from [21])

There are a number of reports [18, 20-23] on converting these acids to fatty acid methyl ester (FAME) biodiesel; however, biodiesel has some distinctive properties to consider before regarding this as the best final product. Biodiesel (ASTM D6751) is of course renewable, biodegradable and non-toxic, and has a higher flash point than petroleum diesel [24]. Furthermore, it has lower sulfur and aromatic content, higher combustion efficiency, and higher lubricity than petroleum diesel [25, 26]. However, biodiesel also has higher viscosity, higher cloud point and pour point, higher nitrogen oxides (NO_x) emissions, lower energy density, and higher injector/engine wear [27-30]. With the inherent disadvantages of FAME, it would be advantageous to make a renewable fuel with the benefits of a biofuel (i.e., renewable, low sulfur, low aromaticity) but exhibiting petroleum Diesel-like properties (lower cloud and pour points, lower NO_x emissions, higher energy density, lower engine wear).

1.4 Established Feedstock Deoxygenation

To avoid the disadvantageous physical properties of oxygenated fuels, feedstock deoxygenation has been investigated as an alternative pathway of biofuel production. Established hydroprocessing catalysts like supported cobalt/molybdenum or nickel/molybdenum have been applied to the hydrodeoxygenation (HDO) of biomass feedstocks [31-35], and existing HDO infrastructure in long-operating refineries could cut down capital expenditures. However, expensive operating conditions such as temperatures exceeding 400 °C and hydrogen pressures >90 bar are often required for complete conversion. Atmospheric pressure deoxygenation reactions at 320 °C - 450 °C were studied combined with catalytic cracking over zeolites [36-41], mesoporous aluminosilicates [42, 43], and oxide-supported platinum [43], and various pillared clays were applied to the cracking of vegetable oils at 400 °C – 500°C [44]. Additionally, stearic acid has been treated with alkali hydroxides and metal oxides in supercritical water to form C_{16} and C_{17} hydrocarbon products in low yields [45].

Generally speaking, the plausible reaction modes of linear hydrocarbon formation via deoxygenation of fatty acids are represented in Table 1.1 (thermodynamic data listed is from production of linear C_{17} hydrocarbons from stearic acid [46]). Fatty acids can be directly decarboxylated or decarbonylated. Direct decarboxylation cleaves the carboxyl group by evolving carbon dioxide and producing a paraffinic hydrocarbon, while direct decarbonylation gives an olefinic hydrocarbon via removal of the carboxyl group as carbon monoxide and water (reactions I and II). Additionally, the fatty acid can be deoxygenated by adding hydrogen-- the production of linear hydrocarbon can take place via direct hydrogenation or indirect decarbonylation (reactions III and IV). This direct

8

catalytic hydrogenation technology is currently adapted industrially in the NExBTL

Diesel project by Neste Oil [47]. Furthermore, a handful of side reactions can take place

concurrently in the gas phase of the deoxygenation reactors, utilizing the CO, CO_2,

hydrogen and water formed during decarboxylation and decarbonylation. The water gas

shift and methanation reactions are shown in Table 1.1, with thermodynamic data

provided for the gas phase reactions at 300 °C.

Table 1.1 – Reaction modes for deoxygenation of fatty acid feedstocks, including gas
phase side reactions [46]. R = saturated alkyl group, R′ = unsaturated alkyl group

Liquid phase reactions	$\Delta G°_{573}$ (kJ/mol)	$\Delta H°_{573}$ (kJ/mol)
I. Decarboxylation		
R—COOH $\rightarrow$ R—H + CO_2	83.5	9.2
II. Decarbonylation		
R—COOH $\rightarrow$ R′—H + CO + H_2O	47.0	179.1
III. Hydrodecarbonylation		
R—COOH + H_2 $\rightarrow$ R—H + CO + H_2O	-67.6	48.1
IV. Hydrogenation		
R—COOH + $3H_2$ $\rightarrow$ R—CH_3 + $2H_2O$	-86.1	-115.0
Gas Phase Reactions		
V. Methanation		
CO_2 + $4H_2$ $\rightleftharpoons$ CH_4 + $2H_2O$	-61.2	-177.2
VI. Methanation		
CO_2 + $3H_2$ $\rightleftharpoons$ CH_4 + H_2O	-78.8	-216.4
VII. Water gas shift		
CO + H_2O $\rightleftharpoons$ CO_2 + H_2	-17.6	-39.2

1.5 Catalytic Decarboxylation

Initial reports of catalytic decarboxylation of fatty acids were published by the Murzin group [46, 48-57]. A variety of metals supported on different substrates were screened in the decarboxylation of stearic acid at 300 °C (Figure 1.9), the results of which are shown in Table 1.2. While most platinum group metals showed some decarboxylation activity, commercially available palladium supported on activated carbon exhibited the highest activity and selectivity to the saturated hydrocarbon product.

Table 1.2 – Metal-support combination screening results for catalytic decarboxylation of stearic acid at 300 °C [56].

Metal	Support	Loading (wt %)	SA_{BET} (m^2/g)	Conversion (%)
Ni	(Raney)	81	94	4.2
	Al_2O_3	16	105	5.2
	SiO_2	60	-	3.4
	Cr_2O_3	50	88	5.9
Ni / Mo	Al_2O_3	3 / 9	195	1.3
Ru	SiO_2	5	411	0.4
	MgO	5	-	0
	C	5	841	3.2
Pd	Al_2O_3	5	299	4.7
	C	1	1126	17.4
	C	5	936	95
	C	10	782	28.9
Pd/Pt	C	8 / 2	-	45
Pt	Al_2O_3	5	95	3.6
	C	5	797	74.8
Ir	Al_2O_3	2	299	0.2
	SiO2	1	379	0.6
Os	C	5	610	2
Rh	SiO_2	3	490	1.1
	C	1	-	3.2
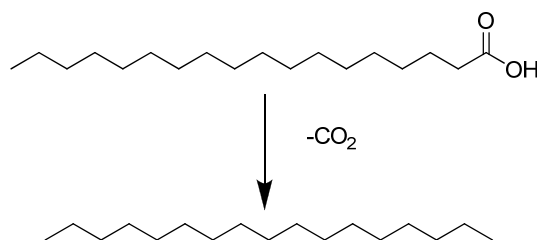
Figure 1.9 – Decarboxylation of stearic acid to form *n*-heptadecane.

The decarboxylation reaction was found to occur as the dominant reaction mode in the absence of hydrogen (i.e. in inert He/Ar/N_2 reaction atmosphere), as there is no net hydrogen requirement in the decarboxylation of fully saturated fatty acids[56]. Hydrogen however was required for high decarboxylation conversion of esters, as decarbonylation dominated in hydrogen-lean environments [56]. Additionally, initial published results indicated unsaturated fatty acids first hydrogenated before deoxygenating to the final hydrocarbon product. Herein were the first unexplained results of concentration-dependent deactivation, with a substantially decreased reaction rate seen for higher initial reactant acid loadings. Subsequently, a comparison of the decarboxylation activity of commercially available palladium on activated carbon and palladium supported on an oxidized synthetic carbon support (Sibunit) was published [53]. The oxidized carbon Sibunit support exhibited heretofore unseen cracking activity at elevated decarboxylation temperatures, yielding smaller chain length hydrocarbon products from the decarboxylation of stearic acid. Also an increase in catalyst "coking" was reported, attributed to the various byproducts of long alkyl chain cracking.

Palladium and ruthenium catalysts were applied to the complete hydrogenation of linoleic acid to stearic acid as a pretreatment reaction for decarboxylation [58]. While initial stearic acid yield was high, detrimental catalyst deactivation was reported for both

11

metals, though the ruthenium deactivated much more rapidly than the palladium. Additionally, lauric acid decarboxylation to form undecane was tested over Pd/C catalysts with substantial deactivation occurring, increasing with increasing lauric acid concentration [52]. Decarboxylation of unsaturated C_{18} acids was investigated in semi-batch with varied initial acid concentration, reaction temperature and solvent [51]. Cursory post-mortem characterization was carried out on the Pd/C catalyst, noting organic deposition via thermogravimetric analysis and loss of surface area and micropore volume via N_2 physisorption. This is attributed hypothetically to coke formation, but no further evidence is shown to support this theory. A recurring trend throughout the current decarboxylation literature is that of very high first-time activity for palladium-based catalysts, with an unexplained detrimental deactivation occurring after one use.

1.6 Research Objectives and Organization

The overarching goal of this work is to develop a viable catalytic system for the decarboxylation of high acid biofeedstocks to form diesel-like hydrocarbons. This includes development of a successful catalyst, the ability to elucidate any catalytic deactivation, and the successful application to multi-use decarboxylation of both model compounds and real-world feedstocks. The objectives of the research presented in this dissertation are:

1. *Develop a well-defined, fully characterized supported palladium catalyst capable of high decarboxylation activity.*

This mainly focuses on catalyst design and development to achieve the overarching goals set forth above. From existing literature, I can be confident of supported palladium being active in the decarboxylation of stearic acid; the difficulty is in developing a methodology to create a material that is both efficient in catalyst loading and well-defined throughout. In other words, the catalyst must be well understood from a chemistry standpoint. Support particle size, morphology, composition, pore size, stability and surface chemistry must be measureable and tunable. Likewise, the supported palladium nanoparticles must be well-distributed, with a narrow particle size distribution while maintaining a high bulk dispersion for palladium atom efficiency. The ability to repeatedly synthesize the catalyst to similar fully-characterized specifications is vital to understanding potential deactivation mechanisms later.

2. *Determine the mechanisms of catalyst deactivation and develop a viable regeneration methodology to recover activity for multi-turnover applications.*

With a well-defined catalyst in hand, the riddle of the mechanism of deactivation can be elucidated utilizing the vast quantity of characterization methodologies available at Georgia Tech and elsewhere. Comparative characterization from fresh and spent catalysts, both in situ and ex situ can provide insight into potential deactivation modes. The ultimate goal of this aim is to regenerate the original activity for catalyst reuse.

3. *Application of the recyclable catalyst system to real world feedstocks to produce diesel-like hydrocarbons in high yield from a low quality biofeedstock.*

With the development of a catalyst active in a system of model compounds, the ultimate goal is successful repeated production of fuel-length alkanes from real biofeedstocks. A brown grease feedstock separated from an aqueous waste stream of a poultry rendering facility will be used as reactant. Various techniques for polishing this feedstock are discussed, and decarboxylation of this feedstock will be monitored and quantified using the aforementioned techniques.

The general organization of this thesis is as follows. Chapter 2 discusses in depth the development of the well defined palladium catalyst. Detailed synthesis and characterization methodologies are explained and applied. Catalytic activity is discussed in Chapter 3, as applied to model systems. Decarboxylation of model compounds ranging from saturated acids, unsaturated acids, alkyl esters, glycerol etc. are discussed, as well as reaction atmosphere and initial concentration effect observations. Catalyst deactivation, post-mortem catalyst characterization, and regeneration methodologies are detailed in Chapter 4. Chapter 5 covers the upgrading of real world biofeedstocks, and Chapter 6 presents a summary of the accomplishments as well as potential paths forward for this work.

1.7 REFERENCES

[1]   M.K. Hubbert, Science. 109 (1949) 103-109.

[2]   C. Okkerse, H. van Bekkum, Green Chemistry. 1 (1999) 107-114.

[3]   J. Fargione, J. Hill, D. Tilman, S. Polasky, P. Hawthorne, Science. 319 (2008) 1235-1238.

[4]   U.S.D.O. E, Energy Information Administration: Official Energy Statistics from the US Government. 2008 [cited 7/2008]; Available from: http://tonto.eia.doe.gov/oog/info/twip/twip_gasoline.html..

[5]   ExxonMobil, Energy Outlook: Global Transportation Demand. 2008 [cited 7/2008]; Available from: http://www.exxonmobil.com/Corporate/energy_outlook_gtd.aspx..

[6]   Energy Information Administration, US Department of Energy, 2009, pp. 1-274.

[7]   U.S.D.O. E, 2009. International Energy Outlook 2009. Energy Information Administration, US Department of Energy.

[8]   D.Q. S. Solomon, M. Manning, Z. Chen, M. Marquis, K. B. Averyt, M. Tignor, H. L. Miller, Cambridge, United Kingdom and New York, NY, USA 2007.

[9]   Energy Information Administration, US Department of Energy, 2008, pp. 1-54.

[10]   W.R.L. Anderegg, J.W. Prall, J. Harold, S.H. Schneider, Proc. Natl. Acad. Sci. U. S. A. 107 (2010) 12107-12109.

[11]   D. Tilman, J. Hill, C. Lehman, Science. 314 (2006) 1598-1600.

[12]   D. Ozcimen, F. Karaosmanoglu, Renewable Energy. 29 (2004) 779-787.

[13]   M. Jefferson, Renewable Energy. 31 (2006) 571-582.

[14]   A. Cadenas, S. Cabezudo, Technological Forecasting and Social Change. 58 (1998) 83-103.

[15]   M. Eggersdorfer, J. Meyer, P. Eckes, Fems Microbiology Reviews. 103 (1992) 355-364.

[16]   G.W. Huber, A. Corma, Angewandte Chemie - International Edition. 46 (2007) 7184-7201.

[17]   M. Ash, E. Dohlman, Electronic Outlook Report from the Economic Research Service, United States Department of Agriculture, 2007, pp. 1-83.

[18]   E. Lotero, Y. Liu, D.E. Lopez, K. Suwannakarn, D.A. Bruce, J.G. Goodwin Jr, Industrial and Engineering Chemistry Research. 44 (2005) 5353-5363.

[19]   EUBIA, *European Biomass Industry Association: Biodiesel*. 2008 [cited 7/2008]; Available from: http://www.eubia.org/214.0.html.

[20]   M.J. Haas, Fuel Processing Technology. 86 (2005) 1087-1096.

[21]   R. Pruszko, INFORM - International News on Fats, Oils and Related Materials. 17 (2006) 431-433.

[22]   M.J. Haas, S. Bloomer, K. Scott, Journal of the American Oil Chemists Society. 77 (2000) 373-379.

[23]   A.S. Ramadhas, S. Jayaraj, C. Muraleedharan, Fuel. 84 (2005) 335-340.

[24]   A. Demirbas, Energy Policy. 35 (2007) 4661-4670.

[25]   F.R. Ma, M.A. Hanna, Bioresource Technology. 70 (1999) 1-15.

[26]   G. Knothe, C.A. Sharp, T.W. Ryan, Energy & Fuels. 20 (2006) 403-408.

[27]   G. Knothe, INFORM - International News on Fats, Oils and Related Materials. 17 (2006) 729-731.

[28]   G. Knothe, Journal of the American Oil Chemists Society. 83 (2006) 823-833.

[29]   G. Knothe, Energy & Fuels. 22 (2008) 1358-1364.

[30]   G. Knothe, K.R. Steidley, Fuel. 86 (2007) 2560-2567.

[31]   A. Centeno, E. Laurent, B. Delmon, J. Catal. 154 (1995) 288-298.

[32]   J. Gusmão, D. Brodzki, G. Djéga-Mariadassou, R. Frety, Catal. Today. 5 (1989) 533-544.

[33]   E. Laurent, B. Delmon, Applied Catalysis A: General. 109 (1994) 77-96.

[34]   E. Laurent, B. Delmon, Applied Catalysis A: General. 109 (1994) 97-115.

[35]   O.I. Senol, T.R. Viljava, A.O.I. Krause, Elsevier Science Bv, 2005, pp. 331-335.

[36]   F.A. Twaiq, N.A.M. Zabidi, S. Bhatia, Ind. Eng. Chem. Res. 38 (1999) 3230-3237.

[37]   A. Demirbas, Fuel Process. Technol. 88 (2007) 591-597.

[38]   A. Demirbas, Energy Sources Part a-Recovery Utilization and Environmental Effects. 30 (2008) 1060-1064.

[39]   T. Danuthai, S. Jongpatiwut, T. Rirksomboon, S. Osuwan, D.E. Resasco, Applied Catalysis a-General. 361 (2009) 99-105.

[40]   T. Sooknoi, T. Danuthai, L.L. Lobban, R.G. Mallinson, D.E. Resasco, J. Catal. 258 (2008) 199-209.

[41]   T.J. Benson, R. Hernandez, M.G. White, W.T. French, E.E. Alley, W.E. Holmes, B. Thompson, Clean-Soil Air Water. 36 (2008) 652-656.

[42]   F.A. Twaiq, A.R. Mohamed, S. Bhatia, Microporous Mesoporous Mater. 64 (2003) 95-107.

[43]   P.T. Do, M. Chiappero, L.L. Lobban, D.E. Resasco, Catal. Lett. 130 (2009) 9-18.

[44]   J.T. Kloprogge, L.V. Duong, R.L. Frost, Environmental Geology. 47 (2005) 967-981.

[45]   M. Watanabe, T. Iida, H. Inomata, Energy Conversion and Management. 47 (2006) 3344-3350.

[46]   M. Snare, P. Maki-Arvela, I.L. Simakova, J. Myllyoja, D.Y. Murzin, Russian Journal of Physical Chemistry B. 3 (2009) 1035-1043.

[47]   NesteOil, 2007.

[48]   I. Simakova, O. Simakova, P. Maki-Arvela, A. Simakov, M. Estrada, D.Y. Murzin, Applied Catalysis a-General. 355 (2009) 100-108.

[49]   S. Lestari, P. Maki-Arvela, I. Simakova, J. Beltramini, G.Q.M. Lu, D.Y. Murzin, Catalysis Letters. 130 (2009) 48-51.

[50]   S. Lestari, P. Maki-Arvela, H. Bernas, O. Simakova, R. Sjoholm, J. Beltramini, G.Q.M. Lu, J. Myllyoja, I. Simakova, D.Y. Murzin, Energy & Fuels. 23 (2009) 3842-3845.

[51]   M. Snare, I. Kubickova, P. Maki-Arvela, D. Chichova, K. Eranen, D.Y. Murzin, Fuel. 87 (2008) 933-945.

[52]   P. Maki-Arvela, M. Snare, K. Eranen, J. Myllyoja, D.Y. Murzin, Fuel. 87 (2008) 3543-3549.

[53]   S. Lestari, I. Simakova, A. Tokarev, P. Maki-Arvela, K. Eranen, D.Y. Murzin, Catalysis Letters. 122 (2008) 247-251.

[54]   M. Snare, I. Kubickova, P. Maki-Arvela, K. Eranen, J. Warna, D.Y. Murzin, Chemical Engineering Journal. 134 (2007) 29-34.

[55]   P. Maki-Arvela, I. Kubickova, M. Snare, K. Eranen, D.Y. Murzin, Energy & Fuels. 21 (2007) 30-41.

[56]   M. Snare, I. Kubickova, P. Maki-Arvela, K. Eranen, D.Y. Murzin, Industrial & Engineering Chemistry Research. 45 (2006) 5708-5715.

[57]   I. Kubickova, M. Snare, K. Eranen, P. Maki-Arvela, D.Y. Murzin, Catalysis Today. 106 (2005) 197-200.

[58]   P. Maki-Arvela, J. Kuusisto, E.M. Sevilla, I. Simakova, J.P. Mikkola, J. Myllyoja, T. Salmi, D.Y. Murzin, Applied Catalysis a-General. 345 (2008) 201-212.

CHAPTER 2

SYNTHESIS AND CHARACTERIZATION OF A WELL-DEFINED

SUPPORTED PALLADIUM NANOPARTICLE CATALYST

2.1 Introduction

The goal of this work was the synthesis and complete characterization of a well-defined supported palladium nanoparticle catalyst, utilizing high palladium atom efficiency to maximize activity, but with the intent that any changes undergone by the catalyst during reaction could be analyzed via post-mortem characterization. A catalyst comprised of mono-dispersed nanoparticles evenly distributed throughout a porous, non-carbonaceous support was the basic intention to satisfy these requirements. This chapter will discuss different iterations of synthesized catalysts with varied supports, pre-treatments, metallation and reduction techniques.

2.2 Materials and Characterization Methods

The following chemicals were commercially available and used as received: Pluronic P123 EO-PO-EO triblock copolymer (P123, Sigma-Aldrich), 1,3,5-trimethylbenzene (TMB, 97%, Sigma-Aldrich), tetraethyl orthosilicate (TEOS, 98%, Sigma-Aldrich), 3-aminopropyltrimethoxysilane (APTMS, 97%, Sigma-Aldrich), 3-ureidopropyltrimethoxysilane (UPTMS, 97%, Sigma-Aldrich), 3-mercaptopropyltrimethoxysilane (MPTMS, 95%, TCI America), dodecane (anhydrous, Sigma-Aldrich), palladium(II) acetate (Pd(OAc)$_2$, 98%, Sigma-Aldrich), N,O-

bis(trimethylsilyl)acetamide (BSA, 95%, Sigma-Aldrich), pyridine (ACS grade >99%, Sigma-Aldrich), toluene (anhydrous, BDH), acetone (ACS grade, BDH), ethanol (reagent grade, BDH), ammonium fluoride (NH_4F, >96%, Alfa Aesar), hydrochloric acid (HCl, conc. 37%, J.T. Baker), dichloromethane (DCM, ACS grade, EMD chemicals), stearic acid (>97%, Fluka), sodium chloropalladate (Na_2PdCl_4, 99%, Aldrich), sodium borohydride ($NaBH_4$, 98%, Aldrich), tetraminepalladium chloride monohydrate ($Pd(NH_3)_4Cl_2 \cdot H_2O$, 98%, Aldrich), cetyl trimethylammonium bromide (CTAB, 98%, Aldrich), and ethyl stearate (>97%, Aldrich).

The materials discussed in this chapter were subjected to numerous characterization techniques, the individual details of which are outlined hereafter. Nitrogen adsorption isotherms were measured at 77K on a Micromeritics ASAP 2010. Surface area was determined by the Brunauer-Emmett-Teller method, in general using relative pressures less than 0.15. The Broekhoff-de Boer method with the Frenkel-Halsey-Hill (BdB-FHH) modification, applied first to these materials by Stucky et al. [1], was used to calculate pore size distributions. For detailed discussion of pore size distribution methodology comparisons, as well as VBA source code for the macro written to create these distributions, see Appendix A.

A Netzsch STA409 was used for thermogravimetric analysis (TGA) under an air flow diluted by nitrogen. Samples were heated under flow at 10 °C/min from 30 to 900 °C, with the total organic content estimated from the weight loss between 150 and 800 °C. Onboard differential scanning calorimetry (DSC) was used to identify peak temperatures of combustion exotherms.

Total active metal surface area was determined by H_2-O_2-H_2 titration chemisorption measurements in a Micromeritics AutoChem II 2920. For the highest active metal surface area accuracy, H_2-O_2 titrations are preferred over CO chemisorption due to the ambiguity of binding configuration of CO on a palladium surface [2]. To ensure full metal reduction, samples were reduced in 5% H_2 flow at 300 °C prior to analysis with sequential titrations of H_2 and O_2. H_2 uptake at room temperature was monitored by a thermal conductivity detector (TCD), and as in previous studies [3], background uptake titrations on the bare support confirm negligible uptake from the catalyst substrate.

Infrared spectra were acquired using KBr pellets with a Bruker Vertex 80v with dual FT-IR and FT-Raman benches and Ram-II module. Powder X-ray diffraction (XRD) patterns were obtained on a Philips Analytical X'Pert diffractometer, Cu-Kα radiation, equipped with an X'celerator detector and nickel filter. The scattered intensities were collected from 0.5° to 90° (2θ) by scanning at 0.008° (2θ) steps.

X-ray photoelectron spectroscopy (XPS) was performed on a powder sample grid with a Thermo Scientific K-Alpha XPS at room temperature and 10^{-8} mbar vacuum. For palladium 3d scans, a 200 µm incident spot size was measured with 0.1 eV step size between 329 and 347 eV and constant analyzer pass energy of 50 eV, using the carbon 1s binding energy of 284.8 eV as reference.

Extended X-ray absorption fine structure (EXAFS) spectra were acquired at the Argonne National Lab, using the synchrotron radiation at the Advanced Photon Source, Beamline 10-ID. Absorbance spectra were measured from 24.2 – 25.2 keV around the palladium k-edge (24.351 keV). Phase shift and backscattering amplitudes were obtained

from Pd foil. The EXAFS coordination parameters were obtained by a least square fit r-space of k^2–weighted Fourier transform data using standard procedures and WINXAS 3.1 software. The quality of the fits were equally good with both k^1 and k^3 weightings.

Scanning electron microscopy (SEM) was performed on sonicated and gold-sputtered samples using an Hitachi S-800 operating at 10 kV. Catalyst samples were also dispersed in ethanol and deposited on polymer/copper grids for analysis via transmission electron microscopy (TEM) on both a JEOL 100CX II (100kV) and an Hitachi HF-2000 field emission gun (FEG) (200kV). Power average particle size was estimated using quantitative dynamic light scattering (DLS) at room temperature on a Protein Solutions DynaPro DLS machine. Samples were diluted in toluene in a quartz cuvette, and histograms were created from an average of 100 measurements. Quantitative elemental analyses were performed by inductively coupled plasma optical emission spectrometry (ICP-OES) by Columbia Analytical Services, Tuscon AZ.

2.3 1ST Generation SBA-15 Supported Catalysts

Beginning with the knowledge that zero-valent palladium has been determined to be the most active metal for decarboxylation, our focus shifts to the novel and advantageous incorporation of palladium onto a well-defined solid support. The desired attributes of a good support material were (i) high surface area, with tunable pore size, (ii) high structural and chemical stability with respect to decarboxylation reactants, products, operating temperatures and pressures, and (iii) the ability to functionalize the exterior and pores, should surface modification be necessary. Additionally, meso-range porosity is preferred to minimize mass transfer limitations of the long-chain FFA in the

pores, as well as substantially increase the deposition threshold for potential pore blockage. We elected to begin with SBA-15, a periodic mesoporous amorphous silica that satisfies the preceding requirements.

2.3.1 Synthesis of 1ST Generation (SBA-15) Catalysts

Similar to literature methods [4, 5], SBA-15 is synthesized from the room-temperature polymerization of tetraethyl orthosilicate (TEOS) around micelles of non-ionic triblock copolymer (Pluronic 123) in an acidic aqueous solution. Following silica condensation, the mixture is subjected to hydrothermal aging, allowing the swelling of the pores. The final mesopore size and wall thickness can be controlled by the time and temperature of this step [5-8]. The aged material is then filtered, washed, and calcined in air to 823 K. A cartoon schematic (Figure 2.1) shows the formation of an ordered hexagonal array of two-dimensional cylindrical mesopores [9].
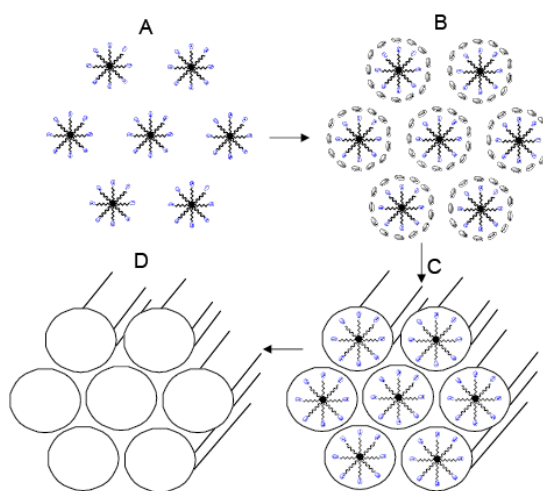
Figure 2.1 - Synthesis of SBA-15: (a) triblock copolymer micelle formation; (b) silica precursor condensation; (c) polymerization to form silica framework; (d) calcination to remove organic template (from [9])

Various methods to support nanoparticle catalysts on silica have been examined [10-26], a few of which were initially adapted and applied to our palladium on SBA-15 material [10, 17, 18]. We decided to avoid the difficulties of *ex situ* nanoparticle synthesis and subsequent silica tethering, and instead focused on incorporating metal precursor salts into the SBA-15 and forming nanoparticles *in situ*. Addition of the precursor salt was implemented in three different steps of the synthesis: (i) before the addition of silica source TEOS, (ii) after calcination, and (iii) after silane functionalization of the silica surface.

PdSBA15-1 was synthesized by modifying a literature method used for platinum nanoparticles [18]. To 99 g of DI H_2O, 1.0 g Pluronic 123 block copolymer (P123) and 370 mg cetyl trimethylammonium bromide (CTAB) were added and stirred for 4 h. To the solution, 2.5 mL of 0.024 M aqueous tetraminepalladium chloride (as $Pd(NH_3)_4Cl_2 \cdot H_2O$) was added and stirred for 24 h at room temperature. Before introducing the mixture to heat, 6.25mL concentrated (37%) HCl and 2.08g TEOS were added, making the final composition of the gel 1 TEOS : 585 H_2O : 6.3 HCl : 0.017 P123 : 0.01 CTAB : 0.006 $Pd(NH_3)_4Cl_2$. After 24 h of vigorous stirring at 40 °C, the mixture was autoclaved at 90 °C for 48 h, filtered, washed, dried, and calcined to 500 °C (2 °C/min). The same procedure was used to make PdSBA15-2, except with 2.5 mL of 0.024 M aqueous sodium tetrachloropalladate (as Na_2PdCl_4) as precursor salt.

SBA15-Pd^0 was produced by first suspending 500 mg as-synthesized SBA-15 in 100 mL DI H_2O. Li, et al. previously reported that increasing the pH of the suspension solution prior to ion-exchange deprotonates surface silanol groups to form Si-O$^-$ sites at which the adsorption of cationic metal precursor can occur via coulombic interactions

[17]. For this reason, 5% aqueous ammonium hydroxide was added dropwise to the reaction mixture until the pH was ~11. 65.15 mg of tetraminepalladium chloride monohydrate (0.247 mmol) dissolved in 50 mL DI H_2O was added to the flask, and the mixture was stirred at room temperature for 6 h. After solution reduction with excess aqueous $NaBH_4$ (noting a color change from brown to dark black), the SBA-15-Pd^0 was filtered, washed with subsequent aliquots of DI H_2O, ethanol, and diethyl ether, and dried *in vacuo* overnight.

It has been reported that silica functionalized with amine groups exhibit strong binding to ionic metal precursors, potentially yielding a final catalyst with evenly distributed nanoparticles [26]. To explore this method in our application, we first functionalized the SBA-15 with 3-aminopropyl ligands similar to literature methods [4]. Briefly, 1.0 g SBA-15 was suspended in anhydrous toluene, to which 1.0 g (excess) 3-aminopropyltrimethoxysilane (APTMS) was added. After stirring for 24 h under argon at room temperature, the aminosilica (3AP-SBA15) was filtered, washed with toluene, and dried *in vacuo* at 50 °C overnight. This material was metallated via two methods: (i) using the same method as for the above SBA15-Pd^0, except without the ammonium hydroxide pH adjustment (3AP-SBA15-Pd^0-1) and (ii) with the pH adjustment (3AP-SBA15-Pd^0-2).

2.3.2 Cursory Evaluation of 1st Generation Catalysts

A straightforward way to qualitatively contrast the aforementioned 1st generation catalyst syntheses was via transmission electron microscopy. The co-deposited catalyst PdSBA15-is shown in Figure 2.2. Large palladium nanoparticles are visible deposited

26

throughout the silica particle for PdSBA15-1. Most of these particles appear to be much

larger than the pore size of the SBA-15 (see Table 2.1), ruling out simple deposition

within the 6.1 nm diameter mesopores. Higher magnification images suggest structural

malformations around the palladium nanoparticles, indicating the presence of the metal is

altering the formation of long term order and periodicity of standard SBA-15 (Figure 2.3).

This disorder is reflected in the normalized pore volume and surface area which are much

lower than the bare SBA-15 silica (Table 2.1).
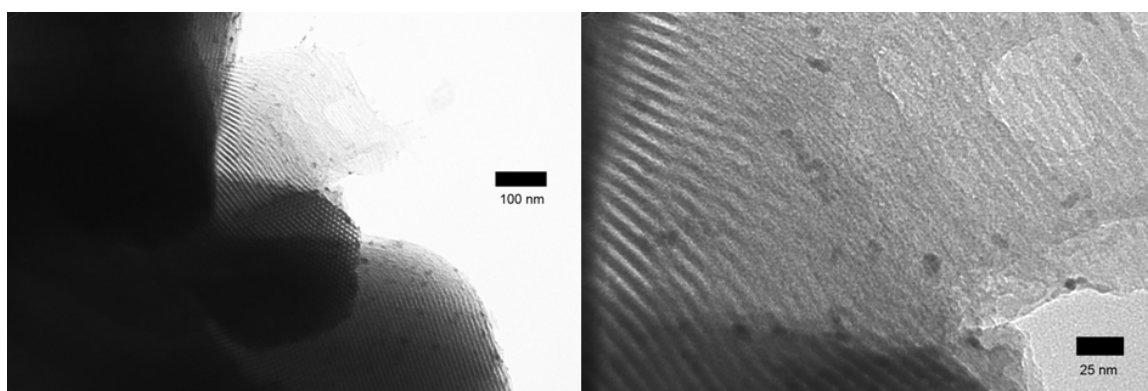
Figure 2.2 - TEM image of PdSBA15-1 showing dispersed nanoparticles at relatively low
loading

Table 2.1 – Nitrogen physisorption data for selected 1st generation catalysts (77K)

	SA ^{a} (m^2/g_{SiO2})	d_p ^{b} (nm)	V_p (cm^3/g_{SiO2})
SBA-15	960	6.4	0.87
PdSBA15-1	640	6.1	0.73
PdSBA15-2	940	6.5	0.86
3APSBA15	420	5.1	0.43
3APSBA15-Pd^0	290	4.9	0.21

^{a}BET ^{b}BdB-FHH
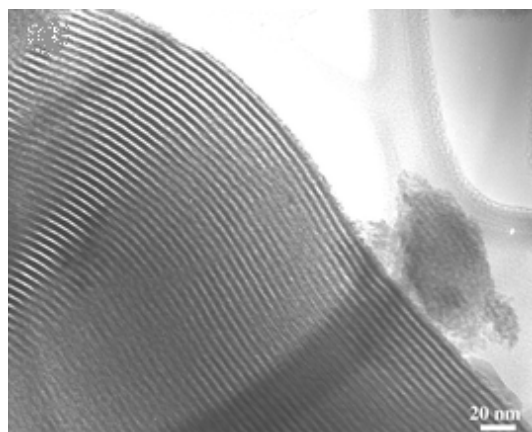
Figure 2.3 – TEM image of as-calcined SBA-15 silica.

Very little visual evidence of palladium nanoparticle formation is seen for PdSBA15-2, indicating negligible incorporation of the precursor palladium salt into silica material. Indeed, the SBA-15 structure appears unaffected and the physisorption indicates little change in porosity or surface area. Even at higher magnification, evidence of palladium particles is absent, and elemental analysis confirms palladium content less than the measureable limit. Due to the lack of deposited palladium within the substrate, co-synthesis of palladium nanoparticles and SBA-15 using sodium chloropalladate as precursor salt in the sol-gel was ruled out as a viable catalyst synthesis route.
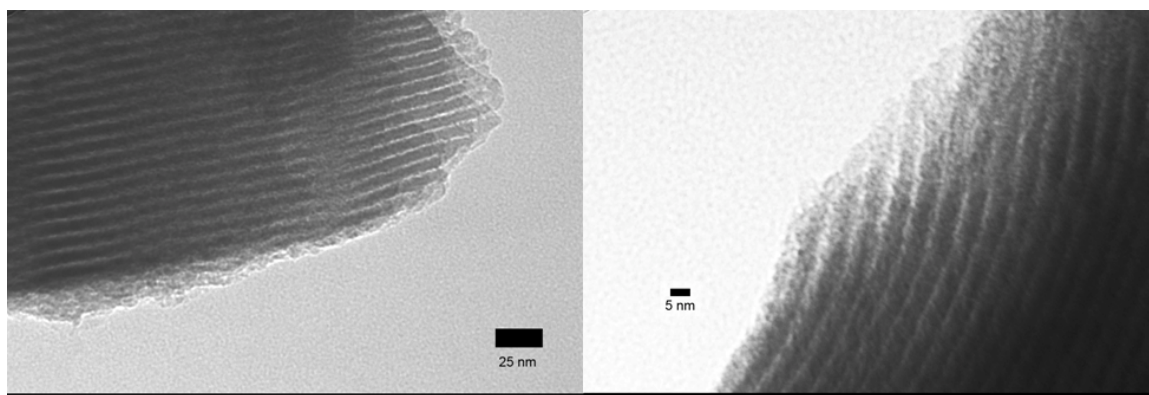
Figure 2.4 - PdSBA15-2: left, particle with no visible metal loading; right, higher magnification, little evidence of palladium nanoparticle formation

The as-calcined SBA-15 post-impregnated with palladium salt and solution reduced (SBA15-Pd0) is shown in Figure 2.5. Very large particles are shown deposited on the silica, showing very poor incorporation within the pores. Also apparent is substantial evidence to solution formation of bulk nanoparticles and subsequent aggregation and deposition on the silica surface. We attempted to avoid this bulk aggregation and deposition by pre-treating the silica surface with aminosilane ligands to induce ligation of the precursor salt throughout the particle prior to reduction (3APSBA15-Pd). Unfortunately, as shown in Figures 2.6 and 2.7, exterior deposition of palladium particles was unavoidable in liquid-phase reduction. However, a higher degree of in-pore incorporation is seen in the functionalized samples, especially 3APSBA15-Pd^0-2 (Figure 2.7), indicating better interaction with the palladium precursor.
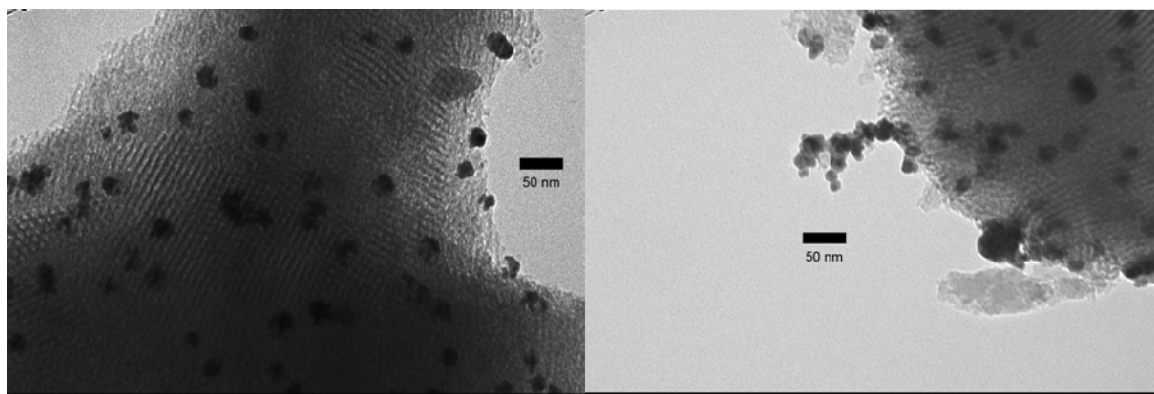
Figure 2.5 - TEM image of SBA15-Pd^0: left, large (ca. 15 - 25 nm) nanoparticles on the particle surface; right, aggregations of large nanoparticles formed in solution and deposited on the silica exterior
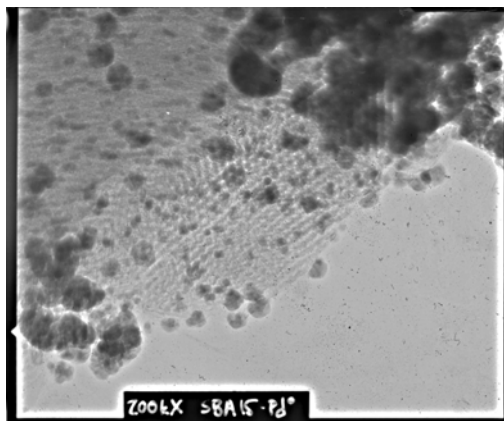
Figure 2.6 - TEM image of 3APSBA15-Pd^0-1 showing very large exterior Pd particles and poor incorporation into the pores
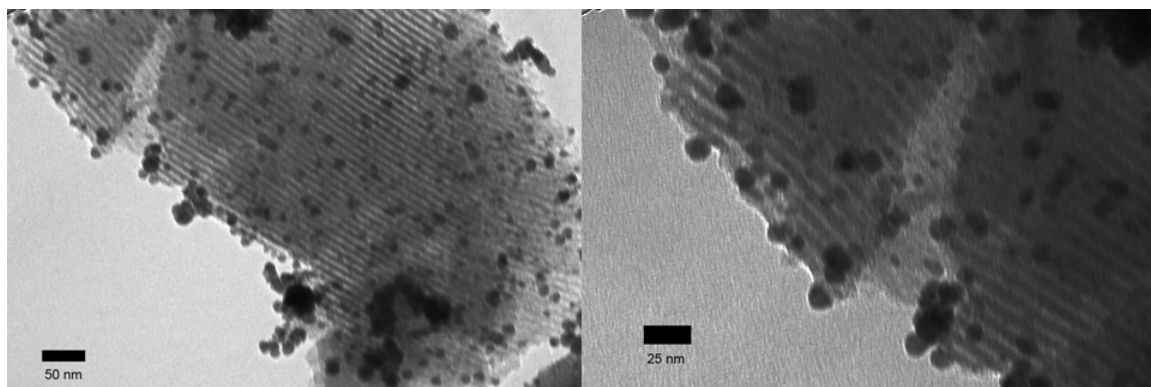
Figure 2.7 - TEM image of 3APSBA15-Pd^0-2 showing a high metal loading with particles both on the surface and filling the mesopores

It is apparent however that the particles deposited within the pores are large, i.e. approximately the same size as the pore itself, ~7nm. This is not only unfavorable from an atom efficiency standpoint (i.e., with larger nanoparticles, the majority of the metal atoms are inaccessible as interior atoms, at the expense of active catalytic binding sites on the surface), but each incorporated nanoparticle effectively blocks its respective pore. This loss of available are and volume are reflected in the physisorption data (Table 2.1) in both pore volume and surface area. It became a necessity to develop a different catalyst

system to ensure efficient deposition of dispersed nanoparticles; one with larger pore volume and much larger mesopores would be required to fully incorporate a high loading of palladium.

2.4 Silica MCF Supported Catalysts

Using what we learned in our initial synthesis experiments, here we present new, well-defined catalysts for the decarboxylation of FFA supported on well-defined porous oxides. Such structurally-defined catalysts, unlike typical commercial Pd/C catalysts, should engender subsequent development of structure-activity-deactivation characteristics that are critical to the detailed understanding of these catalysts. An ultra-large pore volume silica foam support (silica mesocellular foam, or MCF) [27] was now chosen to minimize the impact of internal mass transfer limitations and pore blockage. Silica MCF is synthesized via an extension of the SBA-15 sol-gel synthesis, modifying the gel stoichiometry and adding pore-swelling agents to effect the micelle self-assembly. The Stucky group has published an elegant manuscript detailing the structural transformation of SBA-15 to ordered MCF and finally disordered MCF via changing the sol-gel chemistry [28]. Simply described, as the ratio of swelling agent 1,3,5-trimethylbenzene to P123 triblock copolymer increases, the micelle assembly deviated from hexagonal packing into a disordered array of adjacent swollen micelles. A cartoon illustrating this effect is shown in Figure 2.8. The resultant foam has large spherical cells interconnected via smaller cylindrical windows, providing a three-dimensional porosity tunable via aging time and temperature, as well as the addition of mineralization salts [29]. Likewise, it has been shown that the overall silica foam particle morphology can be

controlled in the synthesis by closely controlling the agitation during the addition of the silica precursor [30].
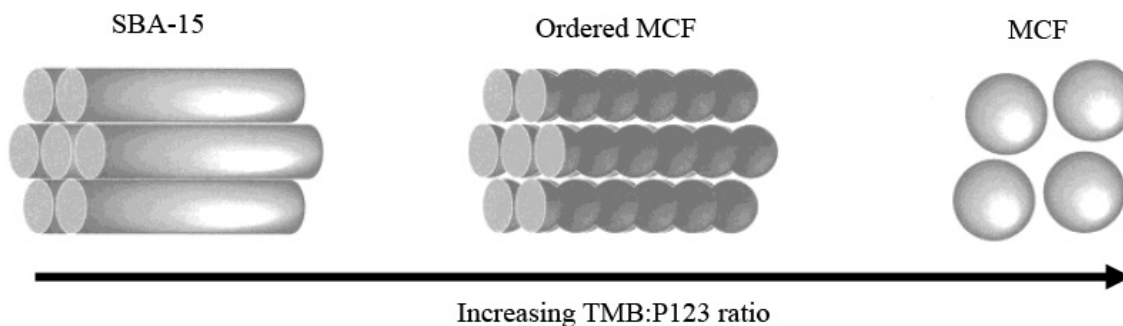
Figure 2.8 – Transition from SBA-15 hexagonally-ordered cylindrical mesopores to three-dimensional cell-and-window MCF pore structure

2.4.1 Synthesis of MCF and MCF Catalysts

2.4.1.1 Mesocellular Foam

Siliceous MCF was synthesized using a modified literature procedure [30]. As an example, 16.0 g P123 was dissolved in 260 g water with 47.4 g concentrated HCl in a capped 500 mL Erlenmeyer flask at room temperature. After complete copolymer dissolution, 16.0 g TMB were added and the solution was stirred vigorously at 39 °C for 2 hours, after which 34.6 g TEOS were added. The solution was stirred for an additional 5 minutes and then left quiescent for 20 hours in an oven at 40 °C. A total of 184 mg NH_4F (dissolved in 20 mL water) was added as a mineralization agent, and the mixture was briefly swirled before aging at 100 °C for an additional 24 hours. The resulting precipitate was filtered, washed with copious amounts of water, dried, and calcined in air

at 550 °C for 6 hours (1.2 °C min^{-1} ramp). A typical synthesis yielded 9.5 g silica MCF, >95% yield.

2.4.1.2 Precatalyst (MCF-X)

Organically functionalized precatalysts were synthesized by modifying the MCF support with three different silanes: UPTMS, MPTMS, and APTMS were used to make MCF-U, MCF-S, and MCF-N, respectively. The typical synthesis (Figure 2.9) began with refluxing under argon a mixture of 1.0 g dry MCF, 40 mL anhydrous toluene, and 5 mmol of the appropriate silane for 48 hours. The solid was then filtered and washed with toluene, ethanol, acetone, and DCM (3x25 mL), and then Soxhlet extracted with DCM for 48 hours to ensure complete removal of any excess unreacted silane. The resultant white powder was then dried overnight at 100 °C and 10 mtorr vacuum.
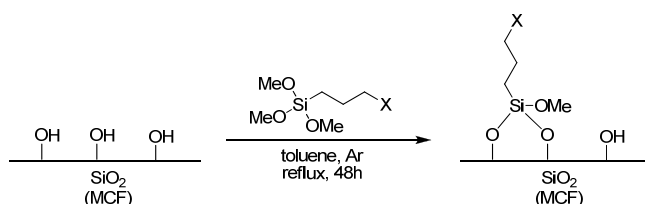
Figure 2.9 – Surface functionalization scheme of MCF-X precatalysts. X = SH, NH$_2$, NHCONH$_2$

2.4.1.3 Catalyst (Pd-MCF-X)

Metallation was carried out by mixing a solution of 62 mg Pd(OAc)$_2$ in 5 mL DCM with 0.5 g MCF-X suspended in 20 mL toluene for 24 hours at reflux. The solids were then filtered, washed with toluene and DCM, and dried under vacuum. The resultant metallated catalysts (nominally 5% Pd by weight) were calcined in air to 350 °C

(1.2 °C min^{-1}, 3 hours) to remove the acetate ligands and silane surface linkers, then reduced under 5% H$_2$ / 95% Ar gas flow at 300 °C for 3 hours (15 °C min^{-1} ramp) and stored in a nitrogen glove box until use. A sample of calcined, silane-free MCF was metallated via the same procedure for comparison, denoted Pd-MCF-bare.

2.4.2 Characterization and Evaluation of MCF Catalysts

2.4.2.1. Silica MCF

SEM images (Figure 2.10) of the calcined MCF show the quiescent synthesis yielded mostly spherical silica particles, as suggested by Han et al. [30], with average diameter approximately 2.5 μm. This estimated value is corroborated by the particle size distribution histogram derived from dynamic light scattering (DLS) measurements, shown in Figure 2.11. The N$_2$ physisorption data (Figure 2.12) exhibit typical Type IV isotherm characteristics, with loop hysteresis indicative of mesoporosity. The quantitative characterization of the distinct cell and window MCF mesopore structure is tabulated in Table 2.2 (refer to Appendix A for more detail in pore size calculations), and a characteristic bimodal BdB-FHH pore size distribution is represented in Figure 2.13. The aforementioned MCF synthesis method yields a silica support with reasonably high surface area (710 m^2/g) and ultra-large pore volume (2.9 cm^3/g), consisting of large hollow spherical cells (d_c = 37 nm) and three-dimensional interconnecting cylindrical windows (d_w = 17 nm). Small angle (0.5° – 5.0° 2θ) X-ray diffraction yields no discernible peaks, indicative of an essentially amorphous material. This loss of long-range order has been reported to occur with an average cell diameter greater than 30 nm [27], so is not an expected result for our synthesis method. This disordered foam pore

structure can be clearly seen in TEM images (Figure 2.14), with pore sizes matching those suggested by N_2 physisorption data.
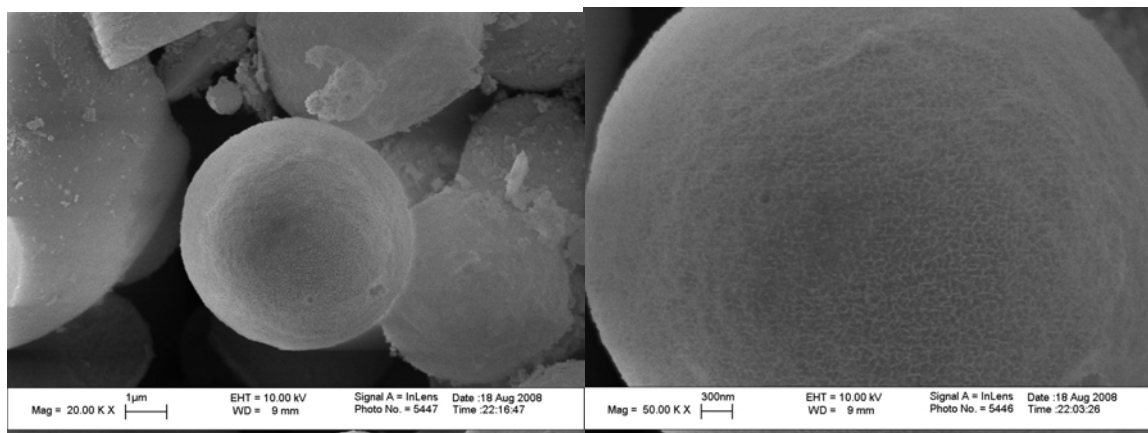
Figure 2.10 – SEM images of bare as-calcined silica MCF support.
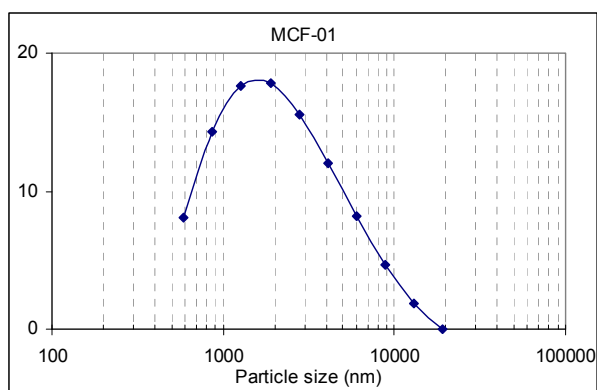
Figure 2.11 – DLS particle size distribution histogram for silica MCF
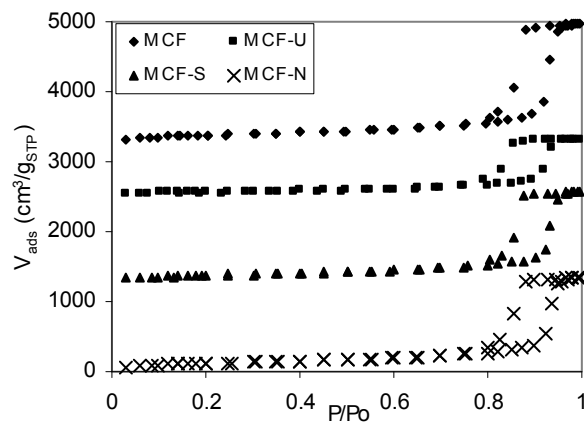
Figure 2.12 - N_2 adsorption/desorption isotherms for MCF and MCF-*X*. Isotherms are vertically offset as MCF +3200, MCF-U +2500, and MCF-S +1250 (cm^3/g STP).

Table 2.2 - N_2 physisorption data (77K) for MCF materials.

Sample	SA_{BET} (m^2/g_{SiO2})	V_{pore} (cm^3/g_{SiO2})	d_{cell}[a] (nm)	d_{window}[a] (nm)
MCF	710	2.9	37	17
MCF-U	550	1.9	34	15
MCF-S	590	2.3	37	17
MCF-N	650	2.5	34	17
Pd(OAc)$_2$-MCF-U	510	1.8	34	15
Pd(OAc)$_2$-MCF-S	580	2.2	37	15
Pd(OAc)$_2$-MCF-N	620	2.1	35	15
Pd-MCF-U	670	2.5	35	15
Pd-MCF-S	650	2.6	37	17
Pd-MCF-N	660	2.5	35	15

[a]Determined by BdB-FHH theory
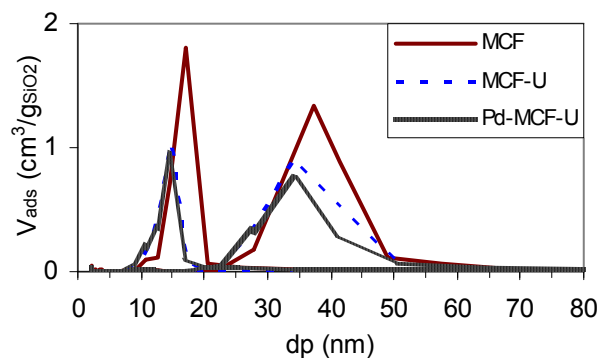
Figure 2.13 – Characteristic BdB-FHH pore size distribution for MCF materials. The right set of peaks is calculated from the N_2 adsorption isotherm and represents the diameters of the spherical cells. The left set of peaks is calculated from the desorption isotherm and represents the diameters of the cylindrical interconnecting windows. (See Appendix A for more detail.)
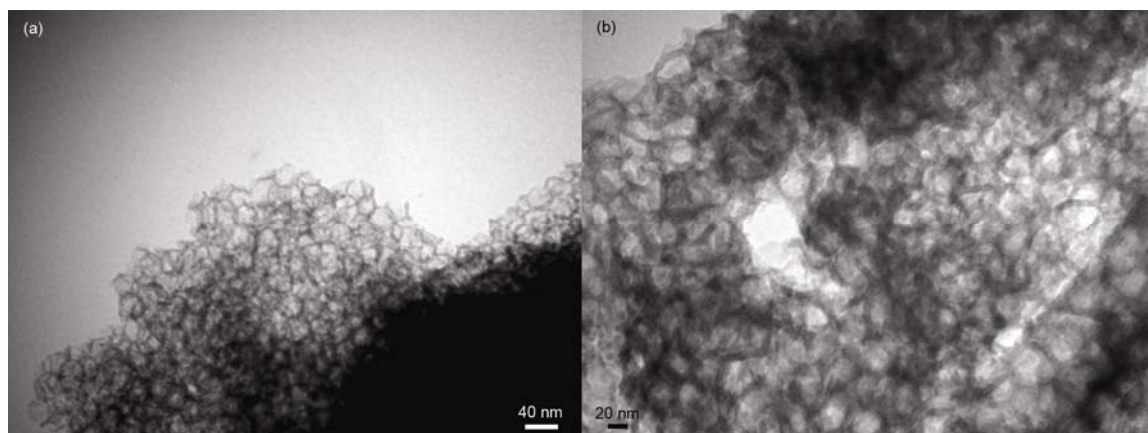
Figure 2.14 – TEM images of bare MCF support, clearly showing foam-like disordered cellular structure.

2.4.2.2 MCF-X and Pd-MCF-X

For comparative analysis, the organic loadings of the silane-functionalized MCF-X pre-catalysts were determined by TGA. Using identical reaction conditions, the ligand loadings on a per gram silica basis were 2.6 mmol (MCF-U), 0.73 mmol (MCF-S), and

1.5 mmol (MCF-N). As desired, all loadings were greater than the amount of palladium precursor (0.5 mmol), ensuring the metal precursor would not be added in excess.

Using the measured organic loadings, the physisorption data were normalized to a per gram silica basis and are shown in Table 2.2. The pre-catalysts all exhibit a decrease in surface area, pore volume, and average pore size, and upon metallation ($Pd(OAc)_2$-MCF-X) these decrease further. However, it is important to note that throughout these surface modifications, the inherent cell-and-window pore structure of the material remains intact, as indicated by the isotherm characteristics (Figure 2.12) and bimodal pore size distributions (Figure 2.13). A rebound in surface area, pore size and volume occurs after calcination and reduction, as the organic ligands are combusted and the resultant supported palladium oxide is reduced to metallic nanoparticles (Pd-MCF-X). This fresh form of the catalyst has relatively high surface area (~660 m^2/g), very high pore volume (~2.5 cm^3/g), and large accessible mesopores (35 nm cells, 15 nm windows).

Low resolution high contrast TEM images of the reduced catalysts are shown in Figure 2.15, and clearly a large number of small nanoparticles are evenly distributed throughout the silica support. To investigate this further, we obtained HRTEM images from Sandeep Kumar at the University of Minnesota (Figure 2.16) that illustrate palladium particles of approximately 2 nm inside the individual MCF cells. To independently determine the accessible palladium surface area and average nanoparticle size, H_2-O_2 titration chemisorption was performed.
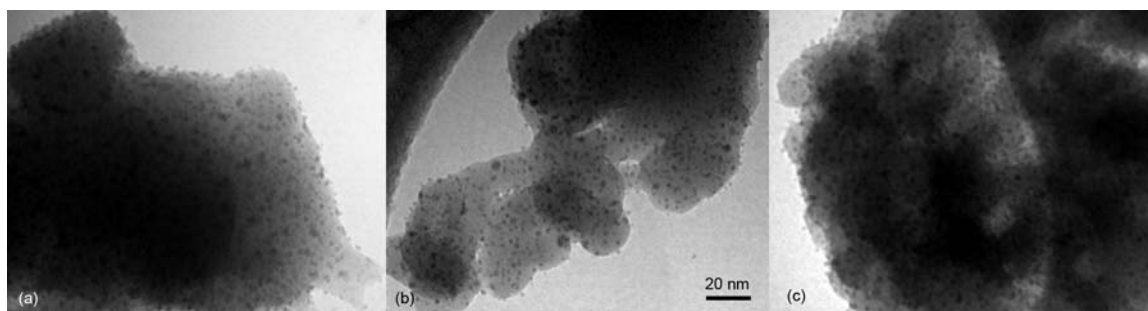
Figure 2.15 – TEM images of reduced catalysts: (a) Pd-MCF-U, (b) Pd-MCF-S, (c) Pd-MCF-N.
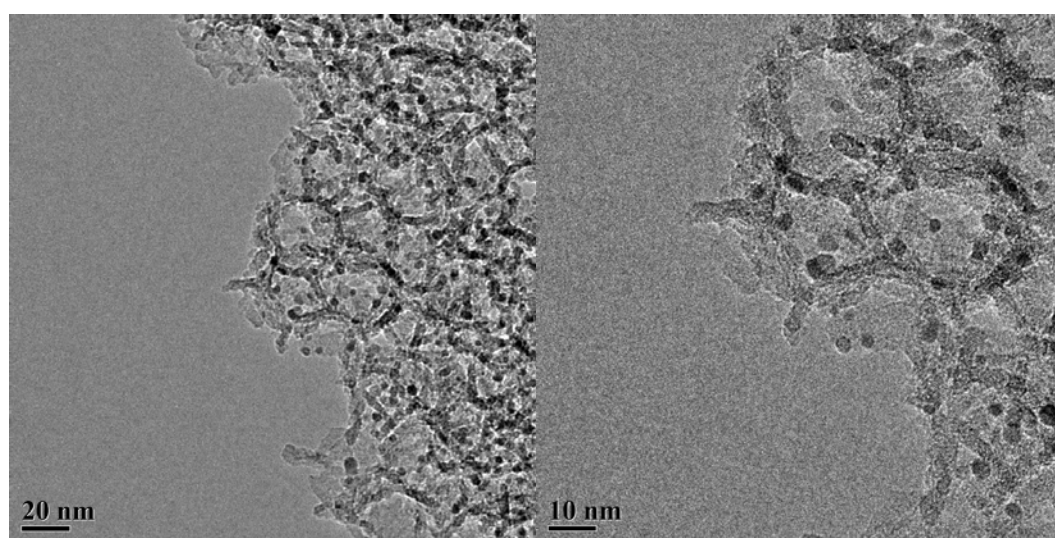
Figure 2.16 – HRTEM images of reduced Pd-MCF-U, clearly showing small Pd nanoparticle distributed throughout the MCF pore structure.

The chemisorption results (Table 2.3) show large and similar H_2 uptake for both Pd-MCF-U and Pd-MCF-N, and these values stay consistent through additional titration steps. Additionally, they correspond to an average nanoparticle size of ~ 2 nm, each utilizing a total palladium content of 5.5 wt% (via elemental analysis), which is nicely consistent with the TEM imaging. Pd-MCF-S, however, shows uptake values orders of magnitude lower, with large variations between titration repetitions, even though the

TEM image (Figure 2.15b) clearly shows nanoparticles present and elemental analysis shows 5.7 wt% palladium. This discrepancy was hypothesized occurring due to the formation of palladium sulfide (PdS) during the high temperature calcination and reductions. If this hypothesis was correct, there would be little zero valent palladium accessible in the Pd-MCF-S particles, making H_2 chemisorption uptake quantity an inaccurate value from which to calculate average nanoparticle size and metal dispersion (where dispersion is calculated as the ratio of number of surface atoms to number of total atoms in a particle).

To prove this hypothesis, we turned to extended X-ray absorption spectroscopy (EXAFS). Pd K-edge EXAFS spectra for three different samples are shown without phase correction in Figure 2.17. The spectrum drawn in blue represents supported zero-valent palladium nanoparticles, with the characteristic first nearest neighbor peak at 2.5 Å representing the Pd-Pd scattering path. A fully oxidized sample is represented as the black spectrum, exhibiting characteristics of bulk Pd oxide (PdO) nanoparticles. This is illustrated by the large nearest neighbor peak at much closer bond distance, at approximately 1.4 Å. The Pd-MCF-S sample is shown in red; the spectrum exhibits multiple characteristics to discuss. Firstly, there exists a Pd-Pd scattering peak at 2.5 Å, suggesting some existence of zero-valent palladium in the sample. However, the first nearest neighbor peak is at 1.7 Å, suggesting oxidized palladium species. Since the bond distance of the cationic palladium with its lattice counterion is larger than that of the Pd-O bond distance seen in the PdO sample, we can conclude that the element is larger than oxygen. In fact, the EXAFS spectrum of Pd-MCF-S fits theoretically very well with the incomplete formation of core-shell PdS/Pd nanoparticles—that is, a substantial Pd-S

nearest neighbor scattering path along with a residual metallic Pd-Pd path. This hypothesis explains the unexpected response in the H_2-O_2 chemisorption data, and is supported by physisorption, TEM, and EXAFS.

Table 2.3 - H_2-O_2 chemisorption data. Two data sets represent repeat titration cycles.

	Pd-MCF-bare		Pd-MCF-U		Pd-MCF-S		Pd-MCF-N	
Cumulative uptake (cm^3/g STP)	1.66	1.51	6.85	6.49	0.28	0.06	6.30	6.42
Pd surface area (m^2/g$_{sample}$)	3.5	3.2	14.4	13.7	0.60	0.13	13.1	13.5
Pd surface area (m^2/g$_{Pd}$)	64	58	263	250	11	2.5	240	244
Particle diameter (nm)	7.8	8.5	1.91	1.99	-	-	2.06	2.03
Pd dispersion (%)	14.4	8.5	59.1	56.2	-	-	54.3	55.0
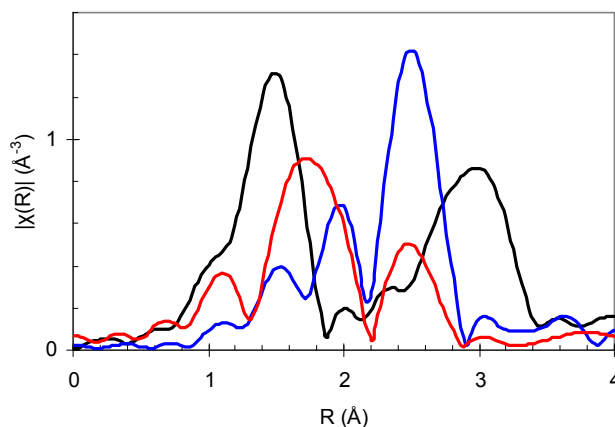
Figure 2.17 – EXAFS spectra MCF supported palladium materials: PdO nanoparticles (black line), Pd nanoparticles (blue line), and Pd-MCF-S (red line).

The metallated bare MCF (Pd-MCF-bare, 4.8 wt% via elemental analysis) exhibits a fraction of the active metal surface area of those catalysts prepared from a functionalized precatalyst. Distributing a palladium-complexing silane ligand throughout the silica prior to introduction of the metal precursor allows us to achieve extremely high and uniform particle dispersion not often seen in a material containing a metal loading of

41

>5 wt%. The palladium is distributed throughout the silica particle and is fully accessible by large mesopores, making the Pd-MCF-U and Pd-MCF-N ideal catalyst candidates for overall palladium availability and low internal mass transfer limitations.

2.5 Conclusions

Many initial attempts to make a well-defined palladium nanoparticle catalyst utilizing SBA-15 as support were unsuccessful. Attempted metal incorporation concurrent with the support synthesis resulted in limited deposition with structural defects in the mesostructure, or no metal content at all. Various iterations of post-synthesis metallation were performed, with the propyl-amine functionalized SBA-15 yielding the best results. Unfortunately, the average palladium particle size was still quite large (~6 nm), and a large amount of solution-phase reduction and subsequent aggregation and surface deposition occurred. Physisorption characterization indicated nanoparticle pore-blockage as well, limited the useful surface area and pore volume for catalysis. To alleviate these constrictions, the transition to a three-dimensional ultra-large pore volume MCF support was made. The MCF was functionalized with three different silanes to act as palladium precursor salt scavenging precatalysts: thiol, amine, and urea. After metallation, extensive characterization was performed, and small nanoparticles were prevalent throughout the MCF particles in all cases. However, in the material pre-functionalized with thiol silane, the nanoparticles formed had negligible surface area active for hydrogen adsorption, and were found via EXAFS to be palladium sulfide nanoparticles instead of zero-valent Pd. On the other hand, the Pd-MCF-U and Pd-MCF-N catalysts satisfied our requirements of a well-defined, highly loaded palladium

nanoparticle catalyst to move forward with activity studies. These evenly-distributed, ~2 nm palladium nanoparticles were successfully synthesized with 55% - 60% dispersion in a 5 wt% palladium material—a dispersion heretofore unseen in the literature for a material with as high metal loading.

2.6 REFERENCES

[1]   W.W. Lukens, P. Schmidt-Winkel, D.Y. Zhao, J.L. Feng, G.D. Stucky, Langmuir. 15 (1999) 5403-5409.

[2]   D. Loffreda, D. Simon, P. Sautet, Surf. Sci. 425 (1999) 68-80.

[3]   E.W. Ping, R. Wallace, J. Pierson, T.F. Fuller, C.W. Jones, Microporous Mesoporous Mater. 132 (2010) 174-180.

[4]   J.C. Hicks, C.W. Jones, Langmuir. 22 (2006) 2676-2681.

[5]   D.Y. Zhao, Q.S. Huo, J.L. Feng, B.F. Chmelka, G.D. Stucky, J. Am. Chem. Soc. 120 (1998) 6024-6036.

[6]   M. Kruk, M. Jaroniec, C.H. Ko, R. Ryoo, Chem. Mater. 12 (2000) 1961-1968.

[7]   J.S. Lee, S.H. Joo, R. Ryoo, J. Am. Chem. Soc. 124 (2002) 1156-1157.

[8]   P. Van der Voort, M. Benjelloun, E.F. Vansant, J. Phys. Chem. B. 106 (2002) 9027-9032.

[9]   J.C. Hicks, Chemical and Biomolecular Engineering, Georgia Institute of Technology, Atlanta, 2007, p. 207.

[10]   P. Han, X.M. Wang, X.P. Qiu, X.L. Ji, L.X. Gao, Journal of Molecular Catalysis a-Chemical. 272 (2007) 136-141.

[11]   Y.X. Jiang, N. Ding, S.G. Sun, Journal of Electroanalytical Chemistry. 563 (2004) 15-21.

[12]   F. Kleitz, S.H. Choi, R. Ryoo, Chemical Communications (2003) 2136-2137.

[13]   Z. Konya, E. Molnar, G. Tasi, K. Niesz, G.A. Somorjai, I. Kiricsi, Catalysis Letters. 113 (2007) 19-28.

[14]   Z. Konya, V.F. Puntes, I. Kiricsi, J. Zhu, P. Alivisatos, G.A. Somorjai, Catalysis Letters. 81 (2002) 137-140.

[15]   S.S. Lee, B.K. Park, S.H. Byeon, F. Chang, H. Kim, Chemistry of Materials. 18 (2006) 5631-5633.

[16]   S.S. Lee, H.I. Park, B.K. Park, S.H. Byeon, Materials Science and Engineering B-Solid State Materials for Advanced Technology. 135 (2006) 20-24.

[17]   C.L. Li, Q.H. Zhang, Y. Wang, H.L. Wan, Catalysis Letters. 120 (2008) 126-136.

[18]   A.K. Prashar, R.P. Hodgkins, R. Kumar, R.N. Devi, Journal of Materials Chemistry. 18 (2008) 1765-1770.

[19]   H. Song, R.M. Rioux, J.D. Hoefelmeyer, R. Komor, K. Niesz, M. Grass, P.D. Yang, G.A. Somorjai, Journal of the American Chemical Society. 128 (2006) 3027-3037.

[20]   A. Taguchi, F. Schuth, Microporous and Mesoporous Materials. 77 (2005) 1-45.

[21]   J.Y. Ying, C.P. Mehnert, M.S. Wong, Angewandte Chemie-International Edition. 38 (1999) 56-77.

[22]   I. Yuranov, L. Kiwi-Minsker, P. Buffat, A. Renken, Chemistry of Materials. 16 (2004) 760-761.

[23]   I. Yuranov, P. Moeckli, E. Suvorova, P. Buffat, L. Kiwi-Minsker, A. Renken, Journal of Molecular Catalysis a-Chemical. 192 (2003) 239-251.

[24]   J. Zhu, Z. Konya, V.F. Puntes, I. Kiricsi, C.X. Miao, J.W. Ager, A.P. Alivisatos, G.A. Somorjai, Langmuir. 19 (2003) 4396-4401.

[25]   S.M. Zhu, H.S.S. Zhou, M. Hibino, I. Honma, Journal of Materials Chemistry. 13 (2003) 1115-1118.

[26]   R. Trivedi, S. Roy, M. Roy, B. Sreedhar, M.L. Kantam, New Journal of Chemistry. 31 (2007) 1575-1578.

[27]   P. Schmidt-Winkel, W.W. Lukens, D.Y. Zhao, P.D. Yang, B.F. Chmelka, G.D. Stucky, J. Am. Chem. Soc. 121 (1999) 254-255.

[28]   J.S. Lettow, Y.J. Han, P. Schmidt-Winkel, P.D. Yang, D.Y. Zhao, G.D. Stucky, J.Y. Ying, Langmuir. 16 (2000) 8291-8295.

[29]   P. Schmidt-Winkel, W.W. Lukens, P.D. Yang, D.I. Margolese, J.S. Lettow, J.Y. Ying, G.D. Stucky, Chem. Mater. 12 (2000) 686-696.

[30]   Y. Han, S.S. Lee, J.Y. Ying, Chem. Mater. 19 (2007) 2292-2298.

CHAPTER 3

DECARBOXYLATION OF MODEL COMPOUNDS AND MIXTURES

3.1 Introduction

The goal of this section is to begin to apply the catalysts discussed in Chapter 2 to the problem outlined in Chapter 1—that is, to attempt to make diesel fuel-length hydrocarbons from low-cost biofeedstock analogues. With the initial motivation for this decarboxylation work coming from the challenge of upgrading a poultry-derived brown grease, we turned to its general composition to survey model compounds. This brown grease from a local poultry rendering facility (American Proteins, Toccoa GA) was analyzed for lipid and FFA content via gas chromatography, and the fatty acid carbon chain length distribution is shown in Figure 3.1. Acids of carbon chain length 18 are clearly the most prevalent, and together saturated and monounsaturated C_{16} and C_{18} acids account for nearly 90% of the total fatty acids.
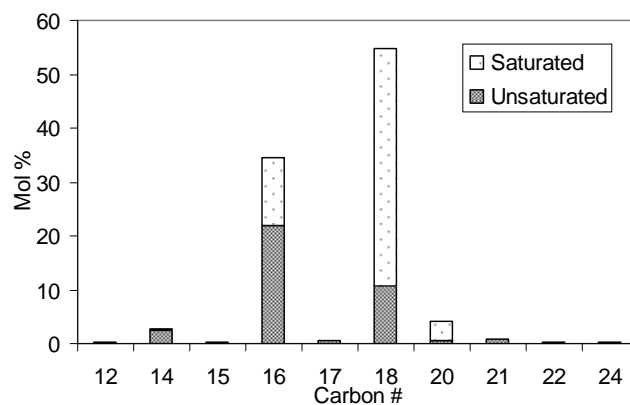
Figure 3.1 - Fatty acid carbon chain length distribution of wastewater brown grease feedstock candidate.

These values fit in well with published compositions of many high-acid biofeedstocks, including plant oils and other animal byproducts (Table 3.1). With the majority of acid content being C_{16} and C_{18}, and the potential hydrocarbon products n-C_{15} and n-C_{17} being applicable as drop-in diesel fuels, initially examining catalyst activity using stearic acid (C18:0) is easily justified.

Table 3.1 – Fatty acid composition of different high-acid biofeedstocks (Data from [1-8])

	fatty acid composition (wt %)						
	myristic (14:0)	palmitic (16:0)	palmitoleic (16:1)	stearic (18:0)	oleic (18:1)	linoleic (18:02)	linolenic (18:3)
rapeseed oil		3.5		0.9	64.4	22.3	8.2
virgin olive oil		9.2	0.8	3.4	80.4	4.5	0.6
sunflower oil		6.0		4.2	18.7	69.3	
safflower oil		5.2		2.2	76.3	16.2	
soybean oil	0.1	10.6		4.8	22.5	52.3	8.2
palm oil	1.2	47.9		4.2	37.0	9.1	0.3
white grease		23.3	3.5	11.0	47.1	11.0	1.0
poultry fat		22.2	8.4	5.1	42.3	19.3	1.0
lard	1.7	17.3	1.9	15.6	42.5	9.2	0.4
edible tallow	4.8	28.4		14.8	44.6	2.7	
yellow grease	2.4	23.2	3.8	13.0	44.3	7.0	0.7
brown grease	1.7	22.8	3.1	12.5	42.4	12.1	0.8

Of course, additional model acids will be discussed herein, including those with varying chain lengths and degrees of unsaturation. Likewise, alkyl ester derivatives, mixtures of acids, and common additives like glycerol and propylene glycol were tested for activity at reaction conditions. The goal of this work was not only to show that our synthesized catalysts have high and robust decarboxylation activity, but also to develop

an understanding of the reaction scheme when dealing with multi-component mixtures to provide insight for later reactions with real feedstocks.

3.2 Experimental Methods

3.2.1 Materials

The following chemicals were commercially available and used as received: dodecane (anhydrous, Sigma-Aldrich), N,O-bis(trimethylsilyl)acetamide (BSA, 95%, Sigma-Aldrich), pyridine (ACS grade >99%, Sigma-Aldrich), toluene (anhydrous, BDH), acetone (ACS grade, BDH), ethanol (reagent grade, BDH), dichloromethane (DCM, ACS grade, EMD chemicals), stearic acid (>97%, Fluka), glycerol (>98%, Aldrich), palmitic acid (95%, Aldrich), oleic acid (98%, EMD), palmitoleic acid (97%, EMD), propylene glycol (99%, Aldrich), and ethyl stearate (>97%, Aldrich). Tridecane was purchased from Sigma-Aldrich and distilled over CaH_2. Pd-MCF-X catalysts were synthesized as described in used as described in Chapter 2 (and [9]).

3.2.2 General Stearic Acid Decarboxylation Procedure

The Pd-catalyzed decarboxylation of stearic acid was carried out in batch in a 300 °C oil bath. Typically, 15 mL pressure reactors were charged in a nitrogen glove box with 25 mg reduced Pd-MCF-X and 2.7 mL of 0.15 M stearic acid in dodecane. For kinetic studies, each time point corresponded to an individual tube, and 50 μL tridecane were used as internal standard. The tubes were placed in the preheated oil bath and magnetically stirred for up to 6 hours before removal and thermal quench in a cold silicone oil bath. A sample of the reactor contents was extracted via syringe and stirred

with pyridine and BSA for 1 hour at 60 °C to silylate any remaining carboxylic acid moieties. This allowed for the now-silylated stearic acid to elute through the GC column and be quantitatively analyzed. A gas chromatograph with flame ionization detector (GC-FID) (Shimadzu GC-2010), equipped with an SHRX5 column (15m, 0.25µm film thickness, 0.25mm i.d.), was used for quantitative analysis of the decarboxylation reactions.

3.2.3 Decarboxylation of Other Compounds

Decarboxylation kinetics of palmitic acid and batch decarboxylation of ethyl stearate were performed by the same procedure as described for stearic acid in Section 3.2.2. Because the characterization for the amine-based catalyst and urea-based catalyst is nearly identical (see Chapter 2), for the sake of comparison fidelity, all subsequent decarboxylation reactions were catalyzed with the Pd-MCF catalyst made from the urea-functionalized precatalyst (Pd-MCF-U). Decarboxylation reactions with unsaturated acids (oleic acid, palmitoleic acid, linoleic acid, etc.) and other compounds for which H_2 was necessary were carried out in a 30 mL stainless steel stirred Parr reactor. In general, the reactor bomb was charged with 250 mg pre-reduced Pd-MCF, 3.0 mmol reactant, and 25 mL dodecane. The reactor was then closed, purged with argon and hydrogen, charged with the desired gas, and ramped to 300 °C via temperature-controlled heating jacket (approximately 20 minutes to reach 300 °C from 25 °C). The reactor was stirred at approximately 500 rpm for the duration of the reaction. Semi-batch reactions are carried out under 10 mL/min hydrogen flow. Gas analysis was performed via balloon transfer and direct injection into a gas chromatograph equipped with an HP-PLOT S column and

TCD detector for analysis of hydrogen, CO, CO_2, and light hydrocarbon products. Liquid product analysis was carried out as described for stearic acid. External standards were used for both gas and liquid phase GC product identification.

3.3 Results and Discussion

3.3.1 Batch Decarboxylation Kinetics of Stearic Acid

Batch decarboxylation of stearic acid over Pd-MCF-X catalysts was performed at 300 °C for up to 6 hours. Conversion of stearic acid to *n*-heptadecane after 6 hours was 89.1%, 37%, and 84.8% for Pd-MCF-U, Pd-MCF-S, and Pd-MCF-N respectively, with no quantifiable appearance of side products. A typical kinetic plot is shown in Figure 3.2, which highlights the similarities in performance of Pd-MCF-U and Pd-MCF-N catalysts. Their comparable activities are expected, as the material properties of the reduced catalysts are quite similar, evidenced in Chapter 2 by physisorption, TEM, and chemisorption. Similarly, the poor activity of Pd-MCF-S was predicted by the lack of accessible active area during H_2-O_2 titration chemisorption; since the palladium sulfide particles have few active sites for probe hydrogen adsorption, their inability to efficiently activate the reactants under reaction conditions is expected. Additionally shown is the kinetic profile for the Pd-MCF-bare catalyst, exhibiting lower conversions than the catalysts pre-functionalized with amine or urea. This activity deviation is expected due to the lower amount of available palladium as quantified by chemisorption titrations. It should be noted however that a four-fold decrease in probe uptake does not necessarily translate directly to a four-fold decrease in stearic acid conversion; parallel competing

rates likely exist, e.g. primary reaction rate of decarboxylation and rate of catalyst deactivation (see Chapter 4).
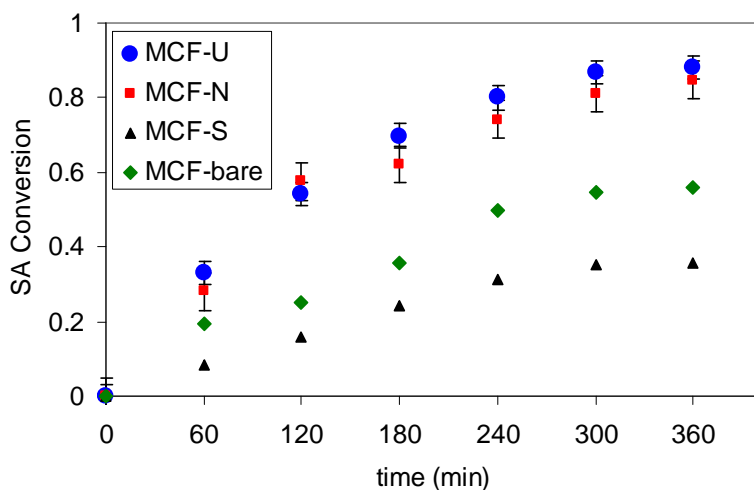
Figure 3.2 – Decarboxylation kinetics of 0.15 M stearic acid at 300 °C, N_2 atmosphere.

3.3.2 Batch Decarboxylation of Ethyl Stearate

Batch decarboxylation of ethyl stearate was performed over Pd-MCF-U and Pd-MCF-N under inert N_2 atmosphere at 300 °C for 6 hours. As seen in Figure 3.3, conversions of less than 15% were obtained, with approximately 87% selectivity after 6 hours to *n*-heptadecane, and the remaining 13% to stearic acid. Murzin et al. have reported that the free carboxylic acid is not a side product in this reaction, but instead a necessary intermediate in the decarboxylation of alkyl esters in the absence of hydrogen [10]. In other words, before decarboxylation can occur, ethylene must be evolved to form the stearic acid intermediate. This was supported by our preliminary results, and provided another piece to the overall reaction scheme. The low overall conversions

attained by Pd-MCF-X catalysts are similar to those reported in literature for related catalysts and alkyl esters in N_2 atmosphere [11].
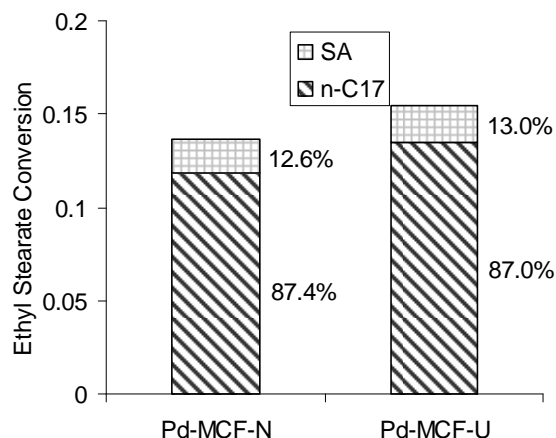
Figure 3.3 - Decarboxylation of 0.15 M ethyl stearate, 360 minutes, 300 °C, N_2 atmosphere.

3.3.3 Hydrogenation and Decarboxylation of Unsaturated Acids

Batch decarboxylation of oleic acid was initially attempted with an inert argon atmosphere, with 6-hour conversions of 40% observed. The selectivity to the decarboxylated alkane was essentially zero, however, with the main products being heavy oligomers. Similar results were seen using palmitoleic and linoleic acids (Table 3.2). These results were in agreement with previous publications reporting that unsaturated reactants will crosslink if no hydrogen source is present [12]. Running the same reactions with hydrogen as the reaction atmosphere yields dramatically different results (Table 3.3). Complete conversion of the unsaturated acids is achieved, with selectivity to the decarboxylated product alkane approximately equivalent to those seen with fully saturated reactants. Negligible dimeric or oligomeric sideproducts are formed; the remaining reactant is present in its fully saturated form, as stearic acid.

53

To further probe the sequence of this reaction, the reactor was charged with the same reactants, ramped from room temperature to 300 °C, and immediately quenched for analysis. The charged stainless steel reactor took approximately 20 minutes to reach reaction temperature, and was stirred for the duration of the temperature ramp. Reaction mixture composition for this initial time point is shown in Table 3.4. In the presence of hydrogen gas, the unsaturated fatty acids are completely hydrogenated by the time the reaction reaches its holding temperature, after which the dominant reaction mode is essentially the decarboxylation of stearic acid, which we've thoroughly studied. Some small amount of decarboxylation has managed to occur during the short period of time the reactor is at high temperature, which is acceptable given reports of relatively slow decarboxylation beginning to occur upwards of 280 °C [13]. The hydrogenation though is fully completed by these temperatures, which is not surprising given that supported palladium catalysts have been identified as efficient hydrogenation catalysts for over a century [14], and have been shown active in gas phase hydrogenations at temperatures lower below 100 °C [15]. Additionally, reports were recently published of complete hydrogenation of linoleic acid to stearic acid under hydrogen flow at 200 °C [16]. The hypothesized stepwise reaction pathway involving initial hydrogenation followed by decarboxylation was supported by these results.

Table 3.2 – Reaction results for unsaturated acids under Argon at 300 °C, t = 6 hours.

	Conversion (6 h)	Selectivity (%)					
		n-C_{17} [a]	C_{18} [b]	C_{35} [c]	heavy [d]	crack [e]	other
Oleic acid	40%	< 1	8	2	84	1	5
Linoleic acid	36%	< 1	7	1	88	2	2
Linolenic acid	43%	< 1	8	1	87	2	2

[a]decarboxylated product, [b]other C_{18} acids, [c]coupled ketone sideproduct, [d]C_{36}+ dimeric and oligomeric products, [e]C_5-C_{16} acids and hydrocarbons

Table 3.3 – Reaction results for unsaturated acids under H_2 at 300 °C, t = 6 hours.

	Conversion (6 h)	Selectivity (%)					
		n-C_{17} [a]	$C_{18:0}$ [b]	$C_{18:x}$ [c]	heavy [d]	crack [e]	other
Oleic acid	100%	91	8	0	0	0	< 1
Linoleic acid	100%	93	7	0	0	0	< 1
Linolenic acid	100%	89	9	< 1	0	0	< 1

[a]decarboxylated product, [b]stearic acid, [c]unsaturated acids, [d]C_{36}+ dimeric and oligomeric products, [e]C_5-C_{16} acids and hydrocarbons

Table 3.4 – Reaction results for unsaturated acids under H_2 after temperature ramp to 300 °C.

	Conversion	Selectivity (%)					
		n-C_{17} [a]	$C_{18:0}$ [b]	$C_{18:x}$ [c]	heavy [d]	crack [e]	other
Oleic acid	100%	7	93	0	0	0	< 1
Linoleic acid	98%	5	94	< 1	0	0	< 1
Linolenic acid	98%	5	93	2	0	0	< 1

[a]decarboxylated product, [b]stearic acid, [c]unsaturated acids, [d]C_{36}+ dimeric and oligomeric products, [e]C_5-C_{16} acids and hydrocarbons

3.3.4 Decarboxylation of Palmitic acid, Glycerol and Mixtures

As a simple comparison of relative reactivity of different acid chain lengths, we examined the decarboxylation kinetics of palmitic acid (C16:0) in inert atmosphere. As previously discussed, 16-carbon acids account for the vast majority of acid and lipid compounds in candidate biofeedstocks along with C18, so the addition of palmitic acid to this study was an obvious choice. In fact, the study of palmitic acid decarboxylation was quite trivial—the kinetics of decarboxylation at 300 °C over Pd-MCF are shown in Figure 3.4, overlaid with those of stearic acid under the same reaction conditions. The conversion of palmitic acid to the decarboxylated alkane *n*-pentadecane   occurred at approximately the same rate as that of stearic acid to *n*-heptadecane.
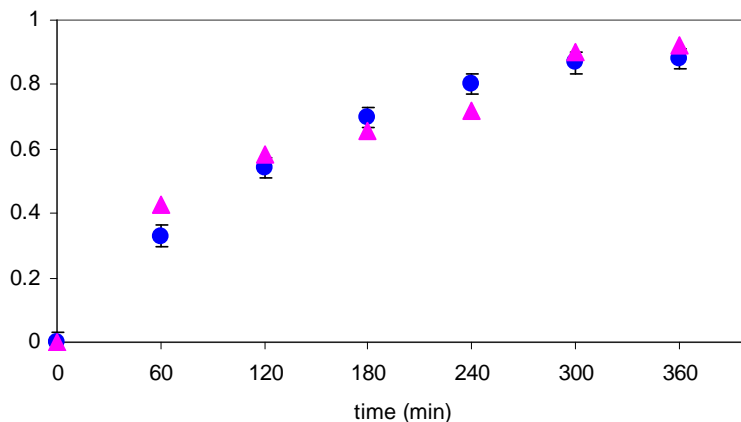
Figure 3.4 – Decarboxylation of palmitic acid (pink) and stearic acid (blue) in dodecane with Pd-MCF catalyst at 300 °C under N_2

Figure 3.5 represents the proposed reaction pathway for saturated and unsaturated fatty acids and their alkyl derivatives, using C_{18} acid-based reactants as a model system. Unsaturated acids are quickly hydrogenated to full saturation prior to decarboxylation,

and alkyl esters must undergo dealkylation before decarboxylation to the product alkane. Unsaturated alkyl esters were found to mainly hydrogenate to the fully saturated alkyl esters prior to dealkylation, but there has been some evidence of unsaturated dealkylation so the pathway has been included [11].
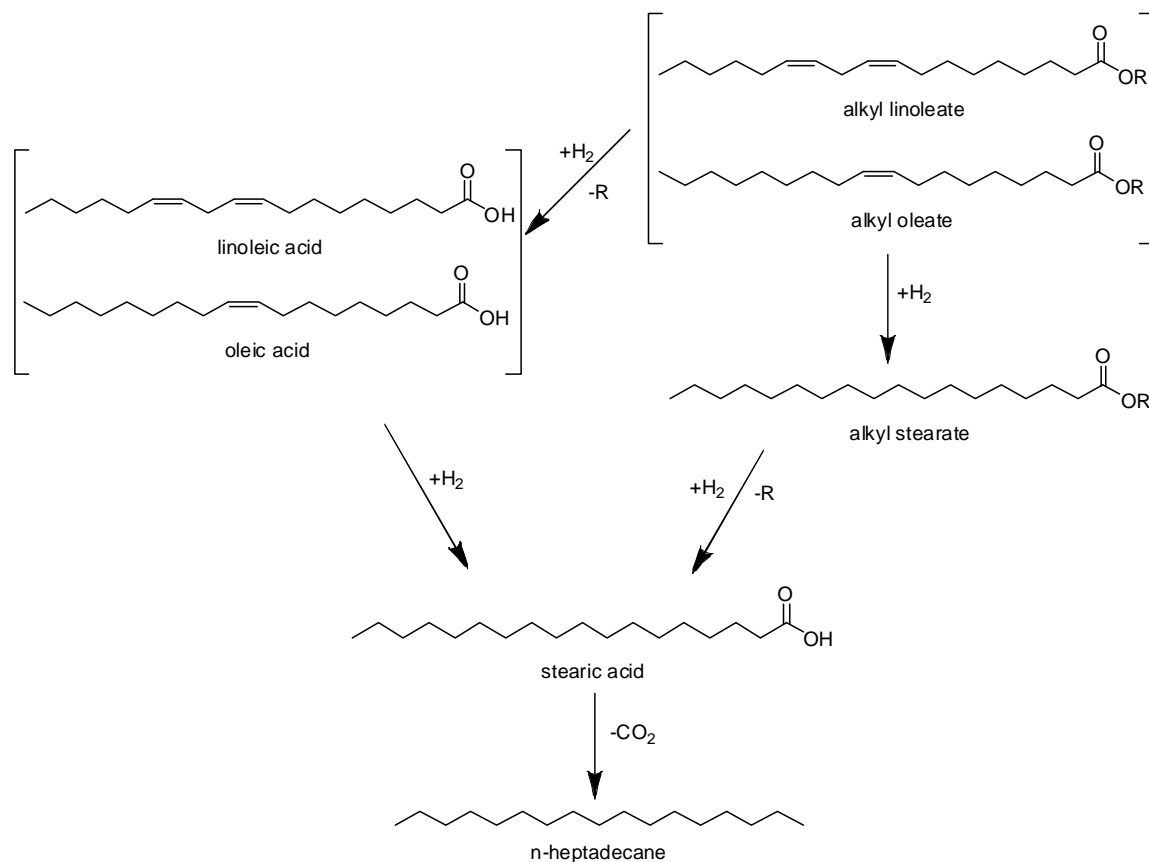
Figure 3.5 – Proposed reaction pathway of fatty acids and their derivatives under hydrogen atmosphere in the presence of Pd-MCF catalysts.

Additionally, reactions were carried out examining the effects of glycerol and propylene glycol in decarboxylation conditions, as the two compounds are commonly found in large quantities in candidate biofeedstocks [17]. At 300 °C in the presence of H_2,

the glycerol is fully reacted after 6 hours, with the main product being the complete dehydration product propane. Approximately 10% selectivity to the incomplete dehydration product propanol was seen, though no evidence of propane diol was observed. Propylene glycol performed similarly, with the major product being propane gas, with a small amount of residual propanol. With two and three moles of water respectively evolved for every mole of propylene glycol and glycerol completely dehydrated, it is necessary to have a purge gas flow during reaction to relieve the reactor of built up overpressure. (Effects of increasing reactor overpressure are discussed in Chapter 4.)

Table 3.5 – Glycerol and propylene glycol in dodecane, H_2, Pd-MCF, 6 h, 300 °C.

| | | Selectivity (%) | | | |
	Conversion	propane	propanol	propane diol	crack[a]
glycerol	100%	90	10	0	< 1
propylene glycol	100%	96	4	-	< 1

[a] potential cracking products: CH_4, C_2H_6, C_2H_4

Finally, the decarboxylation of a mixture of multiple fatty acids and glycerol was investigated. Two different batches are highlighted here: first, a mixture of glycerol, stearic acid and palmitic acid, reacted for 6 hours with Pd-MCF under hydrogen flow at 300 °C in dodecane (Figure 3.6). The glycerol is fully reacted, mainly to propane with some propanol remaining. The conversion of stearic acid is 83%, with the sole product being *n*-heptadecane, and the conversion of palmitic acid is 81%, with full selectivity to *n*-pentadecane. Secondly, a mixture of glycerol with the mono-unsaturated acids linoleic acid and palmitoleic acid were reacted under the same conditions described above, and

the 6-hour reaction results are shown in Figure 3.7. Here we see complete conversion of

the entire reactant mixture, with a similar product breakdown for glycerol, and the acids

being hydrogenated to their fully saturated analogues. The C16 and C18 acids form their

decarboxylated products with 80% and 78% selectivity, respectively.
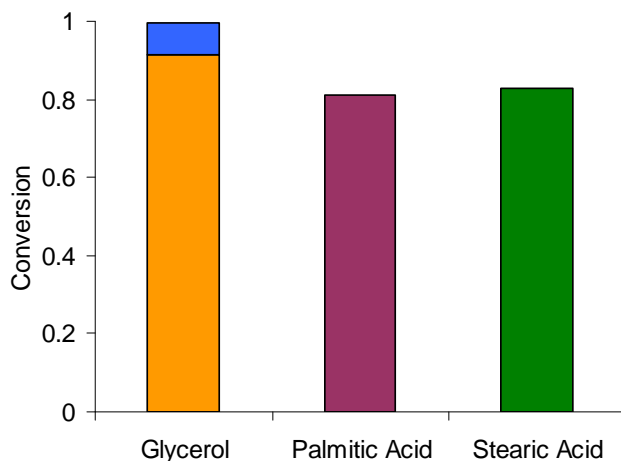
Figure 3.6 – Conversion of a mixture of glycerol and saturated acids, with selectivities of propane (orange), propanol (blue), pentadecane (purple) and heptadecane (green)
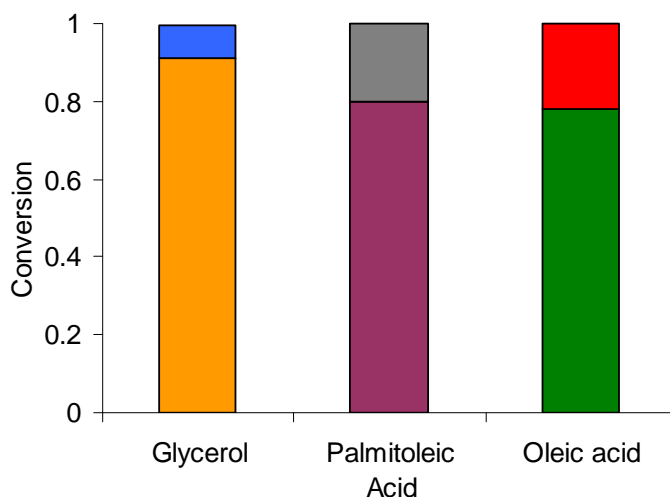
Figure 3.7 – Conversion of a mixture of glycerol and unsaturated acids, with selectivities of propane (orange), propanol (blue), pentadecane (purple), palmitic acid (grey), heptadecane (green), and stearic acid (red)

3.4 Conclusions

The Pd-MCF catalysts exhibited high activity in the decarboxylation of fatty acid model compounds. The kinetics of stearic acid decarboxylation follows a nice smooth curve and yields rates similar to those reported in the literature for palladium supported on carbon [18]. The sole reaction product when decarboxylating pure stearic acid is *n*-heptadecane, a candidate chemical for drop-in diesel fuel, with negligible side product formation. Similarly, palmitic acid decarboxylation follows a similar kinetic curve, with the main product being *n*-pentadecane. The Pd-MCF-U and Pd-MCF-N catalysts exhibited much higher activity than the thiol-functionalized or bare materials, in agreement with the hydrogen uptake chemisorption characterization discussed in Chapter 2.

The Pd-MCF-U catalyst was chosen for further study to investigate the decarboxylation of unsaturated acids, alkyl esters of fatty acids, and glycerol and glycol additives. In the absence of hydrogen, unsaturated acids do not decarboxylate, but instead dimerize and oligomerize, eliminating any further reaction. In the presence of hydrogen, however, the unsaturated acids quickly hydrogenate to their fully saturated analogues, which then decarboxylate as normal. A similar stepwise reaction occurs with fatty acid alkyl esters, during which the dealkylation occurs prior to decarboxylation. A generalized reaction scheme was presented to illustrate the stepwise manner of this progression. Glycerol was found to dehydrate quite readily over the Pd-MCF catalyst in the presence of hydrogen at 300 °C, forming mainly propane with some residual propanol. A similar trend was seen for propylene glycol. No unexpected effects were observed when mixtures of glycerol and saturated and unsaturated acids were tested, with each

component behaving similarly to its individual reaction. Pd-MCF performed well throughout the model compound reactions, making a strong case for being a robust decarboxylation catalyst, at least in single-use applications for now.

3.5 REFERENCES

[1]   F. Aranda, S. Gomez-Alonso, R.M.R. del Alamo, M.D. Salvador, G. Fregapane, Food Chem. 86 (2004) 485-492.

[2]   M. Canakci, J. Van Gerpen, Transactions of the Asae. 42 (1999) 1203-1210.

[3]   E. Crabbe, C. Nolasco-Hipolito, G. Kobayashi, K. Sonomoto, A. Ishizaki, Process Biochem. (Amsterdam, Neth.). 37 (2001) 65-71.

[4]   J.J. Engel, J.W. Smith, J.A. Unruh, R.D. Goodband, P.R. O'Quinn, M.D. Tokach, J.L. Nelssen, J. Anim. Sci. 79 (2001) 1491-1501.

[5]   M.S. Graboski, R.L. McCormick, Progr. Energy Combust. Sci. 24 (1998) 125-164.

[6]   E. Lotero, Y. Liu, D.E. Lopez, K. Suwannakarn, D.A. Bruce, J.G. Goodwin Jr, Industrial and Engineering Chemistry Research. 44 (2005) 5353-5363.

[7]   M.A. Paleari, V.M. Moretti, C. Bersani, G. Beretta, T. Mentasti, Meat Science. 67 (2004) 549-557.

[8]   D.N. Zheng, M.A. Hanna, Bioresour. Technol. 57 (1996) 137-142.

[9]   E.W. Ping, R. Wallace, J. Pierson, T.F. Fuller, C.W. Jones, Microporous Mesoporous Mater. 132 (2010) 174-180.

[10]   M. Snare, I. Kubickova, P. Maki-Arvela, K. Eranen, J. Warna, D.Y. Murzin, Chem. Eng. J. (Lausanne). 134 (2007) 29-34.

[11]   P. Maki-Arvela, I. Kubickova, M. Snare, K. Eranen, D.Y. Murzin, Energy & Fuels. 21 (2007) 30-41.

[12]   M. Snare, I. Kubickova, P. Maki-Arvela, D. Chichova, K. Eranen, D.Y. Murzin, Fuel. 87 (2008) 933-945.

[13]   I. Kubickova, M. Snare, K. Eranen, P. Maki-Arvela, D.Y. Murzin, Catal. Today. 106 (2005) 197-200.

[14]   P. Breteau, Comptes Rendus Hebdomadaires Des Seances De L Academie Des Sciences. 151 (1910) 1368-1369.

[15]   K. Mallick, K. Mondal, M. Witcomb, M. Scurrell, J. Mater. Sci. 43 (2008) 6289-6295.

[16]   P. Maki-Arvela, J. Kuusisto, E.M. Sevilla, I. Simakova, J.P. Mikkola, J. Myllyoja, T. Salmi, D.Y. Murzin, Applied Catalysis a-General. 345 (2008) 201-212.

[17]   D. Fabbri, V. Bevoni, M. Notari, F. Rivetti, Fuel. 86 (2007) 690-697.

[18]   I. Simakova, O. Simakova, P. Maki-Arvela, D.Y. Murzin, Catalysis Today. 150 (2010) 28-31.

CHAPTER 4

DEACTIVATION, REGENERATION & RECYCLE

4.1 Introduction

In 2005 the Murzin group first reported catalysts capable of deoxygenating long-chain acids and derivatives without the use of high hydrogen pressures or without hydrogen altogether [1-11]. Their research demonstrated that a palladium on carbon catalyst can deoxygenate free fatty acids via decarboxylation in the absence of hydrogen overpressures to form the resultant alkane. Further research on this decarboxylation reaction has been carried out with continuing work from the Murzin group [2-4, 12, 13] and others [14-16], examining the effects of differing reaction atmospheres, temperatures, degrees of acid unsaturation, catalyst supports, and reactor types, with a wide variety of results. One observation that remains constant across the studies, however, is that the supported palladium catalysts readily deactivate during the decarboxylation reaction [2, 3, 9, 13, 14, 16], having a detrimental effect on catalyst turnover and recycle. The trend in the literature is to recognize a decrease in catalyst surface area and pore volume, and therefore identify the most likely catalyst deactivation mechanism as coking. Although this may be a reasonable suggestion, additional evidence to support this and rule out other deactivation methods has not yet been reported.

The approach in our initial study of fatty acid decarboxylation [14] was to develop a well-defined supported palladium catalyst that could be fully characterized both before and after deactivation. A mesocellular foam (MCF) silica support was

chosen to allow post-mortem carbon-based characterization techniques that would not involve significant background subtraction or interference associated with use of the commonly studied activated carbon supports. Similarly, thermal oxidative treatments such as calcination could be applied to investigate the nature of the deactivation without the potential to alter the physical properties of the support itself, as may be the case with carbon-based supports. This silica support was also designed to have very large pores to allow not only for better internal mass transfer of reactants and products during reaction, but to provide a substrate on which the nature of the reported deposition could be more easily elucidated. Finally the catalyst was synthesized in such a way to deposit a very narrow size distribution of palladium nanoparticles uniformly throughout the silica particle, yielding a well-defined catalyst on which a battery of material properties could be compared before and after reaction. Furthermore, with a small average nanoparticle size (~2 nm), various characterization techniques could be used to track not only changes in nanoparticle particle size and morphology, but the high metal dispersion would facilitate spectroscopic confirmation of alterations in nanoparticle surface oxidation or chemical poisoning. Herein we apply this catalyst (Figure 4.1) to the standard literature decarboxylation reaction of stearic acid to *n*-heptadecane with the aim of (i) elucidating the nature of the deactivation and (ii) developing a procedure to regenerate the catalytic activity.
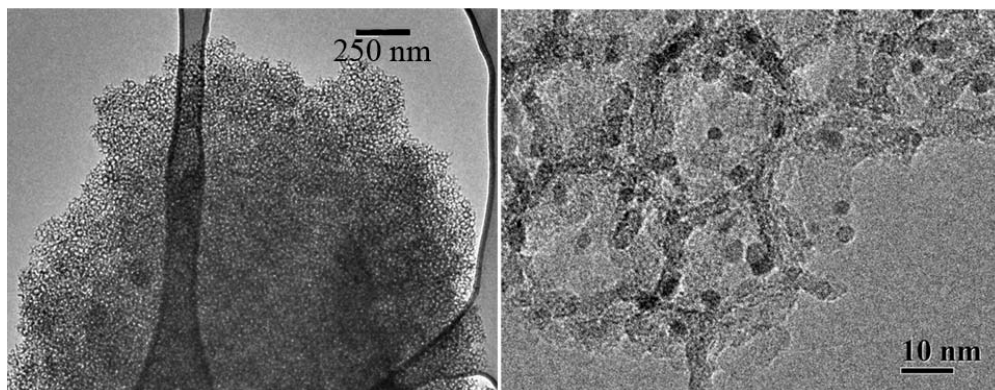
Figure 4.1 – TEM images of Pd-MCF catalyst used for this study.

4.2 Materials and Characterization Methods

4.2.1 Chemicals

The following chemicals were commercially available and used as received: dodecane (anhydrous, Sigma-Aldrich), N,O-bis(trimethylsilyl)acetamide (BSA, 95%, Sigma-Aldrich), pyridine (ACS grade >99%, Sigma-Aldrich), dichloromethane (DCM, ACS grade, EMD chemicals), stearic acid (>97%, Fluka), tetrahydrofuran (THF, ACS grade, EMD chemicals), hexane (anhydrous, Sigma-Aldrich), diethyl ether (anhydrous, Sigma-Aldrich), and potassium bromide (KBr, 99%, Alfa Aesar). Tridecane was purchased from Sigma-Aldrich, distilled over CaH_2, and stored in a nitrogen glove box.

4.2.2 Material Synthesis

The Pd-MCF catalyst was synthesized as discussed previously in Chapter 2. In this work, only the urea-functionalized precatalyst was utilized prior to metallation, mild calcination, and reduction under hydrogen flow (Pd-MCF-U, hereafter referred to only as Pd-MCF). All samples were dried under vacuum and stored in a nitrogen glove box prior to further use in reaction or various characterization techniques.

66

4.2.3. Material Characterization

Nitrogen adsorption isotherms were measured at 77K on a Micromeritics ASAP 2010. Surface area was determined by the Brunauer-Emmett-Teller method, in general using relative pressures less than 0.15. The Broekhoff-de Boer method with the Frenkel-Halsey-Hill (BdB-FHH) modification [17] (See Appendix A), was used to calculate pore size distributions for both the large cells (adsorption upswing, assuming spherical capillary condensation) and the interconnecting windows (desorption downswing, assuming cylindrical capillary evaporation).

A Netzsch STA409 was used for thermogravimetric analysis (TGA) under an air flow diluted by nitrogen. Samples were heated under flow at 10 °C/min from 30 to 900 °C, with the total organic content estimated from the weight loss between 150 and 800 °C. Onboard differential scanning calorimetry (DSC) was used to identify peak temperatures of combustion exotherms.

Total active metal surface area was determined by H_2-O_2-H_2 titration chemisorption measurements in a Micromeritics AutoChem II 2920. To ensure full metal reduction, samples were reduced in 5% H_2 flow at 300 °C prior to analysis with sequential titrations of H_2 and O_2. H_2 uptake at room temperature was monitored by a thermal conductivity detector (TCD), and as in previous studies [14], background uptake titrations on the bare support confirm negligible uptake from the catalyst substrate.

Catalyst dissolution was performed by stirring 250 mg catalyst in 100 mL aqueous strong base (1 g KOH / g H_2O), resulting in free palladium nanoparticles, soluble silica salts, and any residual organics. The organic fraction was separated via extractions with diethyl ether and characterized with ^{1}H NMR and GC-MS. Solution phase [1]H

nuclear magnetic resonance (NMR) measurements were performed using a Mercury Vx 400 MHz with $CDCl_3$ as solvent. Solid state ^{13}C NMR spectra were measured using cross polarization magic-angle spinning (CP-MAS) measurements on a Bruker DSX 300 spectrometer at frequencies of 75.5MHz. The sample was packed into a 7 mm rotor and spun at 5 kHz, and a single pulse of $\pi/2$ and repetition time of 4 s was used. The spectrum was recorded after 14000 scans. The chemical shifts of ^{13}C were referenced to adamantane.

Infrared spectra were acquired using KBr pellets with a Bruker Vertex 80v with dual FT-IR and FT-Raman benches and Ram-II module. Powder X-ray diffraction (XRD) patterns were obtained on a Philips Analytical X'Pert diffractometer, Cu-Kα radiation, equipped with an X'celerator detector and nickel filter. The scattered intensities were collected from 0.5° to 90° (2θ) by scanning at 0.008° (2θ) steps.

X-ray photoelectron spectroscopy (XPS) was performed on a powder sample grid with a Thermo Scientific K-Alpha XPS at room temperature and 10^{-8} mbar vacuum. For palladium 3d scans, a 200 μm incident spot size was measured with 0.1 eV step size between 329 and 347 eV and constant analyzer pass energy of 50 eV, using the carbon 1s binding energy of 284.8 eV as reference.

Extended X-ray absorption fine structure (EXAFS) spectra were acquired at the Argonne National Lab, using the synchrotron radiation at the Advanced Photon Source, Beamline 10-ID. Absorbance spectra were measured from 24.2 – 25.2 keV around the palladium k-edge (24.351 keV). Phase shift and backscattering amplitudes were obtained from Pd foil. The EXAFS coordination parameters were obtained by a least square fit r-

space of k^2–weighted Fourier transform data using standard procedures and WINXAS 3.1 software. The quality of the fits were equally good with both k^1 and k^3 weightings.

Quantitative analyses of reaction kinetics and conversions were performed on a Shimadzu GC-2010 gas chromatograph with flame ionization detector (GC-FID) equipped with an SHRX5 column (15m, 0.25μm film thickness, 0.25mm i.d.). Verification of organic products and extracts was performed on a Shimadzu GCMS-QP2010S gas chromatograph with mass spectrometer detector (GC-MS) equipped with an SHR5XLB column (30m, 0.25μm film thickness, 0.25mm i.d.).

Scanning electron microscopy (SEM) was performed on sonicated and gold-sputtered samples using an Hitachi S-800 operating at 10 kV. Catalyst samples were also dispersed in ethanol and deposited on polymer/copper grids for analysis via transmission electron microscopy (TEM) on both a JEOL 100CX II (100kV) and an Hitachi HF-2000 field emission gun (FEG) (200kV). Quantitative elemental analyses were performed by inductively coupled plasma optical emission spectrometry (ICP-OES) by Columbia Analytical Services, Tuscon AZ.

4.2.4 Decarboxylation Procedure

Similar to the procedure outlined in Chapter 3, batch decarboxylation of stearic acid was carried out in a 300 °C oil bath [14]. In general, 15 mL glass pressure tubes were charged with 25 mg Pd-MCF, 2.7 mL of 0.15 M stearic acid in dodecane, and 50 μL tridecane as internal standard. Residual acidic protons in samples taken for kinetic analysis were derivatized with trimethylsilyl groups via reaction with BSA in pyridine prior to injection into the GC-FID. Spent catalyst was extracted from the reaction vessels

with 25 mL THF, filtered through a 0.5 μm filter, washed with two subsequent aliquots THF, and dried under vacuum at 100 °C overnight. Prior to reuse, the spent catalyst was re-reduced under H_2 flow at 300 °C for 2 hours.

4.3 Results and Discussion

4.3.1 Attempted Recycle and Spent Catalyst Characterization

The kinetics of the decarboxylation of stearic acid to *n*-heptadecane are shown in Figure 4.2 for the fresh Pd-MCF catalyst and the catalyst reused after one 6-hour reaction. The catalyst activity is nearly completely lost after one use, with the used catalyst unable to achieve more than 4% conversion after six hours. H_2-O_2 chemisorption titrations quantifying hydrogen uptake as a measure of available active metal surface area were carried out on both the fresh and spent catalyst (Table 4.1). A greater than 20-fold decrease in active palladium surface area was measured for the spent catalyst, from 12.7 m^2/g to 0.6 m^2/g, consistent with the large decrease in stearic acid reactivity. The nature of this loss of palladium active sites is discussed below.
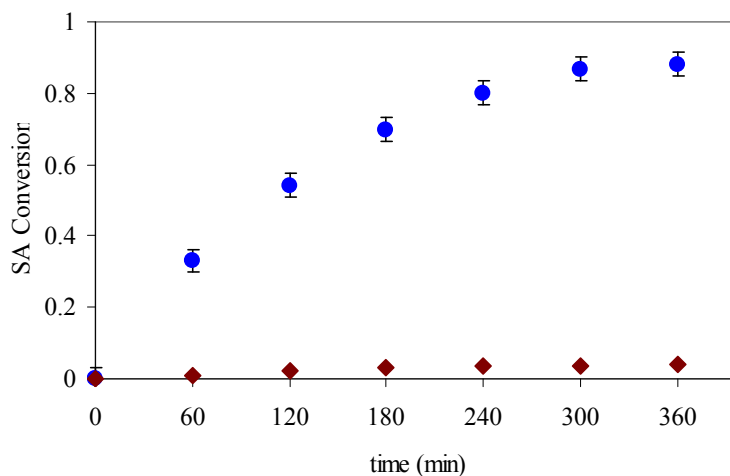
Figure 4.2 – Decarboxylation kinetics of 0.15 M stearic acid for (•) fresh Pd-MCF (♦) spent Pd-MCF

Table 4.1 – Characterization data for Pd-MCF catalysts

	SA_{BET} (m^2/g_{SiO2})	V_{pore} (cc/g_{SiO2})	d_{cell}^{a} (nm)	d_{window}^{a} (nm)	organic[b] wt %	Pd[c] wt %	d_{Pd}^{d} (nm)	SA_{Pd}^{e} (m^2/g_{SiO2})
MCF	710	2.9	37	17	-	-	-	-
Pd-MCF	670	2.5	36	16	-	5.5	2	12.7
spent Pd-MCF	515	1.7	34	16	16	5.5	2	0.6
Pd-MCF-350	550	2.0	34	16	10	5.3	5	2.1
Pd-MCF-600	650	2.4	35	16	0.3	5.6	9	3.0
Pd-MCF-regen	660	2.4	35	16	1.5	5.4	2	12.2

[a] BdB-FHH, [b] TGA, [c] EA, [d] EXAFS/TEM, [e] H_2-O_2 chemisorption

Characterization of the fresh and spent catalyst via XPS was performed to determine whether the catalyst deactivation could be attributed to changes in the oxidation state of the palladium metal (Figure 4.3). The palladium $3d_{5/2}$ and $3d_{3/2}$ spectra show characteristic zero-valent binding energies (335.3 eV and 340.4 eV, respectively) with negligible shift between fresh and spent catalysts. Additionally, the EXAFS spectra of the fresh and spent catalyst, shown in Figure 4.4, both exhibit the same Pd-Pd metallic bond character with no discernible appearance of a Pd-O scattering path in the spent catalyst. The consistent nature of the results from these two techniques allows us to reasonably disregard bulk or surface oxidation as likely deactivation candidates.
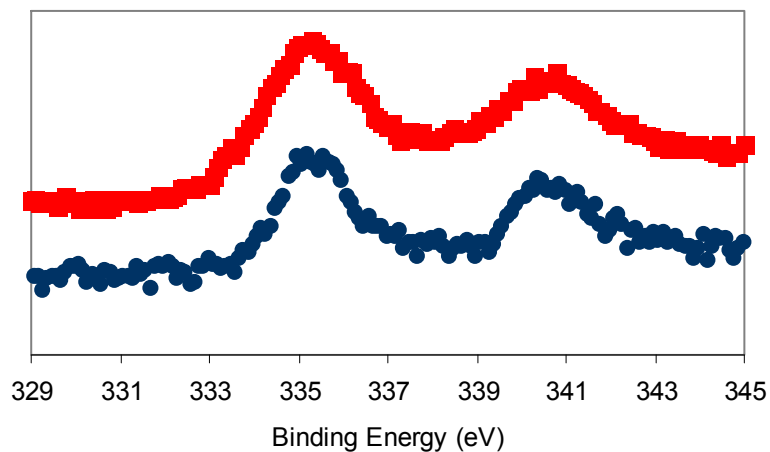
Figure 4.3 – XPS spectra of (top) fresh Pd-MCF and (bottom) spent Pd-MCF
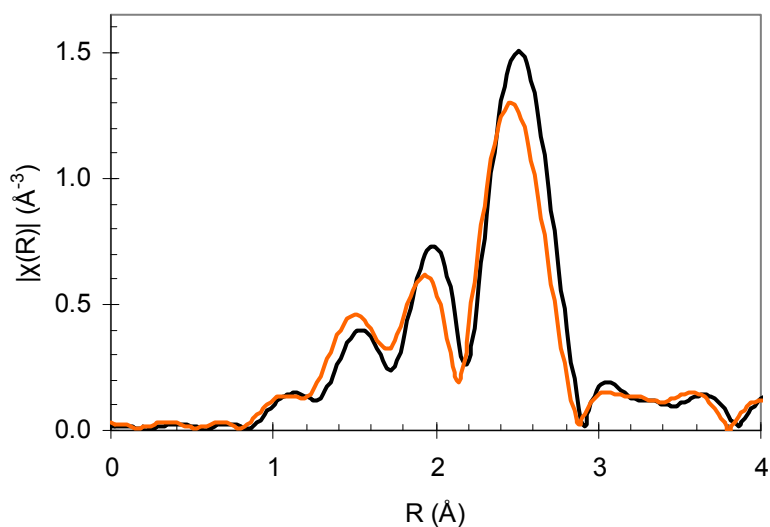
Figure 4.4 – FT-EXAFS spectra of (black) fresh Pd-MCF and (orange) spent Pd-MCF

Another useful observation drawn from comparing the fresh and spent EXAFS spectra is that there is negligible palladium particle size growth over the course of reaction. Although unlikely to cause the severe deactivation depicted in Figure 4.2, palladium nanoparticle sintering, agglomeration, and ripening are still common

nanoparticle phenomena that can be discarded as significant deactivation sources in this system. In fact, the slight peak shift exhibited by the spent catalyst in Figure 4.4 suggests a small decrease in average nanoparticle size as compared to the fresh sample. This change is, however, attributed to a lattice contraction due to a loss of the interstitial hydride formed during the pretreatment reduction in flowing H_2, rather than a palladium loss mechanism (as confirmed by quantitative palladium elemental analysis, Table 4.1).
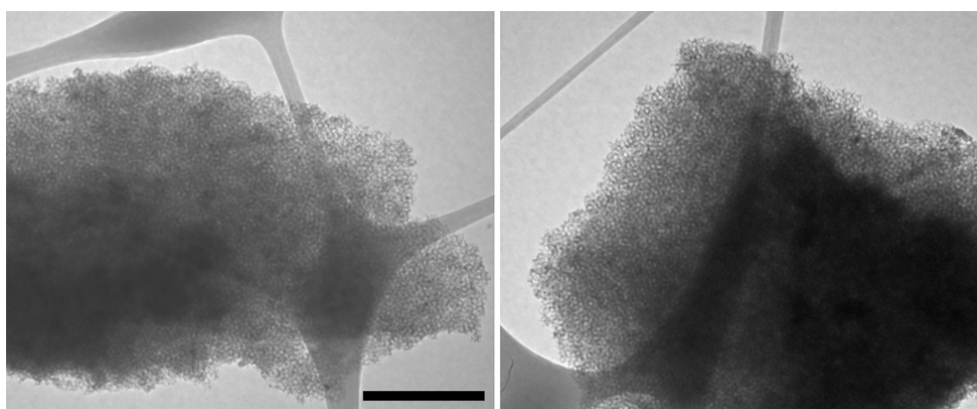
Figure 4.5 –TEM images showing broad foam-like structure of (a) fresh Pd-MCF and (b) spent Pd-MCF [black bar = 500 nm]

Surface area and porosity data from N_2 physisorption for the fresh and spent catalysts provide some further insight into the difference in material properties between the samples (Table 4.1); the catalyst clearly loses substantial surface area and pore volume after reaction. On the other hand, observations from microscopy suggest that the MCF support remains intact, maintaining its mesoporous foam-like structure after reaction (Figure 4.5), and thusly support collapse cannot reasonably be blamed for the porosity loss. Instead, substantial organic deposition was confirmed via TGA, with a measured total organic fraction of approximately 16% by weight (Table 4.1). It is

hereafter hypothesized that this organic deposition plays the primary role in the catalyst deactivation; therefore its efficient removal becomes paramount.

One of the benefits of utilizing a silica-supported catalyst is that any carbonaceous deposits can be removed via calcination. Discussed here are results from 3-hour calcinations in flowing air at 350 °C and 600 °C, temperatures chosen from TGA data as an intermediate oxidation temperature and a temperature at which the major organic components are readily removed, respectively. After 350 °C calcination, during which approximately 40% of the deposited organics are removed, surface area, pore volume and hydrogen uptake all increase as compared to the spent catalyst, but fail to rebound to their original values (Table 4.1). After calcination at 600 °C, over 98% of the deposited organics are removed, and the material exhibits nearly-complete recovery of surface area and pore volume. However, the catalyst is unable to adsorb as much hydrogen as the original catalyst, and the explanation for this is illustrated in the EXAFS spectra shown in Figure 4.6. Metallic Pd has two peaks between about 2-3 Å for a single Pd-Pd distance. The magnitude of the Fourier transform is proportional to the Pd-Pd coordination number, or average nanoparticle radius. The increasing amplitude of the metallic Pd-Pd scattering path as calcination temperature is increased is indicative of an increase in nanoparticle size. So while high temperature calcination can successfully remove the majority of the organic deposition from the spent catalyst, as expected, the palladium nanoparticles significantly agglomerate at these temperatures. Quantitatively, the calcination program that was effective at removing more than 98% of the organics decreased the accessible palladium available for reaction by more than 75%. Ideally, another methodology would

be developed to remove the organics without significantly affecting the morphology and distribution of the palladium nanoparticles.
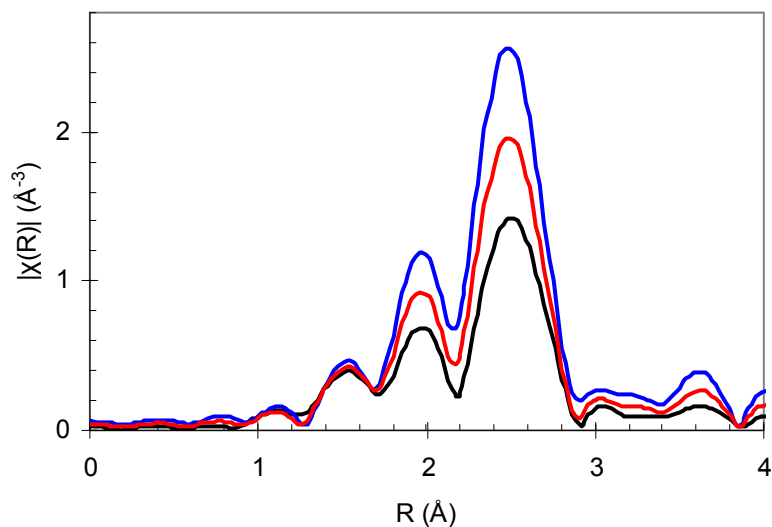
Figure 4.6 – FT-EXAFS of (black) fresh Pd-MCF, (red) spent Pd-MCF calcined at 350 ºC, and (blue) spent Pd-MCF calcined at 600 ºC

The first step in developing this new methodology was to identify the carbonaceous species deposited on the catalyst, and here an array of characterization techniques was applied. ^{13}C CP-MAS NMR spectra of the spent catalyst were initially measured (Figure 4.7) as an attempt to elucidate the functionality of the organic molecules present on the material. Whereas the presence of aliphatic carbon could be confirmed, the relatively low organic loading, in combination with the inherent line-broadening associated with solid-state NMR, made it difficult to identify other moieties, and definitive speciation was not possible. Upon examination of the FT-IR spectrum of the spent catalyst (Figure 4.8), the C=O stretch indicative of an alkyl carboxylic acid group was clearly visible around 1700 cm^{-1}. Additionally, the obvious presence of

multiple sp^3 C-H stretches in the 2850 – 2950 cm^{-1} range was consistent with the NMR spectrum.
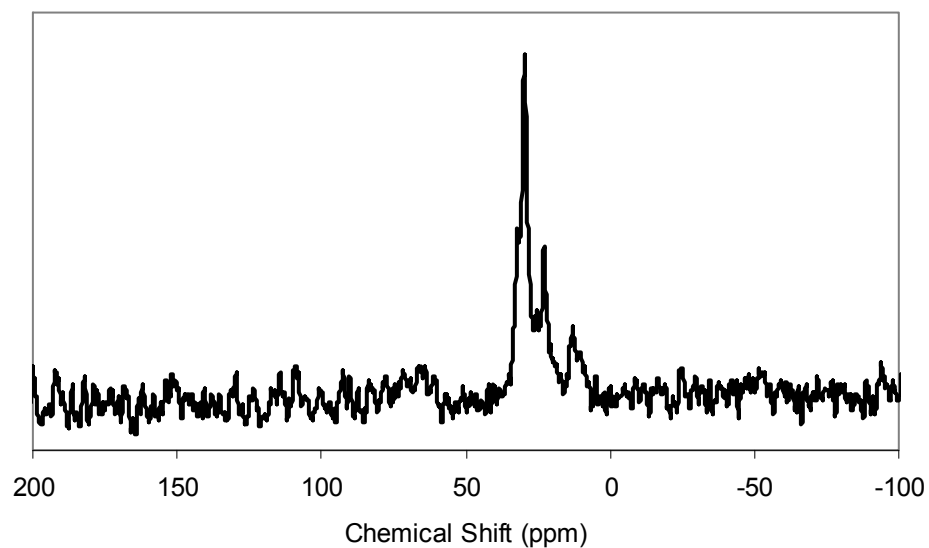
Figure 4.7 – ^{13}C CP-MAS NMR of spent Pd-MCF
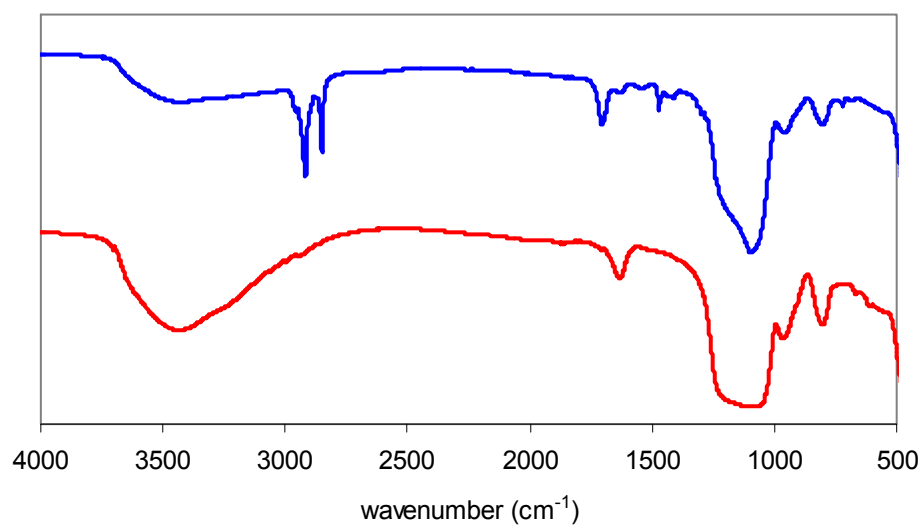
Figure 4.8 – FT-IR spectra of (top) spent Pd-MCF and (bottom) Pd-MCF-regen

For a more direct speciation of the deposited molecules, the spent catalyst was dissolved in an aqueous strong base solution, yielding soluble silica salts, free palladium nanoparticles and the residual organics. After phase-extracting the organic components, solution ^{1}H NMR and GC-MS were used to identify the residual compounds. Three main organic components were definitively identified: dodecane (n-C$_{12}$), heptadecane (n-C$_{17}$), and stearic acid (n-C$_{17}$-COOH) – or, in the context of the investigated reaction, solvent, product, and reactant, respectively. Imposing the assumption that a mixture of these three compounds accounts for the organic deposition on the spent catalyst is consistent with the aforementioned characterization results.

4.3.2 Regeneration and Recycle

Now operating under the hypothesis that reactants and products, and not large deposits of coke, are potentially responsible for the catalyst deactivation, systematic solvent washes were applied to remove the residual reaction products and reactants. Sequential agitated 12-hour washes at 80 °C with THF, hexane, and DCM yielded the highest organic removal (via TGA); after drying and reduction, the material is denoted Pd-MCF-regen (Table 4.1). As can be seen in the tabulated data, the regenerated catalyst regains nearly all of the lost surface area, porosity, and active metal surface area after the removal of 90% of the organic deposition. FT-IR spectroscopy of the regenerated catalyst (Figure 4.8) shows almost complete disappearance of the peaks corresponding to the deposited organics (sp^3 carbon C-H at 2850-2950 cm^{-1}, alkyl carboxylic acid C=O at 1700 cm^{-1}). While no evidence of dimeric or oligomeric compounds has been observed in the use of fully saturated reactant acids in this study, we cannot definitively rule out

the possibility of their existence in trace quantities. However, previous reports have only

seen oligomerization in the decarboxylation of unsaturated acids [5, 10].
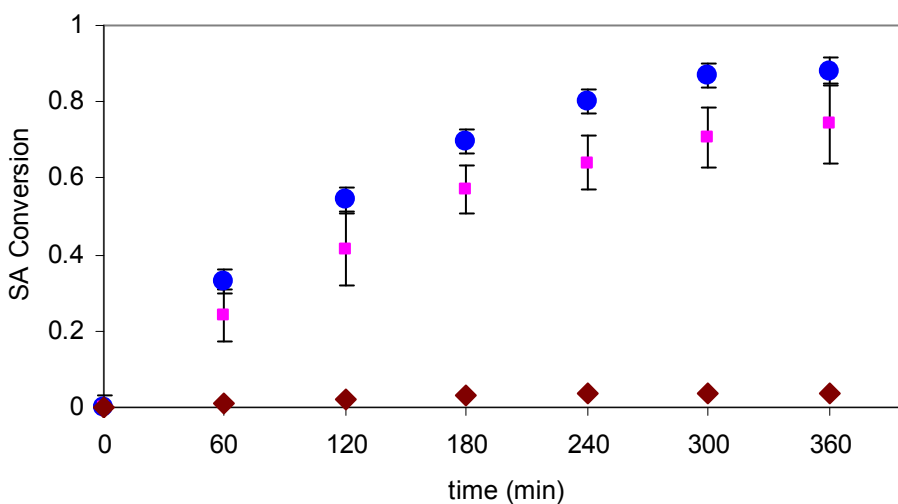
Figure 4.9 – Decarboxylation kinetics of 0.15 M stearic acid for (•) fresh Pd-MCF (♦) spent Pd-MCF (▪) Pd-MCF-regen (error bars represent standard deviation of replicates).

Reaction kinetics are shown in Figure 4.9 for the fresh, spent, and regenerated

catalyst. The 6-hour conversion of stearic acid to n-heptadecane using the regenerated

catalyst is a nearly 20-fold improvement over the recycled spent catalyst. We further

hypothesize that the deactivation can be attributed to high palladium surface coverage of

reactant acid, in non-reactive binding configurations, in a manner similar to common

nanoparticle-surfactant layer interactions. Coverage dependent decarboxylation activity

of palladium has been elucidated recently by Immer and Lamb [18], and fits with

concentration-dependent phenomena we have seen. Figure 4.10 illustrates the effect of

initial stearic acid concentration on total moles of stearic acid reacted in batch after 6

hours at 300 °C in an inert atmosphere. Total moles reacted are calculated by multiplying

the reaction volume, 6 hour conversion, and initial concentration together, and is expected to increase with increasing initial concentration. It is important to note that this is not necessarily a kinetic determination—the linear trend in the sub 0.20 M region is not insinuating a zero-order reaction, but instead represents approximately 90% conversion (the commonly seen equilibrium conversion for this reaction in batch). That is to say, the reaction reaches equilibrated completion by the time the sample is taken at 6 hours.
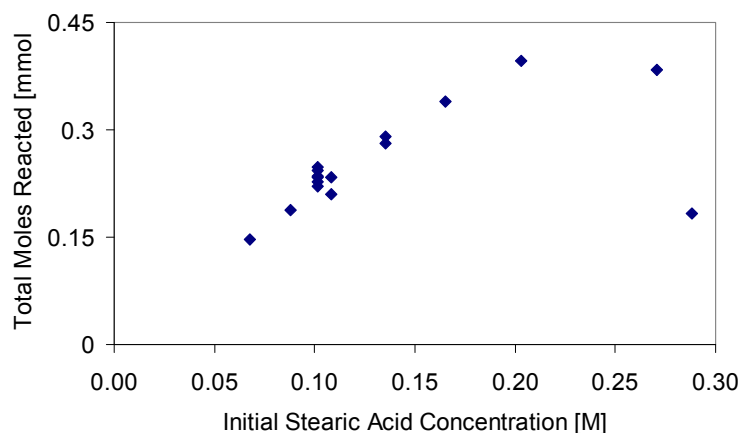
Figure 4.10 – Total moles stearic acid reacted after 6 hours vs. initial stearic acid concentration for the same catalyst loading and reactor volume.

However this increasing trend drops off sharply after 0.20 M, and the reaction that began with 0.29 M stearic acid produces only as much heptadecane as that which began at 0.09 M. This coverage-dependent trend has been tracked dynamically by Immer and Lamb, and shown to be affected not only by acid concentration, but high overpressures of co-adsorbing gases, like H_2 or CO. Additionally, the dominant reaction mode changes with high surface coverage, switching from decarboxylation-dominant to decarbonylation-dominant [18]. This leads to runaway catalyst poisoning, as decarbonylation evolves CO (as opposed to CO_2 from decarboxylation) which is readily adsorbed by available

palladium surface sites. This runaway poisoning can only be reversed by purging the reactor with a nominal hydrogen stream which will readily displace the surface CO adsorbate at the reaction temperature and allow the CO to be purged from the vessel. It is perhaps serendipitous then that Murzin et al began their decarboxylation work in 2005 under semi-batch conditions with a 5% H_2 gas flow [11]. And it is for this reason that subsequent reactions in this thesis utilizing real feedstocks are operated in Parr reactor with a H_2 bleed.

4.4 Conclusions

The deactivation of a supported palladium nanoparticle catalyst during fatty acid decarboxylation has been investigated, and the nature of the cause of the deactivation has been conclusively elucidated for the first time. A well-defined silica-supported catalyst Pd-MCF, previously developed for our initial study [14], was fully characterized before and after use in the 300 °C batch decarboxylation of stearic acid under inert atmosphere. After one use, the catalyst activity was reduced dramatically, achieving less than 5% conversion to n-heptadecane in the second use. XPS of the spent catalyst showed no change in the oxidation state of the palladium nanoparticles, while TEM and EXAFS verified negligible changes in their size or morphology, ruling out sintering or agglomeration as a key cause of deactivation. The spent catalyst surface area and pore volume decreased significantly, attributed to a 16 % by weight deposition of organics rather than a structural or morphological change in the silica substrate. Contrary to previous assumptions, the majority of this carbonaceous deposition was found not to be traditional coke, but instead residual reactants, solvent and product (by NMR, FT-IR, and

GC-MS). These findings fit well with newly-published evidence of surface-coverage deactivation mediated by initial reactant concentration and adsorbed gaseous reaction byproducts [18]. Attempts to remove the organic species from the spent catalyst via calcinations resulted in significant palladium nanoparticle growth, with the average particle size increasing to over 9 nm after treatment in air at 600 °C. Sequential hot extractions with solvents THF, hexane and DCM decreased the organic content of the spent catalyst by 90%, and FT-IR confirmed the removal of residual acids and alkanes. After reduction in H_2 at 300 °C, the regenerated catalyst showed a 19-fold increase in decarboxylation activity compared to the original spent catalyst.

4.5 REFERENCES

[1]   M. Snare, P. Maki-Arvela, I.L. Simakova, J. Myllyoja, D.Y. Murzin, Russian Journal of Physical Chemistry B. 3 (2009) 1035-1043.

[2]   I. Simakova, O. Simakova, P. Maki-Arvela, A. Simakov, M. Estrada, D.Y. Murzin, Applied Catalysis a-General. 355 (2009) 100-108.

[3]   S. Lestari, P. Maki-Arvela, I. Simakova, J. Beltramini, G.Q.M. Lu, D.Y. Murzin, Catalysis Letters. 130 (2009) 48-51.

[4]   S. Lestari, P. Maki-Arvela, H. Bernas, O. Simakova, R. Sjoholm, J. Beltramini, G.Q.M. Lu, J. Myllyoja, I. Simakova, D.Y. Murzin, Energy & Fuels. 23 (2009) 3842-3845.

[5]   M. Snare, I. Kubickova, P. Maki-Arvela, D. Chichova, K. Eranen, D.Y. Murzin, Fuel. 87 (2008) 933-945.

[6]   P. Maki-Arvela, M. Snare, K. Eranen, J. Myllyoja, D.Y. Murzin, Fuel. 87 (2008) 3543-3549.

[7]   S. Lestari, I. Simakova, A. Tokarev, P. Maki-Arvela, K. Eranen, D.Y. Murzin, Catalysis Letters. 122 (2008) 247-251.

[8]   M. Snare, I. Kubickova, P. Maki-Arvela, K. Eranen, J. Warna, D.Y. Murzin, Chemical Engineering Journal. 134 (2007) 29-34.

[9]   P. Maki-Arvela, I. Kubickova, M. Snare, K. Eranen, D.Y. Murzin, Energy & Fuels. 21 (2007) 30-41.

[10]   M. Snare, I. Kubickova, P. Maki-Arvela, K. Eranen, D.Y. Murzin, Industrial & Engineering Chemistry Research. 45 (2006) 5708-5715.

[11]   I. Kubickova, M. Snare, K. Eranen, P. Maki-Arvela, D.Y. Murzin, Catalysis Today. 106 (2005) 197-200.

[12]   I. Simakova, O. Simakova, P. Maki-Arvela, D.Y. Murzin, Catalysis Today. 150 (2010) 28-31.

[13]   H. Bernas, K. Eranen, I. Simakova, A.R. Leino, K. Kordas, J. Myllyoja, P. Maki-Arvela, T. Salmi, D.Y. Murzin, Fuel. 89 (2010) 2033-2039.

[14]   E.W. Ping, R. Wallace, J. Pierson, T.F. Fuller, C.W. Jones, Microporous Mesoporous Mater. 132 (2010) 174-180.

[15]   S. Lestari, P. Maki-Arvela, K. Eranen, J. Beltramini, G.Q.M. Lu, D.Y. Murzin, Catal. Lett. 134 (2010) 250-257.

[16]   J.G. Immer, M.J. Kelly, H.H. Lamb, Applied Catalysis a-General. 375 (2010) 134-139.

[17]   W.W. Lukens, P. Schmidt-Winkel, D.Y. Zhao, J.L. Feng, G.D. Stucky, Langmuir. 15 (1999) 5403-5409.

[18]   J.G. Immer, H.H. Lamb, Energy Fuels. 24 (2010) 5291-5299.

CHAPTER 5

UPGRADING BROWN GREASE FEEDSTOCK

5.1 Introduction

This thesis has previously discussed at length the need for the development of a renewable transportation fuel that is economically viable. With a plethora of analysis debating the current lackluster progress in production of economically-competitive biofuels [1-5], a common admission is the drastic effect of feedstock cost. In independent models, it has been determined that initial materials cost for a given biofeedstock can account for up to 75% of the final biofuel price [5, 6]. For this reason, recent attention has shifted to the utilization of lower cost feedstocks—specifically waste greases, as they can cost over an order of magnitude less than more polished feedstocks [7, 8]. In this study, we were provided with an otherwise-waste grease feedstock from a local poultry rendering facility (American Proteins, Toccoa GA) with the goal of upgrading it to fuel-length hydrocarbons. This chapter will discuss the upgrading process of this brown grease material via catalytic decarboxylation over Pd-MCF catalysts.

5.2 Raw Brown Grease Feedstock

The brown grease in this study was derived from a poultry rendering wastewater separation. Initially, water was separated on-site with a continuous flow Westfalia SA1-01-175 centrifugal separator to less than 1% by weight. Fixed solids content (non-combustible at 550^0C) were lower than expected at less than 1% by weight, indicating

most of the silicate impurities were removed with the aqueous phase. The resultant material is hereafter referred to as raw or unpolished brown grease. This odorous material could be separated into an oily liquid phase and a thick solids phase via centrifugation (4000 rpm, 5 min), with approximately 60% by volume oil, 40% solids. A histogram of carbon chain length composition of unpolished brown grease is shown in Figure 5.1, from which can clearly see the main carbonaceous components of this material are C_{16} and C_{18} compounds.
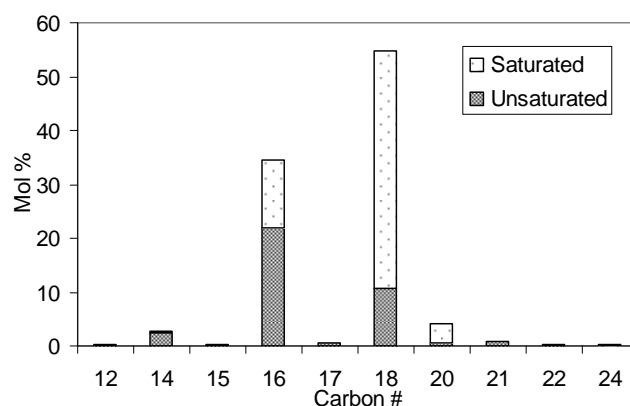
Figure 5.1 – Chain length distribution of carbonaceous compounds in unpolished brown grease.

Similar to the model compound reactions carried out in Chapter 3, decarboxylation of the unpolished brown grease was performed in a 30 mL stainless steel stirred Parr reactor at 300 °C over Pd-MCF catalyst for 6 hours under 10 mL/min hydrogen flow. The resultant product was a dark, incredibly odorous, oily mixture at room temperature, and a large quantity of very solid material had to be scraped and chipped out of the reactor. Cursory characterization of the product mixture showed very

low yields of the C_{16} and C_{18} decarboxylation products *n*-pentadecane and *n*-heptadecane, respectively (Table 5.1), with large quantities of unknown compounds. Indications from GC-MS of nitrogen-, phosphorous-, and sulfur-containing compounds fit with existing knowledge of brown grease-based impurities [7]. The massive impurities in the unpolished brown grease material substantially hindered the degree of decarboxylation, and therefore we turned our attention to pretreatment polishing methodologies to create a cleaner feedstock for decarboxylation.

Table 5.1 – 6 hour decarboxylation results for unpolished brown grease under H_2 at 300 °C.

	C_{16}		C_{18}	
	Conversion	Selectivity[a]	Conversion	Selectivity[b]
Unpolished brown grease	33%	11%	27%	14%

[a] to *n*-C_{15}, [b] to *n*-C_{17}

5.3 Polishing of Brown Grease

The main thrust of the polishing was the extraction of fatty acids from the brown grease matrix. Initially, a number of solvents covering a range of polarities were selected to determine which removed organic acids and at what rate. The solvents ranged from aqueous phosphoric acid to canola oil, but, with the exception of lauric acid, there seemed to be little effect (Table 5.2). What did occur was an initial separation into solid and liquid layers, which was even more pronounced after allowing time for crystallization. Table 5.2 describes mixing different solvents at 15 % by volume with heated (65 °C) brown grease for 30 minutes followed by centrifugation at 4000 rpm for 5

minutes, after which a solid "wax" layer and a liquid "oil" layer form. The data listed are for the extracted oil layer; while some concentration of the acids occurred in the wax layer, this occurrence was inconsistent and generally quite small.

Table 5.2 – Extraction (w/w) of carboxylic acids from brown grease with different solvents

| | Acid extraction (%) | | |
	C_{12}	C_{16}	C_{18}
Phosphoric acid[a]	69.0	0.0	16.4
Water	68.1	21.3	26.6
Methanol	72.6	28.9	48.0
Ethanol	73.1	24.2	39.6
Isopropyl alcohol	69.4	26.5	44.0
Ethyl acetate	0.0	17.8	44.1
Canola oil	72.7	32.0	41.4

[a] 1.73 M

This phase separation capability was also probed for the different solvents, as an oil phase is the preferred over a solid phase for our decarboxylation reactant stream (Table 5.3). After reviewing the literature, it was found that the heating process and chemical addition are commonly referred to as degumming and dewaxing, respectively [9, 10]. A salt addition was found to increase oil yield and speed the recrystallization of the wax components, and calcium chloride was chosen as the primary dewaxing salt as per Rajam, et al. [10]. Figure 5.2 illustrates a subset of experiments investigating the effect of dewaxing conditions on oil phase yield. Calcium chloride was added to the unpolished brown grease in three different quantities, 0.2 g/L, 1 g/L and 2 g/L with the latter two yielding a slightly larger oil phase (67%) than the former (56%). Additionally, the same

quantities of calcium chloride were added along with 2.5 volume percent ethyl acetate, resulting in an increase of oil phase yield to 87%, 89% and 84% respectively. For comparison, 0.75 g/L calcium phosphate was added (molar equivalent of 1 g/L calcium chloride) both directly and with ethyl acetate, but resulted in no remarkable difference in oil phase yield (72%, 76%). Figure 5.3 illustrates the effect of the same treatment conditions on residual acid content. The dewaxing regimen combination of ethyl acetate and calcium chloride followed by centrifugation resulted in the highest oil phase yield and the best acid extraction. This material, a neutral-smelling oil, was designated Polished Brown Grease (PBG) and subsequently selected for decarboxylation. Figure 5.4 is a photograph of the separated brown grease phases, illustrating the substantial differences between the unpolished material and its phase-separated constituent components.

Table 5.3 – Phase separation to liquid oil with different solvents at 25 °C

	Solvent (v/v)	Oil phase (% by v)
Phosphoric acid	15	14
Water	15	33
Methanol	15	22
Ethanol	15	27
Isopropyl alcohol	15	54
Ethyl acetate	15	38
Canola oil	15	21
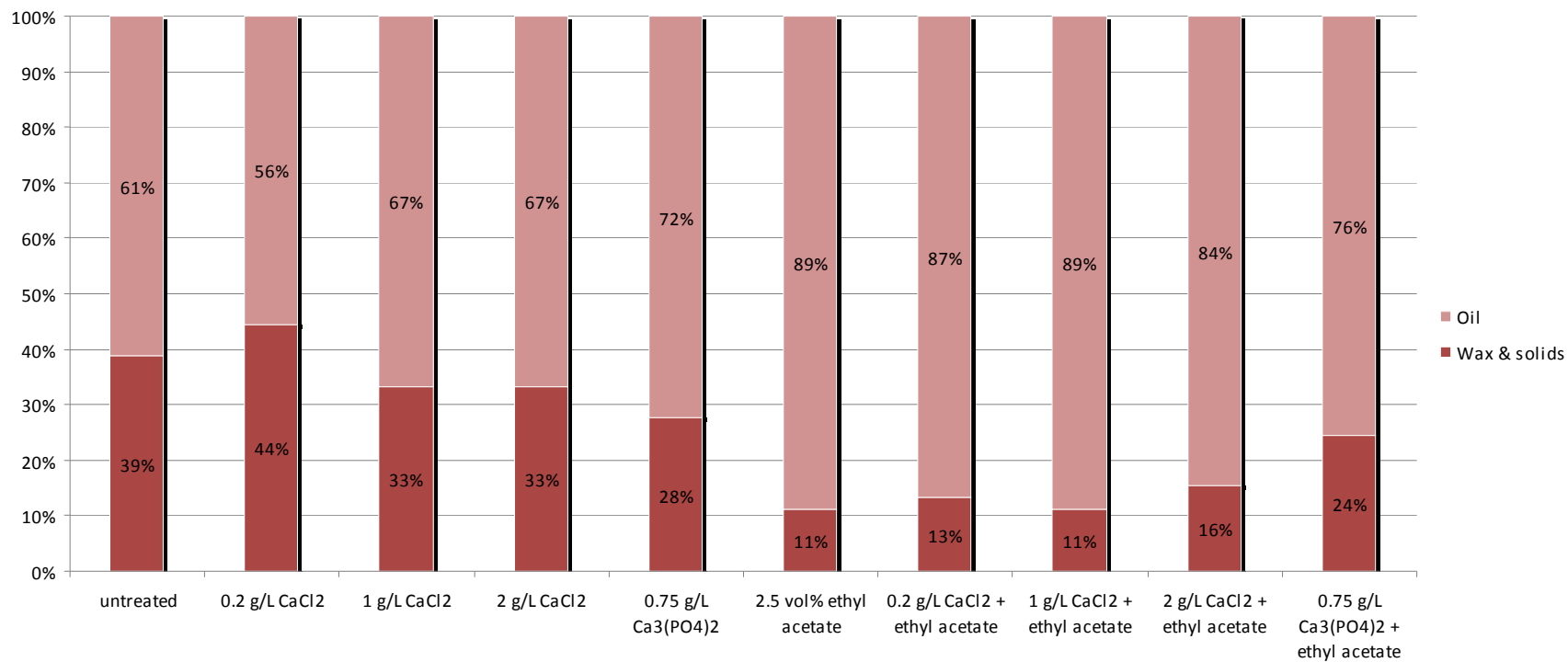
Figure 5.2 – Phase composition of brown grease after various treatments and centrifugation
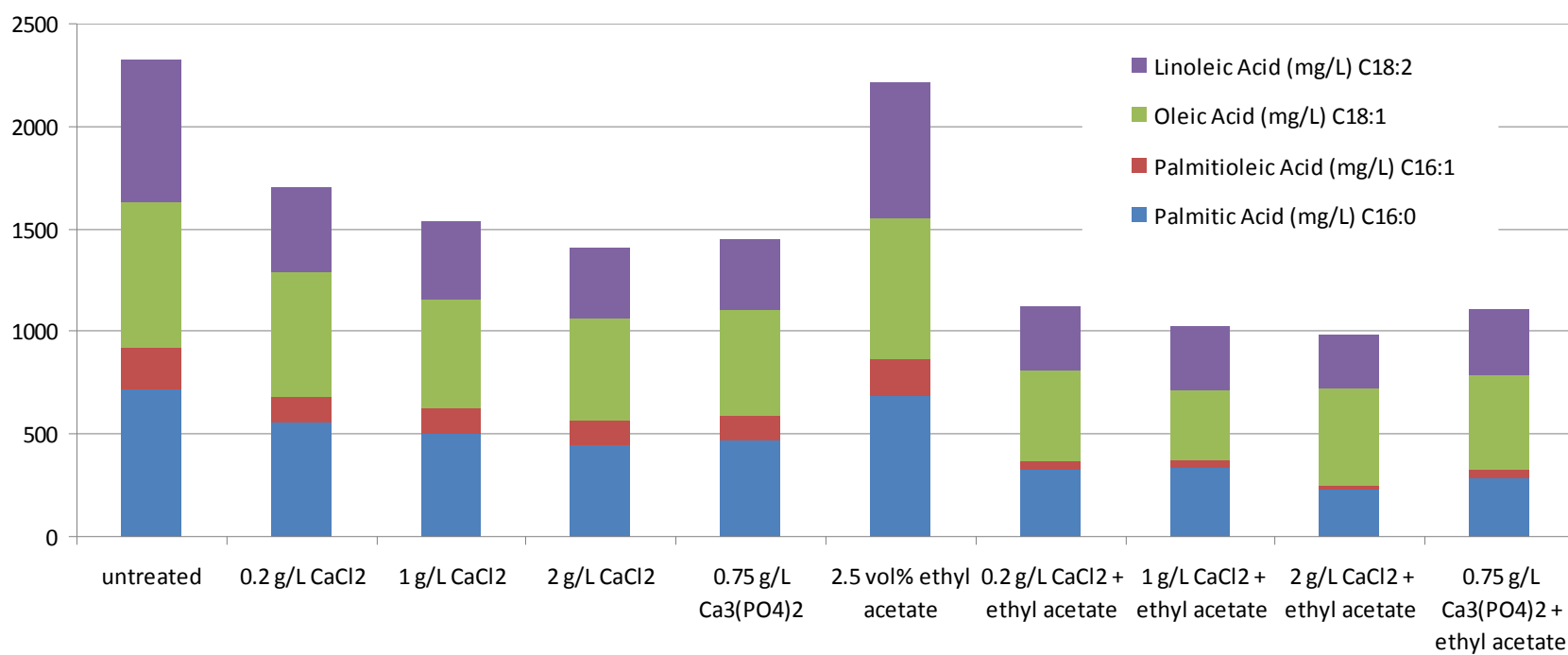
Figure 5.3 – Residual acid content and composition after various treatments.

Figure 5.4 – (top) Photograph of three separated phases of polished brown grease: solids (left), wax (center), oil (right); (bottom) the three phases of PBG on the right with the unpolished brown grease on the far left.

5.4 Decarboxylation of Polished Brown Grease

Decarboxylation of PBG was carried out over Pd-MCF catalyst as described previously. In general, 750 mg PBG and 25 mL dodecane were added to the reactor, already containing 250 mg pre-reduced Pd-MCF catalyst, and reactor was charged with H2 and stirred at 300 °C for 6 hours. Initially, the reaction was run in batch mode, designated PBG-B (Table 5.4), with conversions of C_{16} and C_{18} acids of 44% and 41%, respectively, and selectivities of 85% and 88% to the C_{n-1} hydrocarbons. During these batch reactions, there was a noticeable increase in the reactor pressure, hypothesized to

be a result of evolved CO_2, CO, and H_2O, as well as any trace cracking products. As discussed in Chapter 4, increased reaction overpressure results in competitive adsorption on the catalyst surface sites, not only decreasing net turnovers but potentially affecting the dominant reaction mode [11]. It is therefore not surprising to see lower than expected acid conversions and decarboxylation selectivities. In an attempt to mitigate competitive adsorption from large overpressures, decarboxylation of PBG in semi-batch was performed with a 10 mL/ min hydrogen flow, designated PBG-SB in Table 5.4. As hypothesized, high conversions and selectivities to the decarboxylated hydrocarbons were observed after 6 hours.

Table 5.4 – 6 hour decarboxylation results for PBG in batch and semi-batch.

| | C_{16} | | C_{18} | |
	Conversion	Selectivity[a]	Conversion	Selectivity[b]
PBG-B	44%	85%	41%	88%
PBG-SB	93%	98%	91%	96%

[a] to n-C_{15}, [b] to n-C_{17}

Total acid conversions after six hours for three different initial PBG loadings in batch and semi-batch are shown in Figure 5.5. As expected, a jump in conversion is seen in all cases when running the reaction in semi-batch as opposed to batch. Lower batch conversions are seen as the initial PBG loading increases, supporting the concentration-dependent decarboxylation rate discussed in Chapter 4 and elsewhere. In semi-batch, however, the conversions are quite similar for the three different loadings, suggesting the purge stream alleviates any non-negligible competitive adsorption effects. Pd-MCF

catalyst recycle tests were carried out in semi-batch for all cases as well, the results of which are also shown in Figure 5.5. The spent Pd-MCF catalyst was regenerated as discussed in Chapter 4 and reused in the decarboxylation of PBG. In all cases, the total acid conversion remains high, with only very slight decreases in the overall conversion.
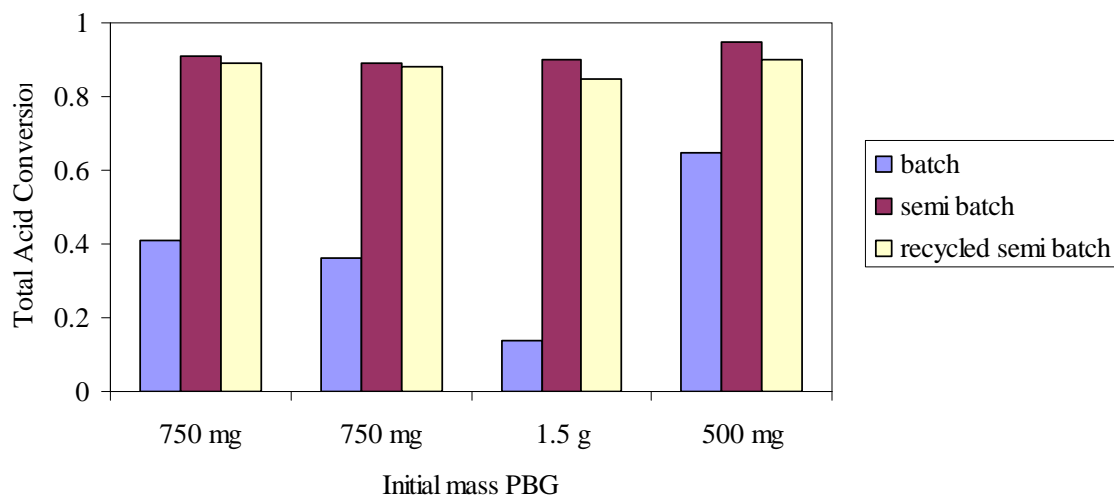
Figure 5.5 – Total acid conversion of PBG in Pd-MCF catalyzed decarboxylation for different initial concentrations of PBG. Data is shown for batch, semi-batch with 10 mL/min H2 flow, and a semi-batch reaction with recycled Pd-MCF catalyst.

5.5 Conclusions

A wastewater-derived brown grease feedstock was acquired from a poultry rendering facility as a candidate low-cost feedstock for renewable diesel-length hydrocarbon fuel. Attempts were made with little success to directly decarboxylate the unpolished brown grease with the Pd-MCF catalyst at 300 °C in a H_2 atmosphere, yielding low overall acid conversions with very low selectivities to the desired decarboxylated hydrocarbon product. Furthermore, 6 hours at 300 °C with the

unpolished brown grease was detrimental to both the catalyst and reactor system. Attempts were made to polish the brown grease, utilizing solvents and salts to separate the material into three distinct phases: undesirable solids, undesirable wax, and desirable oil. Ethyl acetate was identified as the preferable solvent, noting its low cost, low toxicity, and desirable phase separation observations, and performed very well in a treatment regimen with calcium chloride. The treatment yielded a large, neutral smelling translucent oil phase with high extraction of C_{16} and C_{18} fatty acids. The polished brown grease was then used as reactant for decarboxylation using Pd-MCF, in both batch and semi-batch reactions. The acid conversions were low for the batch decarboxylation due to the build up of pressure within the reactor, increasing the effect of competitive adsorption on the overall reaction rate. In semi-batch however, the conversions and selectivities were very high, resulting in a large yield of diesel-length hydrocarbons. Recyclability of the Pd-MCF catalyst was confirmed in the PBG decarboxylation system, retaining high reuse activity after treatment via the regeneration methodology developed in Chapter 4.

5.6 REFERENCES

[1]   D. Fairless, Nature. 449 (2007) 652-655.

[2]   J. Hill, E. Nelson, D. Tilman, S. Polasky, D. Tiffany, Proc. Natl. Acad. Sci. U. S. A. 103 (2006) 11206-11210.

[3]   C. Schubert, Nat. Biotechnol. 24 (2006) 777-784.

[4]   G. Stephanopoulos, Science. 315 (2007) 801-804.

[5]   Y. Zhang, M.A. Dube, D.D. McLean, M. Kates, Bioresour. Technol. 90 (2003) 229-240.

[6]   M.J. Haas, A.J. McAloon, W.C. Yee, T.A. Foglia, Bioresour. Technol. 97 (2006) 671-678.

[7]   M. Canakci, J. Van Gerpen, Transactions of the Asae. 44 (2001) 1429-1436.

[8]   M.G. Kulkarni, A.K. Dalai, Ind. Eng. Chem. Res. 45 (2006) 2901-2913.

[9]   B.K. De, D.K. Bhattacharyya, J. Am. Oil Chem. Soc. 75 (1998) 1683-1686.

[10]   L. Rajam, D.R.S. Kumar, A. Sundaresan, C. Arumughan, J. Am. Oil Chem. Soc. 82 (2005) 213-220.

[11]   J.G. Immer, M.J. Kelly, H.H. Lamb, Applied Catalysis a-General. 375 (2010) 134-139.

CHAPTER 6

SUMMARY

Development of new renewable and economically viable transportation fuels is highly important for both geopolitical and environmental reasons. Recent reports regarding the production of diesel-length hydrocarbons from simulated high-acid feedstocks were promising, but reported severe single-use deactivation of the commercially available supported palladium catalysts. The main goal of this thesis was to design new catalysts to probe the nature of this deactivation, with an eye to developing appropriate regeneration methodologies for eventual application to real feedstocks.

Initially, of course, this meant designing a supported palladium catalyst to do just that. In order to extract meaningful observations from post-mortem characterization, the catalyst had to be well-defined—that is to say, both substrate and metal must be quantifiably characterized. There were many things to consider when deciding upon the catalyst support, including porosity, available surface area, stability to both temperature and pressure, ease of functionalization, among others. Likewise, if the catalyst deactivation was indeed affected by any sort of carbonaceous deposition, as hypothesized in the literature, the support must not interfere with direct characterization methods. Furthermore, the catalyst synthesis methodology must yield palladium nanoparticles with a very narrow pore size distribution, with similar morphology, evenly distributed throughout the entirety of the support. Taking these things into consideration, various attempts were made at synthesizing a well-defined palladium nanoparticle catalyst on a

96

mesoporous silica support, with varying degrees of success and failure. Eventually, calcined silica mesocellular foam was surface-functionalized with silanes to ligate palladium precursor salts, which were then calcined in air and reduced in hydrogen to form small 2-3 nm zero-valent palladium particles evenly distributed throughout the MCF particles.

These Pd-MCF catalysts were then tested in the 300 °C decarboxylation of many model biofeedstock compounds, including saturated and unsaturated acids, alkyl esters, glycerol, and mixtures thereof, to probe their activities. Fully saturated substrates were shown to successfully decarboxylate in the absence of hydrogen, while unsaturated substrates required hydrogen to first hydrogenate before decarboxylation. This step-wise reaction pathway manifested itself in the quite similar decarboxylation conversions of stearic acid and oleic acid, with the latter completely hydrogenating to the former during the temperature ramp of the stainless steel reactor. Likewise, alkyl esters were observed to proceed to decarboxylated hydrocarbon through the saturated acid. Glycerol dehydration occurred quite readily under decarboxylation conditions, yielding mainly propane and water, and had little effect when introduced as an additive in the decarboxylation of acid mixtures.

The Pd-MCF catalysts exhibited similar detrimental single-use deactivation, and the nature of this deactivation was probed via a barrage of post-mortem characterization comparisons. Hydrogen uptake measurements suggested a severely decrease accessible metal surface area for adsorption, but palladium nanoparticle morphological changes such as sintering, agglomeration or ripening were ruled out by transmission electron microscopy and X-ray adsorption spectroscopy. Physisorption indicated a substantial

surface area and pore volume loss, and thermogravimetric analysis suggested significant organic deposition. High temperature calcination succeeded in removing these deposits at the expense of considerable nanoparticle growth. Infrared spectroscopy and nuclear magnetic resonance suggested that the organic deposition was residual reactant acid, solvent, and products, and an extraction methodology was developed accordingly. After a regimen of solvent washes at elevated temperature, the catalyst regained pore volume, surface area, accessible palladium sites, and ultimately decarboxylation activity.

The Pd-MCF catalyst was then directly applied to a wastewater brown grease feedstock acquired from a local poultry rendering facility, to limited success. The massive impurities in the raw brown grease severely limited the decarboxylation activity and were detrimental to both reactor and catalyst. Polishing methodologies were developed, adopting dewaxing and degumming techniques from literature, and a calcium chloride and ethyl acetate treatment procedure was adopted to maximize the oil phase volume and acid extraction extent in a three-phase separation. Decarboxylation of the polished brown grease was performed to great success, with both high acid conversions and high selectivities to the hydrocarbon product. The Pd-MCF was successfully recycled in the PBG system, utilizing the same regeneration methodology developed for the model compound system. The successful and repeated formation of diesel-length hydrocarbons from an otherwise-waste biofeedstock is an important milestone in the quest for renewable transportation fuels. While the Pd-MCF catalyst is likely not to be applied in an industrial setting due to the costs involved in synthesizing such a specifically-tuned material, hopefully the knowledge gained from this work can be adapted for further exploration into the realm of next-generation biofuels.

APPENDIX A

PORE SIZE DISTRIBUTION METHODOLOGIES FROM N$_2$ PHYSISORPTION

ISOTHERMS

A.1 PORE SIZE DISTRIBUTION METHODOLOGIES

Of the many pore size distribution methodologies in existence, the theory proposed by Barrett, Joyner and Halenda (BJH) in 1951 is one of the most commonly applied PSD methods to mesoporous materials [1]. This method directly utilizes the Cohan Equation [2]:

$$\ln(p_0 / p) = \frac{f \gamma V_m}{RT(r-t)}$$

where p/p_o is relative pressure, T is absolute temperature, R is the gas constant, f is the Laplace meniscus curvature factor, γ is the adsorbate surface tension, V_m is the adsorbate molar volume, and t is the statistical thickness of adsorbed gas. Despite its wide usage, the BJH method neglects the effect of pore wall curvature on the thickness of the adsorbed gas layer and therefore systematically underestimates mesopore size [3]. In 1967, Broekhof and de Boer introduced a new set of theoretical equations to account for these discrepancies [3-5]:

$$\ln(p_0 / p) - F(t) = \frac{f \gamma V_m}{RT(r-t)}$$

$$-\frac{dF(t)}{dt} = \frac{f \gamma V_m}{RT(r-t)^2}$$

$$\ln(p_0 / p) = \frac{2\gamma V_m}{RT(r-t)} + \frac{\int_t^r 2(r-t)F(t)dt}{RT(r-t)^2}$$

The first equation can be solved for the thickness of the adsorbed gas layer on a curved surface. The first and second equations can be solved simultaneously to determine the radius of a pore that undergoes capillary condensation. The first and third equations can be solved simultaneously to determine the radius of a pore that undergoes capillary evaporation. The function $F(t)$ is required to solve this system, and BdB provided a semi-empirical function:

$$F(t) = \frac{16.11}{t^2} - 0.1682e^{-0.1137t}$$

which results in some very complicated calculus to solve the system of equations. This system can be simplified dramatically by applying physical adsorption theory developed independently by Frenkel, Hill and Halsey [6-8] in the form of:

$$F(t) = \frac{\alpha}{t^3}$$

where α is the tabulated interaction constant for a given adsorbent-adsorbate pair (e.g., α = 221.8 Å^3 for N_2 on SiO_2). This severely simplifies the BdB equations to [9]:

$$\ln(p_0 / p) - \frac{\alpha}{t^3} = \frac{f\gamma V_m}{RT(r-t)}$$

$$\frac{3\alpha}{t^4} = \frac{f\gamma V_m}{RT(r-t)^2}$$

$$\ln(p_0 / p) - \frac{\alpha}{rt^4} = \frac{2\gamma V_m}{RT(r-t)}$$

Now, from the adsorption branch of the isotherm, pore size can be determined analytically from the first equation and the square root of the second equation. The pore size from the desorption branch must be determined numerically from simultaneously

solving the first and third equations. PSD determination from this modified method (BdB-FHH) is much more mathematically accessible than the original BdB method.

But why go to all the fuss? A comparison of average pore size of mesoporous silicas with tunable cylindrical pore radii (MCM-41, SBA-15) calculated via BJH and BdB-FHH is shown in Figure A1 along with the 'actual' pore size, as determined by SAXS, XRD and TEM. It should be clearly noticeable the systematic underestimation of average mesopore size by BJH across the entire range of tested materials.

Primary Pore Size of various MCM-41 and SBA-15
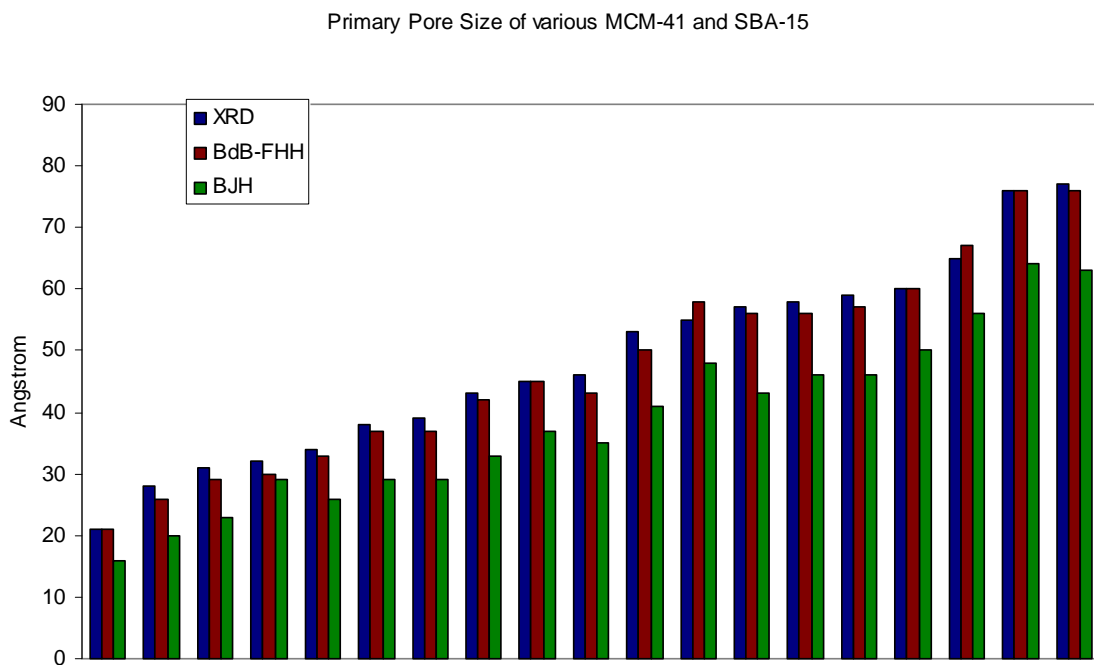
Figure A1 – Comparison of primary pore sizes of SBA-15 and MCM-41 materials as calculated by BJH and BdB-FHH (some data adapted from [9])

Another benefit to using BdB-FHH for mesoporous materials is that, unlike with BJH, for straight cylindrical pores, the pore size distributions from adsorption & desorption branches reduce to equivalent curves (Figure A2). This, at worst, removes the ambiguity

of choosing whether to extract primary pore size data from the adsorption PSD or desorption PSD. If the BdB-FHH PSDs are separated, this provides insight as to the nature of the pores (i.e., the farther the deviation from equivalency, the higher degree of curvature / non-ideality in the material's mesopores), Additionally, and most importantly for this thesis work, is the ability of BdB-FHH to isolate bimodal pore size distributions from ink bottle or cell-and-window mesopore structures [5, 9]. Figure A3 shows an example pore size distribution from silica MCF, with large spherical cells and smaller interconnecting cylindrical windows. The adsorption upswing of the physisorption isotherm yields the pore size distribution for the large spherical cells via capillary condensation, while the desorption arm yields the PSD for the smaller cylindrical windows via capillary evaporation.
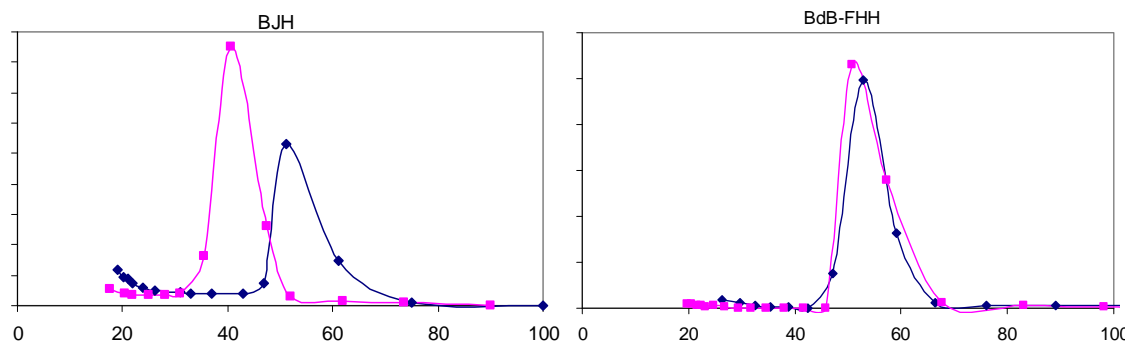
Figure A2 – SBA-15 PSD calculated via BJH (left) and BdB-FHH (right)
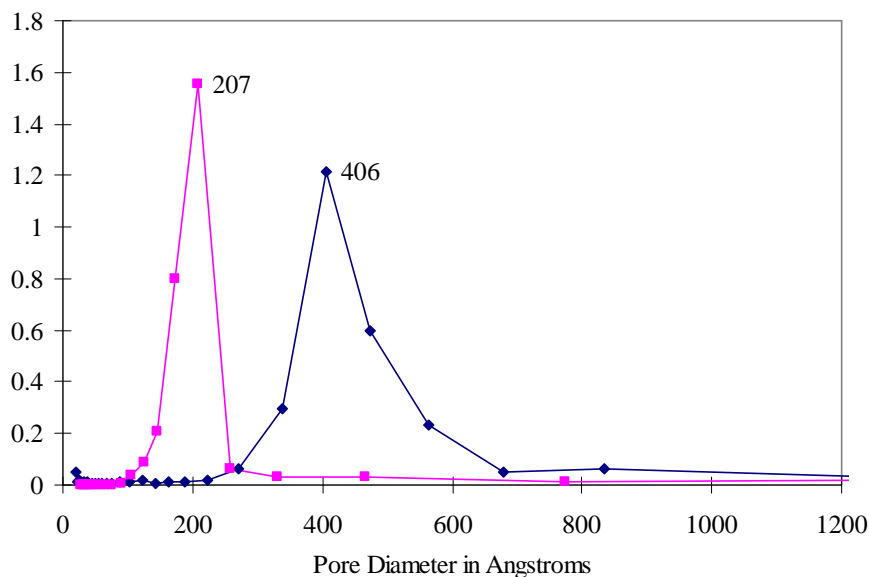
Figure A3 – BdB-FHH PSD for MCF showing bimodal distribution.

A.2 BdB-FHH Excel Macro

In order to provide the group with an accessible way to easily calculate pore size distributions from physisorption isotherms, a macro was written for Microsoft Excel to create BdB-FHH PSDs, following the methodology presented above and in [9]. The VBA code for the BdB-FHH macro is included below.

```
Sub PSD()

Dim Pr(100), Rcr(100), Vl(100), Tcr(100), Vd(100), Csa(100), Vc(100), Pave(100)
Dim PoreV(100), Lp(100), Tave(100), Rc(100), Rave(100), Te(100, 100)
Dim Te1 As String
Dim C(10), T, f, df, dx, Tlast As Double
PageTitle = "Adsorp in "
MeniscusTitle = "Hemispherical Meniscus"
Pi = 3.14159
```

```
a = 5 * (3.541 ^ 3)

R = 0.8314

T = 77.2

RT = R * T

Gamma = 8.72

Vm = 34.68

factoroot = 2 * Gamma * Vm / (R * T)

PoreType = ""

On Error Resume Next

Set dData = Application.InputBox("Please select the cells which contain your isotherm
data. The data must contain p/p0 in column 1 and the volume of gas adsorbed (as gas) in
column 2.", "Select Isotherm Data", Type:=8)

If Err <> 0 Then

    On Error GoTo 0

    Exit Sub

End If

On Error GoTo 0


Do Until PoreType = "sphere" Or PoreType = "s" Or PoreType = "cylinder" Or PoreType
= "c" Or PoreType = False

PoreType = Application.InputBox("Which pore model are you using, cylinder or sphere
(c or s)?", "Pore Model")

    Loop

    If PoreType = False Then

        Exit Sub

    End If

answer1 = MsgBox("Is this an adsorption isotherm?", vbYesNo)

Answer2 = MsgBox("Does the isotherm display hysteresis?", vbYesNo)

alpha = InputBox("What is the value of the FHH parameter, alpha? (Default =
5*3.541\3)", "Enter alpha", a)

If answer1 = vbNo Then
```

```vba
    PoreType = "c"
    PageTitle = "Desorp from "
End If
If PoreType = "sphere" Or PoreType = "s" Then
    ModelSheet = "Spheres"
    PoreType = "s"
    factory = factoroot
    PoreTitle = "Spherical Pores"
Else
    ModelSheet = "Cylinders"
    PoreType = "c"
    factory = factoroot / 2
    PoreTitle = "Cylindrical Pores"
End If
If Answer2 = vbNo Then ModelSheet = ModelSheet & " no Hy"
If alpha = "" Then
    Exit Sub
End If
If answer1 = vbYes Then
    celltitle = "Adsorption in " & ModelSheet
Else
    celltitle = "Desorption from " & ModelSheet
End If
ModelSheet = PageTitle & ModelSheet

ActiveSheet.Activate
dData.Select
Selection.Copy
ActiveSheet.Activate
Sheets.Add
ActiveSheet.Paste
```

```vba
ActiveSheet.Name = ModelSheet
Worksheets(ModelSheet).Activate
Selection.Sort Key1:=ActiveCell, Order1:=xlDescending, Header:=xlGuess,
OrderCustom:=1, MatchCase:=False, Orientation:=xlTopToBottom

iRows = Selection.Rows.Count
Cells(1, 3).Formula = "=B1*0.0015468"
Cells(1, 3).Select
Selection.AutoFill Destination:=Range(Cells(1, 3), Cells(iRows, 3)), Type:=xlFillDefault

For I = 1 To iRows
    Pr(I) = Cells(I, 1)
    Vl(I) = Cells(I, 3)
Next I
If answer1 = vbNo Or Answer2 = vbNo Then

If answerl = vbNo Then
    BranchTitle = "Desorption from"
Else
    BranchTitle = "Adsorption w/o Hysteresis" & Chr(13) & "in"
End If
fa = factoroot / 2
For I = 1 To iRows
    lnp = -Log(Pr(I))
    THigh = 5 * (alpha / lnp) ^ (1 / 3)
    TLow = 0.5 * (alpha / lnp) ^ (1 / 3)
    T = 3 * (alpha / lnp) ^ (1 / 3)
    C(1) = alpha * alpha / lnp
    C(2) = 0#
    C(3) = -2 * alpha * fa / lnp
    C(4) = -2 * alpha
```

```
    C(5) = 0#
    C(6) = fa
    C(7) = lnp
    For K = 1 To 20
        f = C(1) + T * T * (C(3) + T * (C(4) + T * T * (C(6) + T * C(7))))
        df = T * (2 * C(3) + T * (3 * C(4) + T * T * (5 * C(6) + T * 6 * C(7))))
        dx = f / df
        If dx > 0 Then
            THigh = T
        End If
        If dx < 0 Then
            TLow = T
        End If
        T = T - dx
        If (Abs(dx) < 0.00000000000001) Then Exit For
        If T > THigh Then
            T = (THigh + Tlast) / 2
        End If
        If T < TLow Then
            T = (TLow + Tlast / 2)
        End If
        Tlast = T
    Next K
    Tcr(I) = T
    Cells(I, 4) = T
    Rcr(I) = Tcr(I) + fa / (lnp - alpha / (Tcr(I) ^ 3))
Next I
Else

    If PoreType = "c" Then MeniscusTitle = "Cylindrical Meniscus"
    BranchTitle = "Adsorption in"
```

```
For I = 1 To iRows

    logprel = Log(Pr(I))

    q = -((alpha * factory / 3) ^ 0.5) / logprel

    R = alpha / (2 * logprel)

    If R ^ 2 < q ^ 3 Then

        x = R / Sqr(q ^ 3)

        theta = Atn(-x / Sqr(-x * x + 1)) + 1.5708

        root2 = -2 * Sqr(q) * Cos((theta + 2 * 3.14159) / 3)

        Tcr(I) = root2

    Else

        a = -Sgn(R) * (Abs(R) + Sqr(R ^ 2 - q ^ 3)) ^ (1 / 3)

        b = q / a

        Tcr(I) = a + b

    End If

    Rcr(I) = Tcr(I) + factory / (-logprel - alpha / Tcr(I) ^ 3)

Next I

End If


For I = 1 To iRows - 1

    Rave(I) = (Rcr(I) + Rcr(I + 1)) * Rcr(I) * Rcr(I + 1) / (Rcr(I) ^ 2 + Rcr(I + 1) ^ 2)

    a = Sqr(factory)

    b = Sqr(3 * alpha)

    d = -Rave(I) * b

    q = -0.5 * (b + Sgn(b) * Sqr(b ^ 2 - 4 * a * d))

    Tave(I) = d / q

    Pave(I) = Exp(-(factory / (Rave(I) - Tave(I)) + alpha / Tave(I) ^ 3))

Next I


C(2) = alpha

C(3) = 0#

For I = 2 To iRows
```

```
    Rcrit = Rave(I - 1)
    C(1) = -alpha * Rcrit
    T = Tcr(I)
    For J = I + 1 To iRows + 1
        Prel = Pr(J - 1)
        Plog = -Log(Prel)
        C(5) = -Plog
        C(4) = Rcrit * Plog - factory
        For K = 1 To 20
            f = C(1) + T * (C(2) + T ^ 2 * (C(4) + T * C(5)))
            df = C(2) + T * (T * (3 * C(4) + T * 4 * C(5)))
            dx = f / df
            T = T - dx
            If (Abs(dx) < 0.0000000001) Then Exit For
        Next K
        Te(J - 1, I - 1) = T
    Next J
Next I

For I = 1 To iRows - 1
    Vd(I) = 0#
    If I = 1 Then
        Vd(I) = 0#
    Else
        For J = 1 To I - 1
            If PoreType = "s" Then
                Vd(I) = Vd(I) + 1E-24 * (4 / 3) * Pi * ((Rave(J) - Te(I + 1, J)) ^ 3 - (Rave(J) -
Te(I, J)) ^ 3) * Lp(J)
            Else
                If PoreType = "c" Then
```

```
            Vd(I) = Vd(I) + 1E-16 * Pi * ((Rave(J) - Te(I + 1, J)) ^ 2 - (Rave(J) - Te(I,

J)) ^ 2) * Lp(J)

          Else

              sorry = MsgBox("error at Vd(I) stage", vbOKOnly)

              Exit Sub

          End If

        End If

      Next J

  End If


  If Vd(I) >= (Vl(I) - Vl(I + 1)) Then

    Lp(I) = 0#

    Vc(I) = 0#

    Csa(I) = 0#

  Else

    Vc(I) = Vl(I) - Vl(I + 1) - Vd(I)

    If PoreType = "s" Then

      Csa(I) = 4E-24 * (Pi / 3) * (Rave(I) - Te(I + 1, I)) ^ 3

    Else

      If PoreType = "c" Then

        Csa(I) = Pi * 1E-16 * (Rave(I) - Te(I + 1, I)) ^ 2

      Else

        sorry = MsgBox("error at Csa calculation", vbOKOnly)

        Exit Sub

      End If

    End If

    Lp(I) = Vc(I) / Csa(I)

  End If

  If PoreType = "s" Then

    PoreV(I) = 4E-24 * (Pi / 3) * Lp(I) * Rave(I) ^ 3

  Else
```

110

```
        If PoreType = "c" Then
            PoreV(I) = 1E-16 * Lp(I) * Pi * Rave(I) ^ 2
        Else
            sorry = MsgBox("error at PoreV calculation", vbOKOnly)
            Exit Sub
        End If
    End If
Next I


BigPoint = 0
BigPointNumber = 1
CumSA = 0
CumPV = 0
For J = 1 To iRows - 1
    Cells(J, 4) = Tcr(J)
    Cells(J, 5) = Rcr(J)
    Cells(J, 6) = Pave(J)
    Cells(J, 7) = Tave(J)
    Cells(J, 8) = Rave(J)
    Cells(J, 9) = Rave(J) * 2
    Cells(J, 10) = Vc(J)
    Cells(J, 11) = Csa(J)
    Cells(J, 12) = Lp(J)
    Cells(J, 13) = PoreV(J)
    Cells(J, 14) = Vd(J)
    Cells(J, 15) = Rave(J) * 2
    Cells(J, 16) = PoreV(J)
    If Rave(J) < 10 Then Exit For
    If Cells(J, 16) > BigPoint Then
        BigPointNumber = J
        BigPoint = Cells(J, 16)
```

```
      End If


   If PoreType = "s" Then
      Cells(J, 17) = 4E-20 * Pi * Lp(J) * Rave(J) ^ 2
   Else
      If PoreType = "c" Then
         Cells(J, 17) = 0.000000000002 * Pi * Lp(J) * Rave(J)
      Else
         sorry = MsgBox("error at cumulative surface area calculation", vbOKOnly)
         Exit Sub
      End If
   End If
   CumSA = CumSA + Cells(J, 17)
   CumPV = CumPV + PoreV(J)
   Cells(J, 18) = CumSA
   Cells(J, 19) = CumPV
Next J


Cells(1, 1).Select
Selection.EntireRow.Insert
Cells(1, 1) = "Rel pres"
Cells(1, 2) = "Vol as gas"
Cells(1, 3) = "Vol as liq"
Cells(1, 4) = "Crit thick"
Cells(1, 5) = "Crit radius"
Cells(1, 6) = "Avg pres"
Cells(1, 7) = "Avg thick"
Cells(1, 8) = "Avg radius"
Cells(1, 9) = "Avg diam"
Cells(1, 10) = "Vol cores"
Cells(1, 11) = "X sect area"
```

```
Cells(1, 12) = "Pore length"
Cells(1, 13) = celltitle
Cells(1, 14) = "Vol desorp"
Cells(1, 15) = "Avg diam"
Cells(1, 16) = celltitle
Cells(1, 17) = "Surf area"
Cells(1, 18) = "Cumul SA"
Cells(1, 19) = "Cumul PoreV"
SurfaceArea = Fix(CumSA + 0.5)
PoreVolume = Fix(100 * CumPV + 0.5) / 100


    Columns("O:O").Select
    Selection.NumberFormat = "0"
    Charts.Add
    ActiveChart.ChartWizard Source:=Sheets(ModelSheet).Range("$O:$P"),
Gallery:=xlXYScatter, Format:=2, PlotBy:=xlColumns, CategoryLabels:=1,
SeriesLabels:=1, HasLegend:=2, Title:="Plot for " & celltitle, CategoryTitle:="Pore
Diameter in Angstroms", ValueTitle:="Pore Volume in cc per gram", ExtraTitle:=""
    ActiveChart.PlotArea.Select
    Nombre = ModelSheet & " Plot"
    ActiveSheet.Name = Nombre
End Sub


Sub Macro1_combined_graphs()

    Sheets("Adsorp in Spheres Plot").Select
    Sheets("Adsorp in Spheres Plot").Copy Before:=Sheets(5)
    Sheets("Adsorp in Spheres Plot (2)").Select
    Sheets("Adsorp in Spheres Plot (2)").Name = "combined"
    ActiveChart.PlotArea.Select
    ActiveChart.SeriesCollection.NewSeries
```

```
ActiveChart.SeriesCollection(2).XValues = _
    "='Desorp from Cylinders'!R2C15:R23C15"
ActiveChart.SeriesCollection(2).Values = _
    "='Desorp from Cylinders'!R2C16:R23C16"
ActiveChart.SeriesCollection(2).Name = "='Desorp from Cylinders'!R1C16"
ActiveChart.Axes(xlCategory).Select
With ActiveChart.Axes(xlCategory)
    .MinimumScale = 0
    .MaximumScale = 1500
    .MinorUnitIsAuto = True
    .MajorUnitIsAuto = True
    .Crosses = xlAutomatic
    .ReversePlotOrder = False
    .ScaleType = xlLinear
    .DisplayUnit = xlNone
End With
End Sub
```

A.3 REFERENCES

[1]   E.P. Barrett, L.G. Joyner, P.P. Halenda, J. Am. Chem. Soc. 73 (1951) 373-380.

[2]   L.H. Cohan, J. Am. Chem. Soc. 60 (1938) 433-435.

[3]   Broekhof.Jc, J.H. Deboer, J. Catal. 9 (1967) 8-&.

[4]   Broekhof.Jc, J.H. Deboer, J. Catal. 10 (1968) 368-&.

[5]   Broekhof.Jc, J.H. Deboer, J. Catal. 10 (1968) 153-&.

[6]   G. Halsey, J. Chem. Phys. 16 (1948) 931-937.

[7]   G.D. Halsey, Adv. Catal. 4 (1952) 259-269.

[8]   T.L. Hill, Adv. Catal. 4 (1952) 211-258.

[9]   W.W. Lukens, P. Schmidt-Winkel, D.Y. Zhao, J.L. Feng, G.D. Stucky, Langmuir.
15 (1999) 5403-5409.

APPENDIX B

SUPPLEMENTARY CHACTERIZATION

B.1 Chemisorption

Initial active catalyst surface area characterization was carried out using CO chemisorption. However, the binding mechanism of CO on palladium surfaces with defects is not clear, calling into question the validity of the surface area estimations. The Micromeritics AutoChem II 2920 measures uptake and calculates metal surface area from this measured uptake via geometrical assumptions and utilizing a stoichiometry parameter. With ambiguity as to the adsorbate-adsorbent binding stoichiometry of the palladium/CO system, calculated metal surface areas are less than trustworthy. A common alternative to the binary Pd/CO adsorption system is hydrogen chemisorption. To get reliable quantitative hydrogen uptake measurements however, the sample must be put under vacuum to remove adsorbed hydrogen, and our AutoChem II 2920 was not equipped with such a system. Instead, an alternative methodology to displacing surface hydrogen was adopted: H_2-O_2-H_2 titration. The general idea is that after reductive pre-treatment and high temperature passivation, the surface is alternately titrated to saturation with H_2 and O_2 with a TCD detector measuring the outlet gas flows and peak integration determining total uptake of the given adsorbate. So instead adsorbing hydrogen onto a bare metallic surface as in standard hydrogen chemisorption, the hydrogen is displacing surface oxygen, and vice versa during oxygen titration. The titrations are alternated for three or more cycles to provide replicate data sets. An example TCD response from

replicate titrations is shown in Figure B1, each with 20 injections of hydrogen over the duration of 100 minutes. The similarity of the response curves validates the hypothesis that any adsorbed hydrogen from a given cycle is removed/replaced during the next oxygen titration, which is likewise displaced again by the next hydrogen titration.
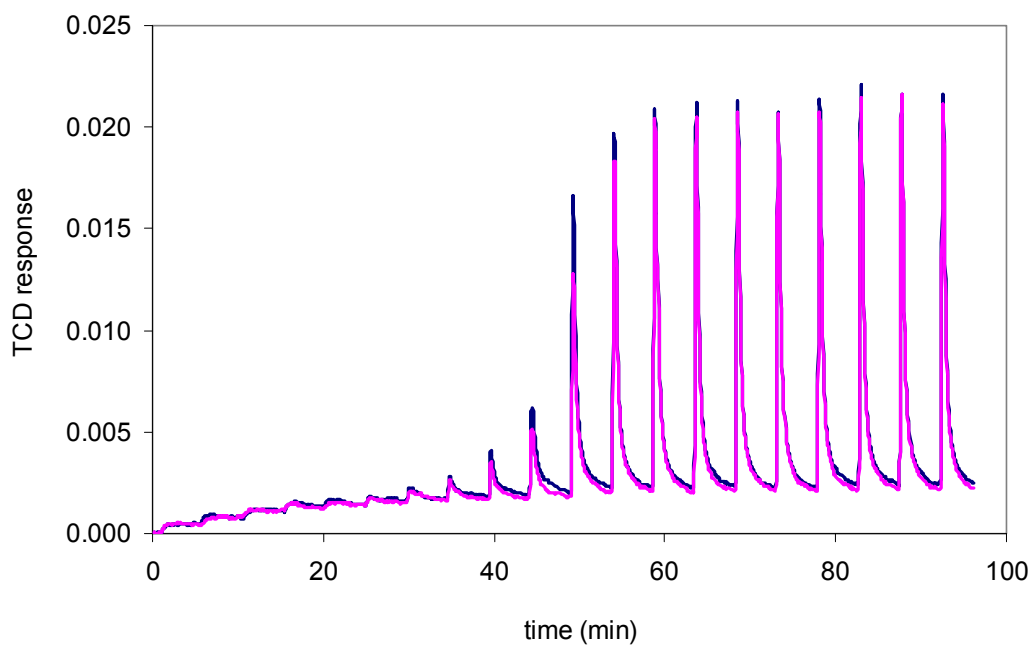

Figure B1 – Two (pink and blue) TCD response curves for replicate hydrogen titrations on Pd-MCF catalysts during H_2-O_2 titration chemisorption.

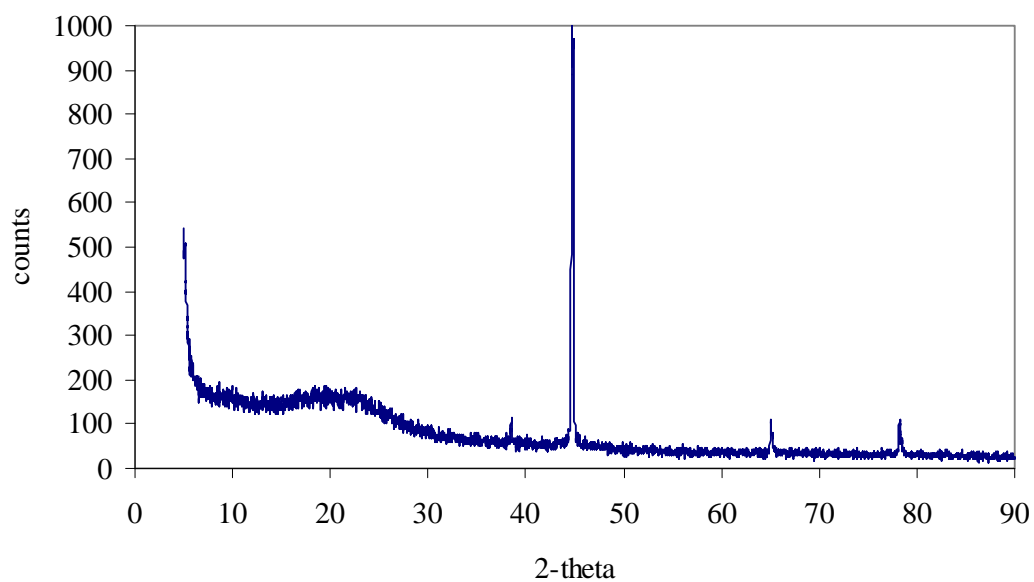**B.2 X-ray Diffraction Patterns**
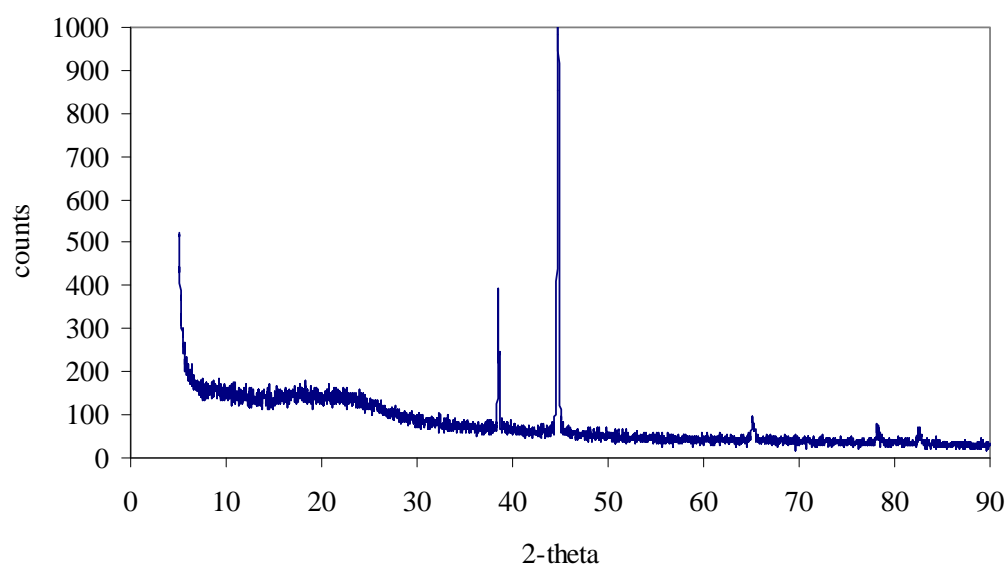

Figure B2 – XRD Pattern for PdSBA15-2

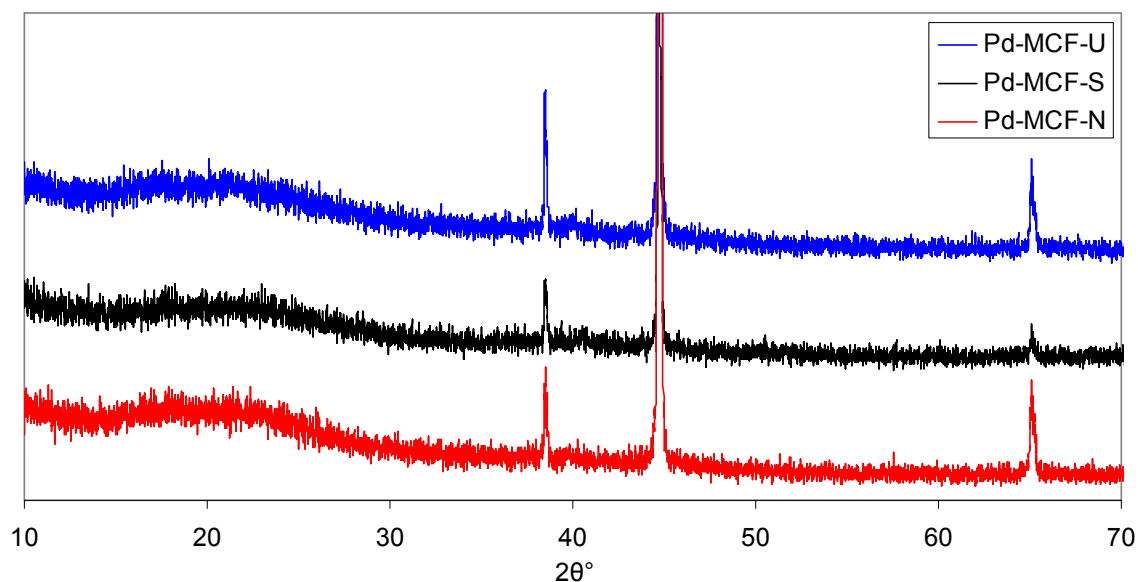Figure B3 – XRD pattern for 3APSBA15-Pd^0-2

Figure B4 – XRD patterns for Pd-MCF-X catalysts, offset for clarity.

B.3 Proton NMR of Dissolved Spent Pd-MCF Catalyst

Spent Pd-MCF catalyst dissolution was performed by stirring 250 mg catalyst in 100 mL aqueous strong base (1 g KOH / g H_2O), resulting in free palladium nanoparticles, soluble silica salts, and any residual organics. The organic fraction was separated via extractions with diethyl ether and characterized with solution phase ^1H nuclear magnetic resonance (NMR), performed using a Mercury Vx 400 MHz with $CDCl_3$ as solvent. The resulting NMR spectrum is shown in Figure B5. Looking beyond the peaks assigned to deuterated chloroform, TMS standard, water, and residual ether (from the organic extraction), the proton shifts at 0.9, 1.3, 1.6, 2.0 and 5.3 ppm match nicely with those of reactant oleic acid. The 5.3 ppm shift is especially characteristic, being the sp^2 protons at the C9 position. The dissolved catalyst proton NMR spectrum corroborated the findings of both GC-MS analysis of the dissolved organic extract and solid state carbon NMR.
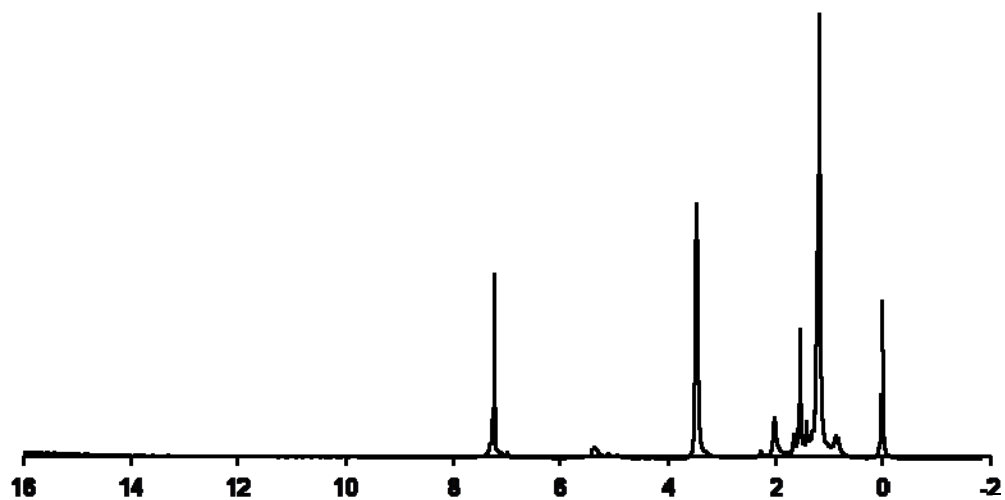
Figure B5 – ^{1}H NMR spectrum of dissolved spent Pd-MCF catalyst.